Theoretical and Experimental Investigation of Graphene based Devices for Bio-Sensing Applications

A

Thesis submitted

for the award of the degree of

DOCTOR OF PHILOSOPHY

By

Rajan Singh

DEPARTMENT OF ELECTRONICS AND ELECTRICAL ENGINEERING

INDIAN INSTITUTE OF TECHNOLOGY GUWAHATI

GUWAHATI - 781 039, ASSAM, INDIA

October 2021

Certificate

This is to certify that the thesis entitled "**Theoretical and Experimental Investigation of Graphene based Devices for Bio-Sensing Applications**", submitted by **RAJAN SINGH** (136102008), a research scholar in the *Department of Electronics and Electrical Engineering, Indian Institute of Technology Guwahati*, for the award of the degree of **Doctor of Philosophy**, is a record of an original research work carried out by him under my supervision and guidance. The thesis has fulfilled all requirements as per the regulations of the institute and in my opinion has reached the standard needed for submission. The results embodied in this thesis have not been submitted to any other University or Institute for the award of any degree or diploma.

Dated:

Guwahati.

Prof. Roy Paily Palathinkal
Professor
Dept. of Electronics and Electrical Engg.
Indian Institute of Technology Guwahati
Guwahati - 781 039, Assam, India.

To

My guide **Prof. Roy Paily Palathinkal**

for his guidance and inspiration

&

My **parents** and **brother**

for their blessings, love and support

Acknowledgements

This thesis would not have been possible without the immense help and support of several people in various measures. I would like to convey my acknowledgment to all of them.

First and foremost, I express my sincere gratitude to my research supervisor, Prof. Roy Paily Palathinkal for providing me an opportunity to work under his guidance. It is very difficult to describe my feelings in words to acknowledge my supervisor for his continuous guidance in all aspects, constant motivation and support throughout the doctoral studies. I am very much thankful to him for transforming me from an unstructured form to a structured form in every aspect of my life and showing me a different path of life. It would be completely impossible for me to bring the research as well as the thesis to this form without the immense facilities provided by him in VLSI Lab I and Centre of Nanotechnology and the freedom of work he has given to me.

I am thankful to my doctoral committee members Prof. H.B Nemade, Prof. P.K Iyer, Dr. Nagarjun Nallam, Prof. Siddhartha Sankar Ghosh and Dr. Mahima Arrawatia for their encouragement and valuable suggestions on my work. I would like to thank faculty members and the office staffs of the Department of Electronics and Electrical Engineering, IIT Guwahati, for their help in carrying out this research work.

I am thankful to my friends Dr. Jitendra Prajapati and Dr. Jitendra Kumar for their assistance in writing my thesis. I am also thankful to all my friend of IITG who stood with me during every ups and downs I faced during the duration of my PhD.

I attribute this achievement to my parents for their constant blessings, support, silent prayers for my success and moreover, making me stand in this position.

Rajan Singh

Abstract

Biosensors are widely used to expedite the estimation of vital health signatures and provide techniques that aid in the continuous health monitoring of patients. Over the last few decades, the advancement in the silicon industry caused significant improvement in the development of sensing devices, marketing sensitive and robust sensors. However, multidisciplinary expertise is needed for the furtherance of developed biosensors. Biotechnology provides simple yet efficient assays to detect biomarkers and hence plays an imperative role in sensor development. Recent developments in two-dimensional nanomaterials such as graphene have also proved to be of great importance to achieve better sensor performances. However, the estimation and modelling of the interaction between the biomarkers and newly discovered nanomaterials are not yet matured, which is indispensable for developing a new generation of sensors. The traditional methods to evaluate these interactions are based on experimentally determined parameters that are difficult to estimate. Therefore, methods for electronic structure calculation, such as density functional theory (DFT), can be a good candidature for the study of interactions between biomarkers and nanomaterials. The primary research objective of this thesis is to employ DFT for estimating the electronic structure of pristine graphene and doped graphene nanostructures and evaluating their interactions with numerous gaseous molecules and biomarkers by calculating binding energies, electronic structures, and charge transfer. The doped nanostructures exhibit superior sensing capabilities over pristine nanostructures. Further, the synthesis of graphene and its functionalization routes to employ them as Glutathione and Lactate sensors are explored. Later, for experimental proof, the chem-resistive-based sensing devices were fabricated, and sensor parameters were estimated. The high sensitivity and better limit of detection of the fabricated devices make them suitable for devices for point of care applications for detecting various health disorders.

Contents

List of Figures

List of Tables

1

Introduction

Contents

1.1 Introduction

1.1.1 Biosensor

According to the definition given as per IUPAC, "It is a device that uses specific biochemical reactions mediated by isolated enzymes, immunosystems, tissues, organelles or whole cells to detect chemical compounds usually by electrical, thermal or optical signals" [17].

1.1.2 Biosensor system

A biosensor system consists of three components, as shown in Fig.1.1. The first component is the bio-recognition component, also called bioreceptors; these are target biomolecule specific. The second component is the biotransducer responsible for converting interaction between target biomolecule and receptor into a measurable signal. The last component is the electronic readout circuit, it has instrumentation amplifiers and signal conditioning circuits, and a display to show the output [1].

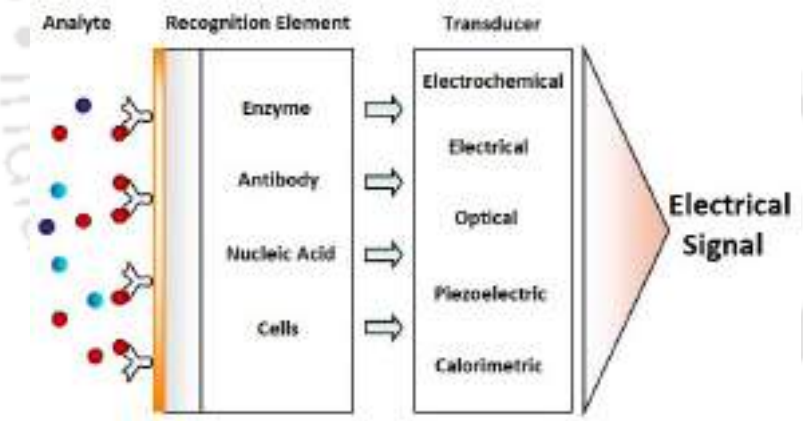

Figure 1.1: Differnet components of Biosensor system [1].

1.1.3 Classification of BioSensors

There are various types of classification of biosensors, as shown in Fig.1.2. The first type of classification is based on the labels used in detection [2]. In the biosensor system, biorecognition or receptor is crucial as it is responsible for interactions with target biomolecule and selectivity. Therefore the second type of classification is based on receptors used. The next major component of the biosensor system is the biotransducer. It is responsible for measuring the interactions between target and receptor, thus affecting the sensitivity. Therefore, the third type of categorisation is based on the type of transducer used [3].

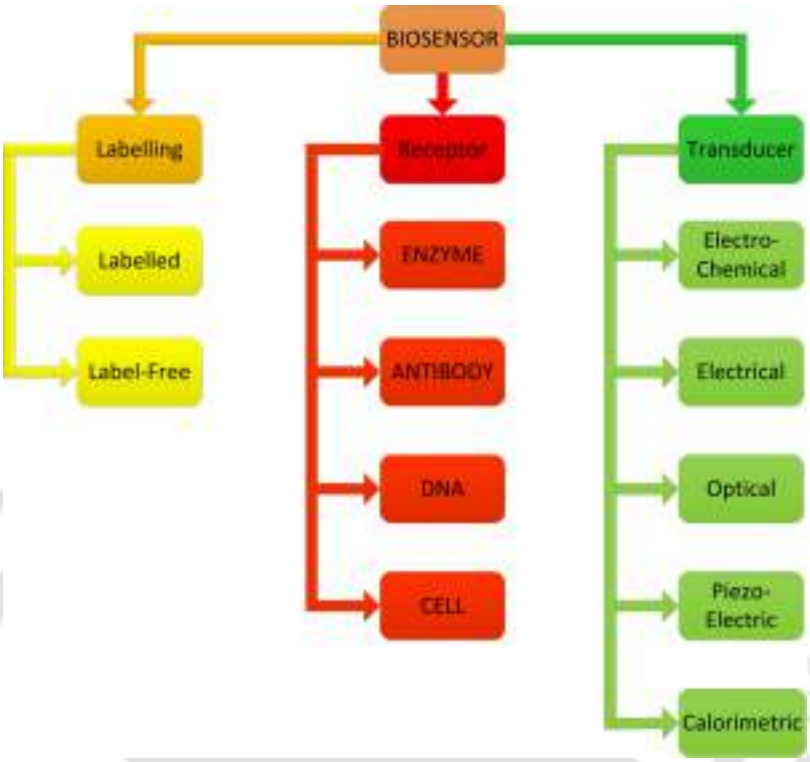

Figure 1.2: Classification of Biosensor system [2]- [3].

1.1.4 Based on labelling

Based on labelling used in the detection, biosensors are classified into labelled and label-free, as shown in Fig.1.2.

Labelled biosensor

Label-based techniques use "tags" or "labels" to detect a particular analyte in the background of other materials. These labels are chemical substances that can result in optical signals for detection.

Label-Free

These are novel techniques in which no labelling is required. In such biosensors, receptors are used to detect a particular biomolecule that is responsible for selectivity. They have some kinetics or thermodynamics associated with target molecules. In this type, minimum assay development is required to detect a target molecule.

1.1.5 Based on Receptor

Based on receptors, biosensor's further classification is shown in Fig 1.2 and discussed as follows:

- Enzyme: In this target biomolecule specific enzymes used, for example, Glucose detection [18]
- Antibody: It is made up of amino acids arranged in a highly ordered sequence. An antigen-specific antibody fits its unique antigen in a particular way, for example, detection of protein [11].
- Nucleic acids: These types of biosensors are based on DNA, RNA and peptide acids. The complementary sections have a very high affinity and hence give good selectivity, for example, detection of S. epidermidis [19].
- Cells: Biosensors that can detect cellular activity or a specific component of a cell. For example, Cell Microenvironment Monitoring [20].

1.1.6 Based on Transducer

Based on transducer type and their mechanisms involved classification of biosensors shown in Fig.1.2 and discussed as follows:

- Electrochemical: Chemical reactions that produce electrons and ions can be monitored with Amperometric and potentiometric techniques. Amperometric is highly sensitive and suitable for mass production, whereas potentiometric involves detection of change in potential. The advanced silicon fabrication technology makes the mass production possible [3]
- Electrical: This includes Conductometric(Impedimetric) and ion-sensitive techniques. Ions or electrons produced during a reaction can cause a change in conductivity. Ion-sensitive is similar to the potentiometric method [21].
- Optical: These types of biosensors are based on optical properties such as diffraction or fluorescence, which is a change in frequency of emission due to absorption or excitation of atoms [22].
- Piezoelectric: Piezoelectric crystals vibrate due to applied electrical signal of a specific frequency, as target molecule binds their frequency varies or due to binding events mass varies and hence stress/strain on crystal varies due to which voltage generated [23].
- Calorimetric (thermometric): The reaction between target biomolecule and receptor causes variation in temperature, which is sensed by temperature sensor [3].

1.1.7 Application of Biosensing

- Medical: Detection of diseases. for example, lung cancer detection and Lab on Chip [24].
- Environmental: Detection of pollutants in the environment. For example, gas sensing [25].
- Industrial: Detection of gases and chemicals. For example, pH detection [26].
- Food technology: Determination of food quality. For example, detection of H_2S gas from food samples [27]
- Space: Space exploration involves detection of gases [27] and chemicals [28].
- Defence: In the prevention of biological warfare. For example, detection of biological agents like H1N1 [29]

1.2 Electrochemical Biosensors

Electrochemical biosensors are the most popular and universally explored. These are based on the reaction between the receptor and analyte molecules, causing current, voltage, or impedance signals. Sensors can be classified as conductometric, amperometric/voltammetric, and potentiometric based on the transduction method.

1.2.1 Chemiresistor

Chemiresistors are materials that are conducting in nature with an inherent resistance/conductance that can experience changes as a response to variations in chemical characteristics of the surrounding environment [30]- [31]. Their sensing action depends primarily on the interaction between receptor and analyte. This interaction can be either Van der Waals, ionic, covalent, hydrogen bonding, or other recognition processes. A simple chemiresistor consists of two electrodes and the receptor material deposited in between them. The inherent resistance of the chemiresistor can be measured, and therefore, the changes in the resistance can be observed upon exposure with the analyte. As the receptor is exposed to the analyte, its constituent atoms interact with the analyte atoms. During which, a phenomenon like material's structure change or charge transfer occurs, which is ultimately refected as a change in the material's resistance. Moreover, the change in the resistance is proportional to the concentration or amount of analyte present. Therefore, the amount of analyte present can be estimated from the calibration curve. The fusion of nanomaterials in chemiresistive devices can enhance

Table 1.1: Literature review for Chemiresistors

Application	Receptor Material	Sensor Parameters	Advantages	Disadvantages	Reference
Detecting Chemically Aggressive Vapors	thin films of single-walled carbon nanotube	LOD for NO_2 250 ppb and LOD for Cl_2 500 ppb	Inkjet-printing of CNT film paper	Response and recovery time is more (a few minutes)	[32]
Detection of a nerve agent simulant gas	Nano-composite of single-walled carbon nanotubes and polyaniline	Response time =5.5 at 10 ppm DMMP LOD is 1ppm	Room Temperature operation	-	[33]
Detection of Chemical Warfare Agent	Nano-composite of conducting polymer and single-walled carbon nanotubes	LOD is 6.5 ppm	Stability in humid air	affected by VOC	[34]
Detection of Lead ions	Nano-composite of Metal Organic Framework and Multi-walled carbon nanotubes	Response Time 100 sec LOD 79nM	Selective towards Lead ions	Requires CV setup for measurement	[35]
Detection of LC3 Protein	Functionalized polypyrrole and carbon nanofiber	-	Simple in operation	20-60 min detection time	[36]
Detection of hepatitis B surface antigen	Graphene-gold nanoparticle composite	LOD 50 pg per mol	Real time detection	complex functionalization process	[37]

their sensing performance (sensitivity, selectivity). Some recent applications with nanomaterials in chemiresistors are given in Table 1.1

1.2.2 Amperometric and Voltammetric Biosensors

These biosensors generally have an electrochemical cell with two or three-electrode configurations, i.e. reference electrode, a counter electrode, and a working electrode.

Table 1.2: Literature review for Voltammetric and Amperometric Biosensors

Application	Receptor Material	Sensor Parameters	Advantages	Disadvantages	Reference
Label-free detection of bacterial pathogens	Carbon screen-printed electrodes modified with gold nanoparticles	E. coli O157 Range 10 10^6 CF/mL LOD CFU/mL	Less detection time	-	[39]
Detection of Hydrogen Peroxide	MoO_3 nanoparticles based electrodes	Detection range 1-5 mM	Nanoparticle possess antimicrobial activity	High temperature synthesis process	[40]
Glutamate biosensor	$Co_3\ O_4$ nanocubes	Sensitivity 20.12uA/mM/cm^2 Linear range 10 to 600uM LOD10uM	Excellent stability	High temperature synthesis process	[41]
Detection of oncomarker CA125 in serum	Anti-CA125 probe immobilized over screen-printed carbon electrode	Linear range 5-80 U/mL LOD 1.45 U/mL	Detection in serum	Stable for only 20 days	[42]
Glucose detection	Cu/rGO decorated buckypaper	Linear range 2-25 mM Sensitivity 480 uA/mM	Flexible electrode Green preparation Low-cost	High temperature reduction process	[43]
Diabetic sensor	Platinum and zinc oxide modified carbon nitride electrode	Linear range 10-110 mM LOD 0.1 uM	Non-enzymatic and selective detection in human blood	High temperature synthesis of electrode material	[44]

In the case of Amperometry, the current is produced due to any electrochemical reduction or oxidation at the surface of the working electrode. At the same time, a constant potential was applied to it with respect to the reference electrode. Whereas, during the Voltammetry, the change in current was measured while varying the applied potential. These techniques are highly sensitive, accurate, fast

and are thus employed in various applications. However, the selectivity, as well as the lifetime of the sensor, depends on the material properties of the working electrode [38]. Therefore, once again, robust composites and modern nanomaterials can help in their improvement. Some recent applications with nanomaterials in Amperometric and Voltammetric sensors are given in Table 1.2.

1.2.3 Potentiometric

Potentiometric biosensors are based on the charge accumulated at the receptor with respect to the reference electrode under zero current. This charge accumulation occurs due to its interaction between analyte and receptor. In order to get a potential signal corresponding to this biochemical reaction, ion-selective electrodes and ion-sensitive field-effect transistors are employed. Some recent literature based on potentiometric biosensors is given in Table 1.3.

Table 1.3: Comparison of Chemiresistors, Voltammetric, and Potentiometric Biosensors

Parameter	**Chemiresistor**	**Amperometric and Voltammetric**	**Potentiometric or FET**
Complexity of Structure	Simple	Complex (2 or 3 electrode system in electrochemical cell)	Simple but may be complex in the case of extended or segregated gate structures
Area Requirements	Less	More area required	Less
Replaceable sensing membrane	No	Yes working electrode can be easily replaced	No, but possible in segregated gate structures
Additional Circuitary requirements	No	No	Yes segregated gate structures
Characterization	Simple I-V characterizationsetup	Cyclic Voltammetry setup	Simple I-V characterization setup with or without instrumentation amplifiers
Additional Remarks	cost-effective	Costly	Moderate cost, Gate terminal can improve sensitivity during measurements

1.3 FET-Based Biosensors

Silicon based semiconductor fabrication technology is very much evolved in the last few decades, which enables the manufacturing of advanced VLSI devices on a nanometer scale on silicon wafer [45]. FET based biosensors are based on a combination of these two in which the chemical and biological methods of recognition are used along with semiconductor fabricated devices to detect and measure the target biomolecule with high accuracy and fast response time [21]. This type of sensor also involves signal processing concepts to improve the performance of sensors. The advantages FET

based biosensors can be summarized as follows:

- Small in size and less weight.
- Fast Response time.
- Low-cost fabrication.
- On-chip integration of sensor array.
- Improved robustness and long sensor lifetime.

FET-based biosensors can be classified in terms of the type of device used as transducer and type of receptors used in those transducers [2]. The detailed discussion is as follows:

1.3.1 Based on Device type

1.3.1.1 ISFET

ISFET was the first miniaturized silicon-based chemical sensor introduced by Bergveld in 1970 [46]. Since then, various field-effect biochemical sensors have been developed. It derives from the insulated-gate field-effect transistor (IGFET) and the metaloxidesemiconductor field-effect device (MOSFET), being the most studied field-effect type device for biosensing [45]. ISFET structure as shown in Fig.1.3 is similar to MOSFET, except the gate metal electrode of the IGFET is replaced by an electrolyte solution which is contacted by the reference electrode, with the insulator placed directly in an aqueous electrolyte solution [4]. The operation of ISFET is analogues to a MOSFET, current equation for both

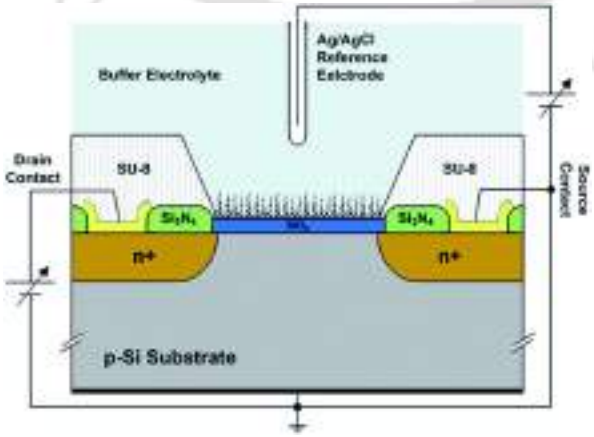

Figure 1.3: ISFET structure [4].

the devices can be given as:

$$I_d = \frac{C_{ox}W}{L}[V_{GS} - V_{TH} - \frac{v_{DS}}{2}]V_{DS} \tag{1.1}$$

But the value of thershold voltage V_{TH} given by Equation is different for both the devices, which is constant in the case of a MOSFET but is a function of the pH of the liquid for the ISFET. Due to this the functionality of both devices varies.

$$V_{TH} = V_{FB} - \frac{Q_B}{C_{ox}} + 2\phi_F \tag{1.2}$$

$$V_{FB} = E_{REF} - \psi_0 - \chi_{sol} - \frac{(Qss + Qox)}{C_{ox}} - \frac{\phi_{Si}}{q} \tag{1.3}$$

Here V_{FB} is the flat band voltage, Q_B is the depletion charge in the silicon, ϕ_F the Fermi-potential, E_{REF} the reference electrode potential relative to vacuum, χ_{sol} the surface dipole potential of the solution, ϕ_{Si} the silicon work function, Q_{ss} is the surface state density at the silicon surface and Q_{ox} the fixed oxide charge. The potential drop in the electrolyte at the oxide-electrolyte interface, ψ_0, is the parameter that makes the flat band voltage a function of the pH, resulting in the ion sensitivity of the device [4]. The advantages of ISFET based sensors are as follows:

- Manufacturing of ISFET is compatible with existing silicon fabrication technology and, hence, can be integrated with signal-processing electronics on the same chip.
- Small in size because of which consumption of sample is less.
- Fast Response.

However, as the sensing membrane is present on the top of the silicon substrate in ISFET, hence, liquid penetration, adhesion problems can degrade the sensor response, reducing lifetime. The typical applications of ISFETs involve pH sensing [26], alkali [47]- [48] and glucose sensing [49]. Some recent literature on ISFET biosensors is given in Table 1.4.

Table 1.4: Literature Review of ISFET

Application	Device Type	Structure	Sensing Material	Sensor Characteristics	Advantages	Dis advantages	Ref.
Arginine Detection	ISFET	n-type substrate (8mmX8mm) Gate Oxide SiO_2/Si_3N_4	Urease	S = 25uA/pH LOD=0.05mM	Good Reproducibility and Stability	changes in Buffer ph cause deflection in current	[50]
Sodium ion detection	ISFET	n-type substrate (8mmX8mm) Gate Oxide SiO_2/Si_3N_4	Fluoropoly-siloxane	S=56-58mV/pNa LOD=0.1mM Response Time=50s Drift=0.3mV/h	Effect of Cloride ion during detection is negligible	Complex structure	[47]
Nitrate ion Detection	ISFET	AlGaN/GaN HEMT structure	tetradodecyl ammonium, 2-nitrophenyloctyl ether with High Mwt. PVC	LOD=1uM S=47.2 mV/pC Selectivity=-5.36 (log K)	No Ref Electrode used	Less sensitive for chloride buffer	[51]
Glucose Detection	ISFET		ZnO based nanorods	S= 53.42 mV/pH S= 33.6 uA/mM (Glucose)	Passivated structure has less Fermi Pinning	Complex structure and fabrication	[49]
Potassium ion detection	ISFET	AlGaN/GaN HEMT L=10-100um W=100um	potassium ionophore with PVC used as membrane	S=52.4mV/Decade Selectivity=-3.1 Response Time=10s	Long life time highly stable	Less selectivity for NH4Cl (-1.21)	[48]
pH Sensor	ISFET	1um i-ZnO over sapphire n-ZnO 80nm as channel	80nm i-ZnO layer	S= 0.55uA/pH S=48.27mV/pH Response Time=12s	passivation removed fermi level pinning	Sensing layer thickness less than Dep. region for sensing	[26]

1.3.1.2 EGFET

EGFET structure is similar to ISFET except the sensing layer is at the end of the extended conductive gate electrode line [52]- [5] as shown in Fig.1.4, i.e. separating the sensing area from the device area. The operation of EGFET is exactly similar to that of ISFET. The surface reactions at

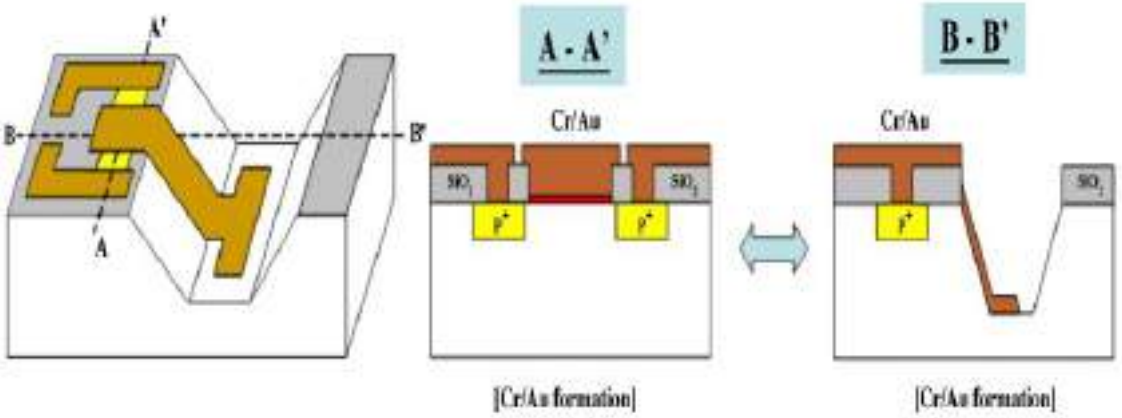

Figure 1.4: Extended Gate FET structure [5].

the sensing membrane cause change in the potential at the membrane electrolyte interface (ψ_0), which is carried to the gate terminal of MOSFET by a conductive layer. ψ_0 is dependent on pH; hence the response of EGFET is also pH-dependent. The EGFETs have several advantages over ISFETs, which are listed below:

- The sensing area is separated from the active device area. It prevents ions from penetrating the channel or moving through the gate oxide, producing a more robust structure for clinical, industrial, and environmental applications.
- It provides convenient packing of the active devices because of a conductive plane which is the extended gate electrode.
- The FET can be tested and characterized in the usual manner without using the solution.
- The sensing area can be readily modified for selective detection of various ions.

Again, there are some shortcomings of EGFET configuration as they can only be used in low impedance membranes. Moreover, sensing membrane replacement is not possible and consume more

area as compared to ISFET. The common applications of EGFETs involve pH Sensing [53], multi-analyte biosensing [52], protein detection [54]. Some recent literature on EGFET biosensors is given in Table 1.5.

1.3.1.3 SEGFET

Many times harsh enviornment cause damage in sensing membrane because of which whole sensing device has to replace with a new one [55]. Hence SEGFET structure came to existence in which replacement of sensing membrane is possible. SEGFET is a type of EGFET in which a metal wire

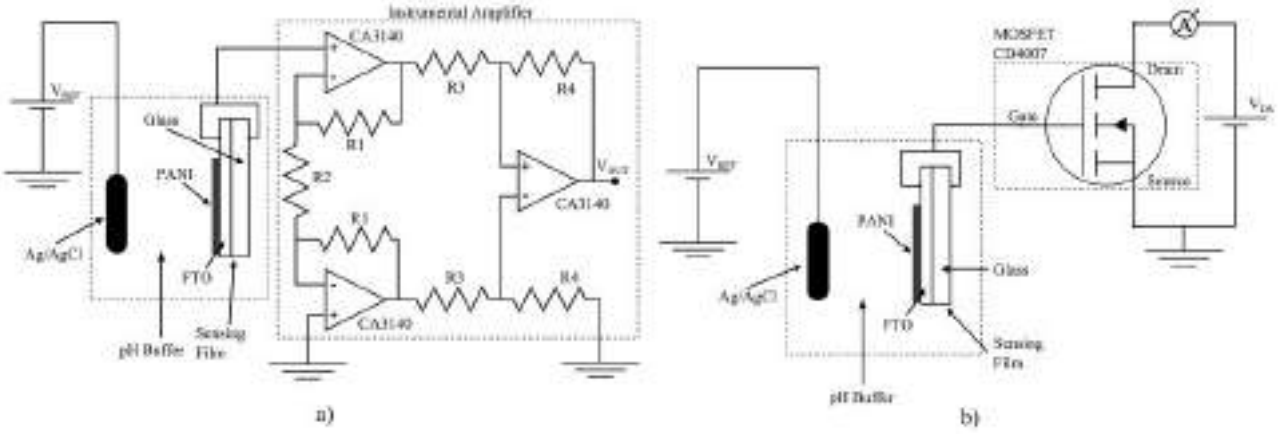

Figure 1.5: SEGFET Structure (a)With Instrumentation amplifier (b) With MOSFET I.C. [6].

connects the sensing film membrane to the gate of a commercial MOSFET [6] as shown in Fig. 1.5. The most common commercial FETs used in SEGFET are the instrumentation amplifier AD620 (used as high impedance unity gain buffer), the operational amplifier LF356 the instrumentation amplifier with LT1167, and the commercial MOSFET-CD4007UB [45]. The operation of SEGFET is the same as that of EGFET.

The commercial MOSFET has good characteristics, and its fabrication process is not a concern. Moreover, the commercial MOSFET is reusable for other applications for which the sensing part may be interchanged. This decreases the cost because the biosensor is disposable. However, SEGFETs are bulky than EGFET and involve complex circuitry. Also, the metal wire that connects the sensing head to MOSFET has to be properly shielded, and if the length of the wire is more, then losses also cause degradation in the sensor's performance. Some applications of SEGFETs are reported in pH sensing [56] and urea detection [57]. Some recent literature on SEGFET biosensors is given in Table

1.5.

Table 1.5: Literature Review of EGFET and SEGFET

Application	Device Type	Structure	Sensing Material	Sensor Characteristics	Advantages	Dis advantages	Ref.
pH Sensor	EGFET	N-MOSFET L=10 um W=30 um	PdO thin Film (130nm) Area = 0.25 cm2	S =62.87mV/pH (linear mode) S =62.87mV/pH (Sat mode) Drift Rate= 2.32mV/h	Temperature effect is negligible	More drift rate as compared to other oxide films.	[56]
pH sensor	EGFET	MOSFET (CD4007UB)	200nm ZnO:Ta layer	S=62.34uA/pH (Sat) S=41.65mV/pH (Linear)	Bio compatible Etching Resistant	Sensitivity is less than 59mV/pH	[55]
pH sensor	EGFET	MOSFET (FET 4007)	In2O3 coated MWCNT (5mmX5mm)	S=36.03mV/pH	Sensitivity variation as annealing temp varies	Sensitivity is less	[53]
Muti-analyte Biosensor	EGFET	n+poly-Si/oxide p-type Si substrate	Nb2O5 film (30nm)	Sensitivities 27.77 mV/pNa^+ 22.3mV/pK^+ 7.71 mV/mM(Urea) 10.89mV/mM(Glu) 32.76mV/pH	CF4 plasma treatment increases the sensitivities	More Exposure to CF4 plasma degrades the responses	[52]
Urea Detection	EGFET	MOSFET (CD4007)	ITO layer on PET substrate (10mmX25mm)	Sensitivities 45.9mV/pH 62.4mV/pC urea Range =0.5-10 mM	Low cost flexible electrode	Less life time more interference of electrodes	[57]
Protein Sensing	EGFET	MOSFET	Au electrodes (D=500nm)	LOD=12nM Range=15.2-1040nM	Label free detection of Protein	Debye length issues	[54]

1.3.1.4 EIS

EIS is the simplest structure of bio-sensor based on the field-effect mechanism. It is derived from MOS-CAP structure [45]. In this type of system, in response to a change of pH, the capacitance of the system varies [58]. The structure of EIS is derived from MOS-CAP in which metallic gate is replaced with electrolyte and a reference electrode as shown in Fig.1.6

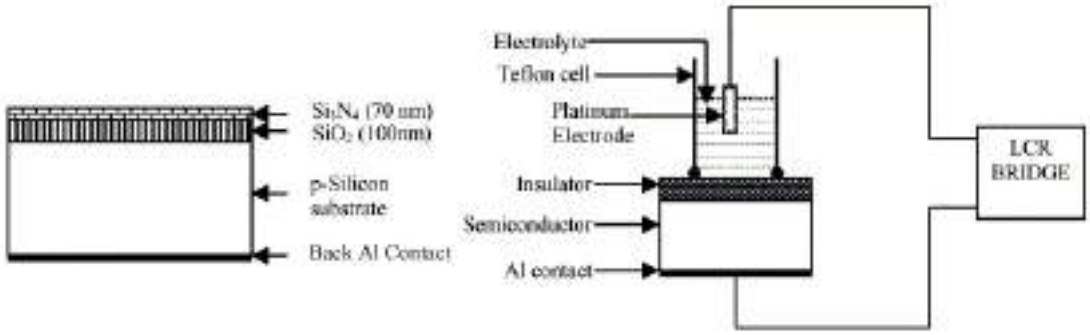

Figure 1.6: (a) EIS-FET Structure (b) EIS-FET characterization Setup [7].

Table 1.6: Literature Review of EIS-FET

Application	Device Type	Structure	Sensing Material	Sensor Characteristics	Advantages	Dis advantages	Ref.
Detection of Creatinine	EIS FET	EIS on 4-inch p-type Si (100) wafers	High-k Tm2Ti2O7 sensing membrane	S=58.45mV/pH S=82.39mV/pC Drift Rate=0.595 mV/h Range=0.01-15 mM	Good Stablility 120Days	slow measurem ent	[59]
Alkali Metal Ion Detections	EIS FET	EIS 4-in p-doped (with boron) single-crystal silicon wafer resistivity 812 ohm cm	Hafnium dioxide (HfO2) thin-film sensing membrane	S=121.6mV/pNa S=98.1mV/pK	proposed low damage plasma treatment hence improved sensitivity	drifts of the fluorinated-HfO2 EIS structure are almost the same as untreated samples	[28]
Estimation of blood analytes (triglycerides and urea)	EIS FET	EIS-CAP silicon wafer (p-type) size of 2.5 cm X 2.5 cm		S=55mV/pH	Sensitivity variation as annealing temp varies	Sensitivity is less	[60]
Detection of DNA	EIS FET	Copper phthalocyanine sandwiched transparent indium tin oxide (ITO)electrode and dielectric (12X40mm2)	ssDNA-immobilized on Ta2O5,OEIS device	S=44.1mV/pH	Low Cost device	Lower limit of detection is,not sufficiently low.	[58]

The operation consists in applying a direct current (dc) polarization voltage via reference electrode to set the working point of the EIS sensor, superimposed to a small alternating current (ac) voltage

(1050 mV), which is applied to the system to measure the sensor capacitance [45].

The EIS sensors are characterized using the C-V measurements [7]. In the C-V curve, three regions can be identified, namely, accumulation, depletion and inversion. For sensing, only the depletion region is considered for analysis, as the curves are shifted due to changes in the electrolyte/insulator interface potential [58]. The EIS sensor has very high precision, but at the same time, the capacitance measurement is a bit complex and difficult. EIS based sensors are reported for the detection of Creatinine [59], alkali metal ion detection [28], estimation of blood analytes [60] and DNA detection [58]. Some recent literature on EISFET biosensors is given in Table 1.6.

1.3.1.5 Comparison between ISFET, EGFET, SEGFET, and EISFET

Table 1.7: Comparison of differnt sensor structures based on FET.

Parameter	ISFET	EGFET	SEGFET	EIS
Complexity of Structure	Simple (MOSFET like)	Complex than ISFET	Most complex	Simple,(MOS-CAP type)
Area	Least	More than ISFET	Sensing area less but require MOS-IC	Least
Replaceable sensing membrane	No	No	Yes	No
Need of Additional Ckt or IC in Sensor Module	No	No	Yes (MOSFET-IC)	No
Characterization ckt	Simple I-V Charecterizaion	Simple I-V Charecterizaion	Simple I-V Charecterizaion with instrumentation amplifiers	Complex C-V Measurement
Life time and Reliability	Less life time and reliability	More life time and reliability than ISFET	More life time and reliability than EGFET	Less Life time and reliability

1.3.2 Based on Receptor used

1.3.2.1 ENFET

The utilization of enzymes as biochemical recognition elements offers high specificity and optimum performance for biosensor application in physiological conditions [9] hence the application of Enzymes

as sensing elements with the existing FET sensor configurations gives birth to ENFET. The architecture of ENFET is very much similar to that of any existing FET based sensor for example ISFET or EGFET. The only difference is that the they contain immobilized enzyme layer on top of Gate dielectric as shown in Fig.1.7 for sensing of biomolecules [8].

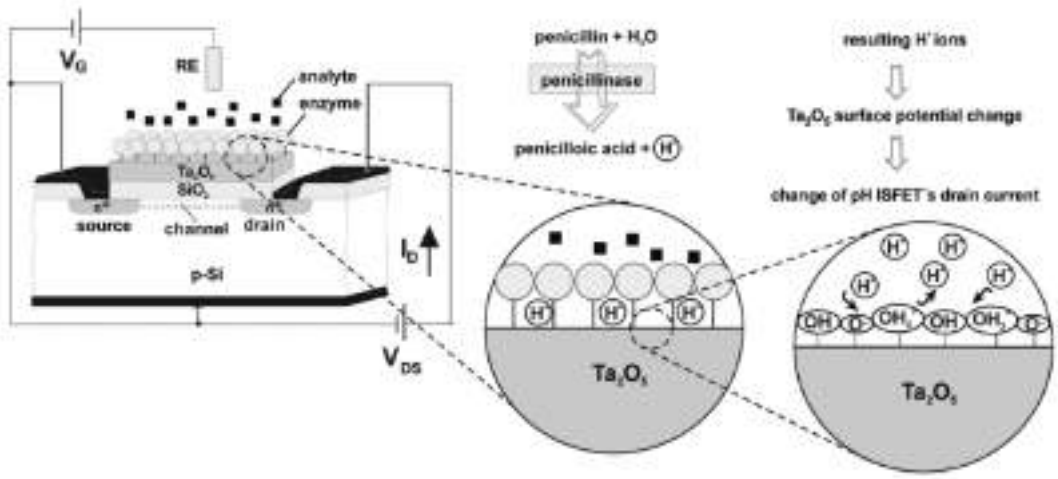

Figure 1.7: ENFET structure and working of penicillin-sensitive EnFET, penicillinase is immobilized on a pH-sensitive Ta_2O_5 surface [8]- [9].

Table 1.8: Literature Review of ENFET

Application	Device Type	Structure	Sensing Material	Sensor Characteristics	Advantages	Dis advantages	Ref.
Urea sensing	ENFET	SEGFET configuration LF356(JFET) input Op-amp as a unity gain buffer	(PVS/N-PANI)3urease (where 3 is the number of bilayers)	S =59mV/pH LOD=0.1-10mM	Increase in the pH sensitivity is achieved after functionalization (around 30 mV) Reproducible sensor	Complex circuitary involed as SEGFET involved	[61]
Lactate ion detection	ENFET	N-channel FET SiO_2/Si_3N_4-gate(100) oriented N-type (500 Ohmcm) silicon wafers	Lactate oxidase (LOD)	S=8to20mV/mM LOD=0.05mM	More sensitive as compared to Platinum electrode Chem-FET Sensor	As buffer concentration increases sensor output decreases	[62]
Penicillinase detection	ENFET	GaN/Al 0.27Ga 0.73GaN 800nm/18nm/1nm HEMT	Penicillinase	S=53.6mV/pH	Reproducibility	Variation of pH or buffer concentration caused the variation in sensor response	[9]

The operation of ENFET is based on the enzymatic reaction between the biomolecule and immobilized enzyme layer. These enzymatic reactions are biomolecule specific hence provides good selectivity in sensor response. Acid or bases are produced as a byproduct of these reactions hence causing a change in pH, this change in pH affects the gate voltage of FET and hence the current through it

varies [9]. Since the response of ENFET is based on highly specific enzymatic reactions, which results in good selectivity in the detection. The Sensitivity is also good as the sensing mechanism involves the change in pH. The ENFET manufacturing is also compatible with existing silicon fabrication. Only the enzyme layer is an additional step. However, the degradation of the enzyme layer cause stability issues and affects the lifetime of the sensor. The reported applications of ENFET involve detection of Bio-Molecules such as urea [61], lactate ion [62] and protein [9]. Some recent literature on ENFET biosensors is also given in Table 1.8.

1.3.2.2 Cell based FET

The concept of cell-based FET sensors utilizing living cells as the sensing element coupled to the metal-free gate of the FET offers the possibility of gaining information about the cells. Cell metabolism parameters are changes in the extracellular pH, the concentration of ions, which can easily be sensed by FET based sensors [20].

Cell-based FET sensors adopt enhancement-type n-channel MOS-FET, which is fabricated by the standard CMOS process. Gate region deposited by a thick layer of Si3N4 is a must because the silicon nitride layer prevents the penetration of alkali ions. This biocompatible passivation layer contributes to device protection and leakage currents reduction. The electrolyte was maintained at ground potential (Ag/AgCl electrode) [10].

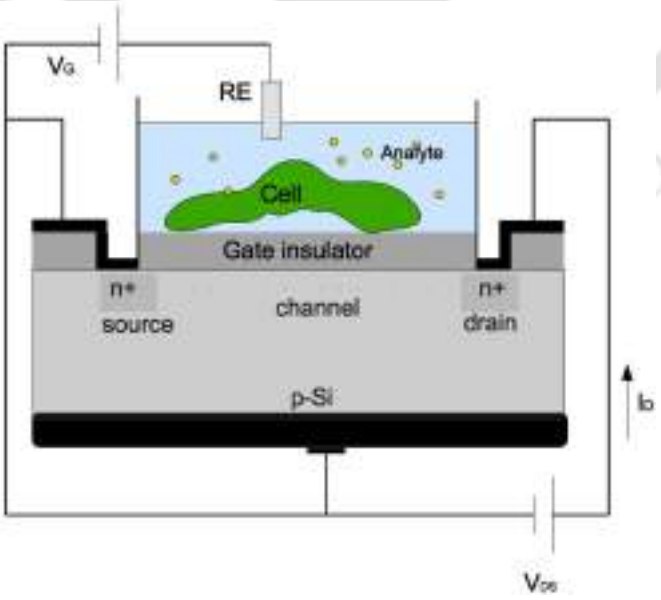

Figure 1.8: Cell Based FET structure [10].

Cells in vitro grow randomly on the surface of the chip. In order to record signals, there are two methods. The first method uses a pipette to suck the cell and then place it onto the sensing area of the chip. This work needs experience and usually has a low success rate. The second method chip is selectively encapsulated in order to expose the gate region [20]. This type of FET sensor mainly focuses on the extracellular pH value in the microenvironment of living cells. It is an important regulator for several cellular functions. The sensing pH mechanism is exactly the same as that of ISFET [10]. A FET structure without a metal gate in an electrolyte has been used to record the electrical activity of individual neuronal cells [20].

Usually, the measurements of cell pH were performed using microelectrodes and magnetic resonance spectroscopy. However, microelectrodes may cause damage to cells, and magnetic resonance spectroscopy is unsuitable for continuous, long-term monitoring of the living cell microenvironment. However, the design of cell-based FET complex as the electrolyte of cell or neuron has to be in direct contact with Gate insulator. The applications of CELL-FET (or cell-integrated extracellular sensor hybrid-system) can be used for many applications such as drug neurophysiology, electrophysiological recording of neuronal activity, and two-way communication between silicon chip and neuron neuronal network ntudy.

1.3.2.3 Immuno-FET

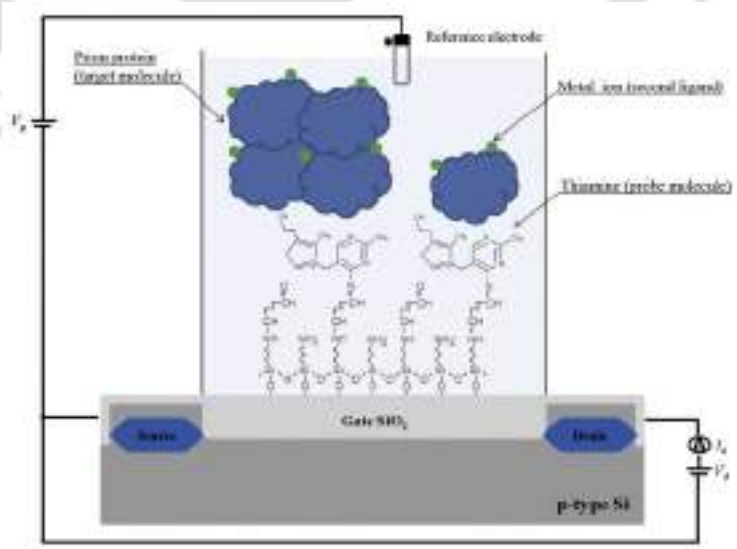

Figure 1.9: Immuno-FET structure [11].

Earlier methods for biomolecule detection such as ELISA, chemiluminescence immunoassay and radioimmunoassay involves complex handling, expensive instrumentation and time consuming methods, respectively [24]. Hence, Immuno-FET was proposed for the cost-effective and rapid detection of biomolecules. In this type of sensors, the gate of the FET is immobilized with an antibody which makes it measure a specific type of biomolecule [19]. They are also known as antibody modified FET based biosensors.

Immuno-FET consist of standard MOS structure fabricated by standard silicon fabrication process but instead of gate metallization an immobilized antibody layer is there for sensing application [24]-[11].

Table 1.9: Literature Review of Immuno-FET

Application	Device Type	Structure	Sensing Material	Sensor Characteristics	Advantages	Dis advantages	Ref.
Lung cancer diagnosis	Immuno FET	ISFET structure W=1000um L=10um	Antigen Cytokeratin fragment 21-1 (CYFRA21-1)and Antigenneuron specific enolase (NSE)	LOD CYFRA-21 = 1ng/ml ΔVg= 8mv(1ng/ml) NSE=100ng/ml vg=8mv (10ng/ml)	Multianlyte detection	FET response degrades as BSA concentration increased	[24]
Human prion protein detection	Immuno FET	ISFET structure (n-type) W=1000um L=10um	Thiamine modified gate	ΔVg= -47mv (400nM)	Introduction of metal ion improves sensitivity and sensor response	-	[11]
Detection of S. epidermidis biofilm and 16S rRNA	Immuno FET	EGFET type	Fibronectin functionalization of Au electrode	S.Aureus 48.9mV/nM S.epidermidis 40.4 mV/nM LOD= $9X10^5$ CFU/ml	Simple passivation packaging and fabrication	Debye length issue and uniformity control of biomolecule on surface	[63]
Apolipoprotein A1 (Protein meaurement)	Immuno FET	EIS	TbTixOy functionalized	S=59.13 mV/pH LOD=12.5 ng/ml	Use magnetic bead improve the response of sensor over debye length	-	[63]

The target biomolecule binds specifically by probe molecule at the gate of MOS. These target biomolecules has some intrinsic charge associated with them. After completion of the binding process, the effective charge varies at the gate. Due to this variation, such as threshold voltage shift (V_{TH}), or variations in the gate voltage (V_G)drain current (I_{DS}) characteristics observed. The incorporation of immobilized antibodies for biomolecule sensing results in excellent selectivity towards the target molecule. It has a fast response time and low sample consumption. However, immobilization of antibodies is complex step and reliability issues are also associated with it. Some of the applications

of Immunosensor involves lung cancer diagnosis [24], protein detection [24]- [63], DNA detection [19]. Some recent literature on ImmunoFET biosensors is also given in Table 1.9.

1.3.2.4 Comparison between ENFET, Cell-FET, and Immuno-FET

Table 1.10: Comparison between ENFET, Cell-FET and Immuno-FET

Parameter	ENFET	Cell-FET	Immuno-FET
Structure	ISFET with immobilized enzymatic layer over Gate dielectric for sensing	ISFET with Cell placed over or cellular liquid in contact of Gate dielectric	ISFET with immobilized probe antigen or DNA over Gate dielectric for sensing
Priciple of Operation	Enzymatic Reactions producing Acid/Base which varies pH sensed by ISFET	ISFET measures change in pH in cellular liquid or ions present in cellular liquid	Charge transfer between target biomolecule and probe molecule hence conductivity of Device varies
Advantages	Enzymatic Reactions are biomolecule specific hence good selectivity and sensitivity	Continuous long term monitoring of Cell without damaging it	Good selectivity and sensitivity due to immobilized antibody
Dis advantages	Enzyme layer immobilization is complex step also its degradation cause issues.	Designing of Cell-FET is complex and cell placing on FET is difficult	Immobilization of antibody is complex step and has degradation issues
Applications	pH, metal ions and Protein sensing	Cell microenviornment monitoring	Diseases detection

1.4 Nanomaterials in FET based Biosensors

Nanomaterials are used in FET based biosensors for improved selectivity and sensitivity as well as the fast response time of sensors [64]. These Nanomaterials are Carbon nanotubes, Graphene and Silicon Nanowires. A detailed discussion of each material with FET technology is given as follows:

1.4.1 Carbon Nanotube (CNT)

CNTs are seamless hollow tubes composed of rolling graphite sheets. According to the layer number of graphite sheet, the CNTs can be divided into single-walled (lengths 0.753 nm and diameter 150 um) and multi-walled (lengths 2-30nm and distance between layer 0.42nm) carbon nanotubes

[12]. Excellent electrical(mobility of carriers very high) and mechanical properties(strength 10-60GPa, Young's Modulus 1TPa) of CNT make them suitable to be used along with already existing FET based biosensors hence producing sensors with improved responses and robustnessCNTR3.

1.4.1.1 CNT based FET (CNT-FET)

The CNT-FET structure comprised of noble metal (gold or platinum) electrodes were lithographically patterned atop an oxide-coated, heavily doped silicon wafer, and a single-walled CNT was deposited atop the electrodes. The metal electrodes served as the source and drain, and the CNT was the active channel. The doped substrate served as the gate electrode, separated from the CNT channel by a thick (100nm-200nm) oxide layer. These CNT can be modified according to target biomolecule; this process is called functionalization of CNT [65]. Advanced CNT based structures involve the capillary formation of CNT enables 3-D structures. These structures provide large surface area and active sites for chemical actions hence exhibit increased sensitivity [66].

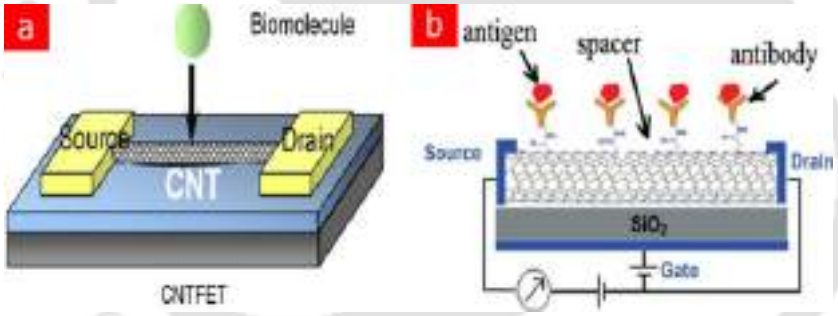

Figure 1.10: (a) CNT-FET based biosensor (b) Working of CNT-FET biosensor, schematic taken from the literature [12]

CNTs are functionalized to respond and detect a particular biomolecule. Once such a biomolecule comes in contact with such a CNT, it will attach to the CNT. This process is termed "Binding". During the binding event, the charge transfer takes place due to which the device characteristics varies [67]. The major advantages of CNT-FET are as follows:

- High sensitivity, because of the large surface area ratio and hollow pipe.
- CNTs can be used to the immobilized enzyme, which keeps high biological activity and thus very high selectivity.
- Fast response time, CNTs have an outstanding ability to mediate fast electron-transfer kinetics,

hence promoting the electron-transfer reactions

- Highly stable due to superior mechanical properties and longer lifetime.

However, despite the above-mentioned advantages, there are a few shortcomings of CNT-FET mentioned below:

- It is not easy to control the size of CNTs in the manufacturing process.
- In the existing technology is also challenging to make cost-effective mass production of CNTs and achieve high purity. Purity is crucial for CNT-based biosensors, but it is hard to obtain it. That is why the current market price of CNTs is too high for any practical commercial application.

The significant applications of CNT-FETs are in label-free detection of diseases, DNA hybridization [68] at the single-molecule level other than this various biomolecule such as protein [66], amyloid in human serum [69] and ph-sensing [70] and gas sensing [25]. Some recent literature on CNTFET biosensors is given below in Table 1.12.

Table 1.11: Literature Review of CNT-FET

Application	Device Type	Structure	Sensing Material	Sensor Characteristics	Advantages	Dis advantages	Ref.
pH sensing	CNT FET	SEGFET MOSFET (CD4007UB)	Oxygen Plasma functionalized MWCNT (4mmX4mm)	S=55.7mV/pH Drift Rate=1.36 mV/hr(pH=7)	Good sensitivity Flexible electodes	Complex circuits involved	[70]
Gas Sensing	CNT FET	CNT on Si substrate With Silver Contacts	CNT Dia=4.52um Length=45nm with Au nanoparticle	CO2 S=1.2 for 50ppm S=3.4 for 800ppm	Good sensitivity due to Au nanoparticle	Bad Selectivity with Ethanol	[25]
DNA Hybridization Detection	CNT FET	CNT on Si substrate L=10um W=50um Au contact	Probe DNA functionalized on CNT	Shift in Vth=60mV for 1uM taget	Good Selectivity between 10-100nM Conc.	Sensitivity is bad for lower conc.	[68]
Protein Detection	CNT FET	Vertical CNT Forest over Gate oxide of NMOSFET	Vertical CNT Forest functionalized with ss-DNA aptamer	S=33uA/uM	Low cost Sensitivity improvement by modifying CNT forest density	Complex structure	[66]
Detection of Amyloid beta in human serum	CNT FET	CNT over Si/SiO_2 Substrate L=5um W=10um	Probe antibodies Functionalied over Au on top of CNTs	LOD=1pg/ml	Excellent LOD		[69]

1.4.2 Silicon Nanowires (SiNW)

Silicon Nanowires are 1-D nanostructures of silicon atoms. Their synthesis is classified as top-down and bottom-up approaches [71]. SiNW is 1-D material hence a high surface to volume ratio. Bandgap, as well as effective masses of electrons and holes, is dependent on the width of nanowire [72]. SiNW is quite popular as a channel material in FET based sensors, i.e. SiNW-FET.

1.4.2.1 SiNW based FET (SiNW-FET)

SiNW-FET structure is very much similar to that of CNT-FET, as explained in the previous section. The only difference is that SiNWs replaces the CNTs in the channel region of FET. Doped SiNW in between source and drain can cause npn or pnp structures depending upon the doping of nanowire. The working of SiNW-FET involves the binding event of the target biomolecule with nanowire. In the binding process, charge transfer occurs between them; therefore, the conductivity of nanowire changes. Hence the current varies through the FET.

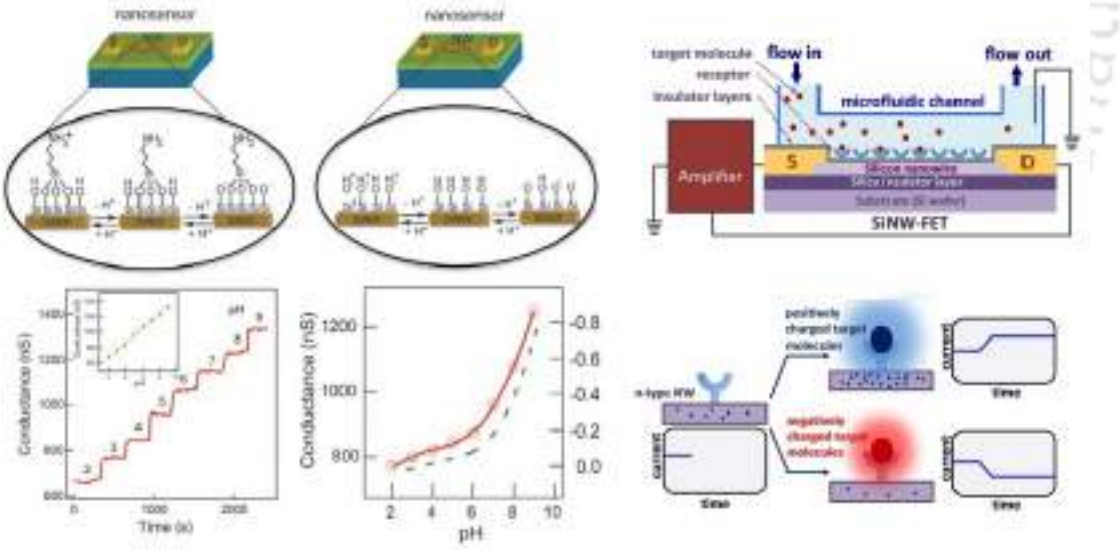

Figure 1.11: SiNW-FET structure, schematic taken from the literature [13].

Due to the 1-D nature of the SiNW, they possess a very high surface to volume ratio; hence the sensitivity of the sensor is much higher. Also, the functionalization of SiNW can be done easily, which increases the selectivity towards specific biomolecules. The fabrication of SiNW-FET is also compatible with standard silicon fabrication steps, which is an additional advantage of these types of sensors. However, the synthesis of SiNW is a slow and complex process. The reported applications

of SiNW-FET consist of DNA detection [29]- [73], pH and alkali metal ion sensing [74], flexible cell recording [75]. Some recent literature on SiNWFET biosensors is given below in Table 1.13.

Table 1.12: Literature Review of SiNW-FET

Application	Device Type	Structure	Sensing Material	Sensor Characteristics	Advantages	Dis advantages	Ref.
DNA detection (H1N1,H5N1)	SiNW FET	SiNW-FET device commercially available (100) SOI wafers	SiNW triangular cross section sizes ranging from 20 to 200 nm 5'-carboxyl-modified single-stranded DNA	LOD=1fM	Label free ultrasensitive DNA detection	-	[29]
Potassium Ion Sensing (pH sensing)	SiNW FET	SiNW-FET p-Si SOI wafer 85 nm, resistivity of 8.5-11.5 Ωcm and145 nm thick buried SiO_2 layer	SiNW coated with hafnium oxide (HfO2) and aluminum oxide (Al2O3)	LOD=10mM S=56mV/pH	Good sensitivity (near-Nernstian)	LOD is large	[74]
Detection of Small Nucleic Acid Oligomers (ssDNA)	SiNW FET	SiNW-FET SOI wafers p-type1015/cm2 buried oxide 1450 A and top silicon thickness of 550 A	SiNW coated with hafnium oxide (HfO2) functionalized with miRNA(miR10b)	S=55.8mV/pH LOD = 100fM	High stability and robustness	-	[73]
Flexible electrical recording from Cell	SiNW FET	p-type silicon NWs based FET	SiNWFETs with cells in which optically transparent PDMS/cell substrates	SNR greater than %	Robust NWFET/cell interface	-	[75]

1.4.3 Graphene

The International Union of Pure and Applied Chemistry (IUPAC) defines graphene as "a single carbon layer of the graphite structure, describing its nature by analogy to a polycyclic aromatic hydrocarbon of quasi-infinite size".

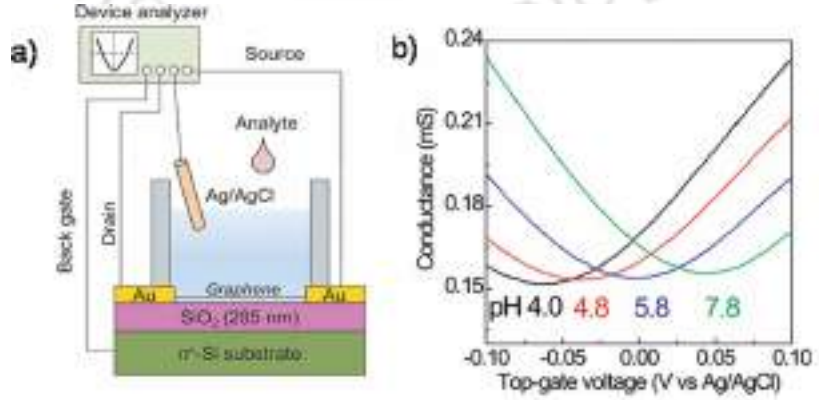

Figure 1.12: (a)Graphene-FET structure (b) Variation in conductance for different pH, schematic taken from the literature [14].

Graphene is an allotrope of carbon in the form of a two dimensional, atomic-scale, hexagonal lattice (honeycomb lattice) in which one atom forms each vertex [76]. The zero bandgaps within the structure enable its ultrahigh electron mobility (200,000 $cm^2\ V^{-1}\ s^{-1}$), which is much higher than that of carbon nanotubes (CNTs). It has excellent thermal (4,000 $Wm^{-1}\ K^{-1}$) and outstanding electrical conductivities(3,189 S cm^{-1}). It also possesses an extremely high surface-to-volume ratio (2,600 $m^2\ g^{-1}$) and ultra-high capacitance. Moreover, the exceptionally low electronic noise of graphene enables the possibility of the sensitive detection of various analytes using graphene [76].

1.4.3.1 Graphene-FET

Graphene is also incorporated with the FET structure for biosensing applications. They provide more sensitivities, selectivity and fast response time as compared to silicon-based FET configurations. A graphene field-effect structure is constructed from bottom to top as follows: substrate, graphene layer as the channel (either monolayer, bilayer or few-layer graphene), a dielectric layer and source-drain electrodes and top gate electrode [65]. A structure with substrate contact and a top gate is used to allow more control in electronic properties. Contact metals should be chosen such that the contact is ohmic. Secondly, a metal that has a work function close to the semiconductor bandgap as possible [77] should be chosen. Some recent literature on GrapheneFET biosensors is given below in Table 1.13.

Functionalization of the graphene layer is also done to maximize the selectivity towards the target biomolecule. In a graphene field-effect transistor (GFET) the graphene sheet acts as the channel between two metal source and drain electrodes which lie atop an electrical insulator such as SiO_2. When charged biological molecules bind on the surface of the semiconducting graphene sheet in the GFET, there is a measurable change in resistance [27]- [79]. The major advantages of Graphene-FET are: Graphene has a 2-D structure, hence more area is available for absorption per volume leading to high sensitivity. GFETs possess a fast response time and are smaller in size (low consumption of sample). Functionalization of Graphene causes more selectivity in the detection of target. Owing to the high conductivity of graphene, a low level of excess (1/f) noise is expected due to thermal switching. Also, thier excellent mechanical properties enable robust sensor and hence longer lifetime. However, apart from the advantages mentioned above, Graphene-FET has a few shortcomings, which arise from costly and complex synthesis processes and difficulty in controlling the size (or shape) of graphene (sheet or nanoribbon). The reported literature indicates that the Graphene-FET are

Table 1.13: Literature Review of Graphene-FET

Application	Device Type	Structure	Sensing Material	Sensor Characteristics	Advantages	Dis advantages	Ref.
Proton sensing	Graphene FET	rGO EGFET on ITO coated Glass Electrode L=800um W=50um	Indium-Tin Oxide electrode	S=43-50mV/pH	Good packing density for active devices	Sensitivity is less than 59mV/pH Impurities affect the response	[78]
H2S Gas Sensing	Graphene n-Si Diode	Graphene over nSi Substrate	Graphene layer	Minimum sensitivity 34.88-35.62 at 10ppm H2S	Good sensitivity and selectivity reproducible and fast	-	[27]
Protein(BSA) Sensing Application	Graphene FET	Graphene over SiO_2/Si Substrate	Anti-BSA probe immobilized over Gate	S=30uS/pH	LOD in Pico-Molar range	High conc sensitivity decreases	[79]
Biomolecule (DHEA-S) Detection	Graphene FET	Graphene over SiO_2/Si Substrate Au contact	DHEA-S aptamer functionalized Graphene	LOD=44.7nM SNR=20dB	label-free detection with high sensitivity	Device malfunction if Id exceeds 40uA	[80]
Metal Ion Detection	Graphene FET	rGO micropatterns on substrate W=10um L=1cm	Functionalized with calmodulin, metallothionein	LOD=1uM (Ca ion) SNR=20-30dB LOD=1nM(Hg ion) SNR=25-30 db	Multiple ion detection with good SNR	Bad selectivity for combination of various ions	[81]

excellent platforms for DNA detection [79], proteins [79] and metal ions [81].

1.4.3.2 Comparison between CNT-FET, SiNW-FET, and Graphene-FET

1.5 Modelling of FET based sensor Devices

The nanomaterial such as graphene in a FET based sensor acts as the channel between two electrodes, which lie atop an electrical insulator such as SiO_2. Applying back-gate bias shifts the fermi level and hence concentration varies without doping. When the Fermi level coincides with the energy of the Dirac point, the graphene is neutral, and conductivity is a minimum. If the Fermi level is greater than zero, then the nature is n-type nature, and when it is less than zero, the nature is p-type. In biosensors, doping can be induced by surface contamination. These impurities make the graphene n-type or p-type and shift the charge neutrality point or Dirac point away from zero [78].

Table 1.14: Comparison between CNT-FET, SiNW-FET and Graphene-FET

Parameter	CNT-FET	SiNW-FET	Graphene-FET
Structure	CNTs as channel material of FET (1D/2D and 3D sensing structure)	SiNW as channel material of FET (1D/2D and 3D sensing structure)	Graphene as channel material of FET (2D sensing structure)
Priciple of Operation	Binding event between target and CNT can cause transfer of charge	Binding event between target and SiNW can cause transfer of charge	Binding event between target and Graphene can cause transfer of charge
Advantages	Functionalization easy High sensitivity,response time and highly robust less surface fouling	Fabrication is easy as only silicon involved High sensitivity	Functionalization easy High sensitivity,response time and highly robust low thermal noise
Dis advantages	Fabrication is complex and costly Size control also difficult	Functionalization is difficult inferior mechanical and electrical properties	Sensing limited by debye screening length and only 2-D sensing structure
Applications	DNA,protein and ph and gas sensing	Protein, DNA and Ion cell detection	Metal Ion, DNA protein detection

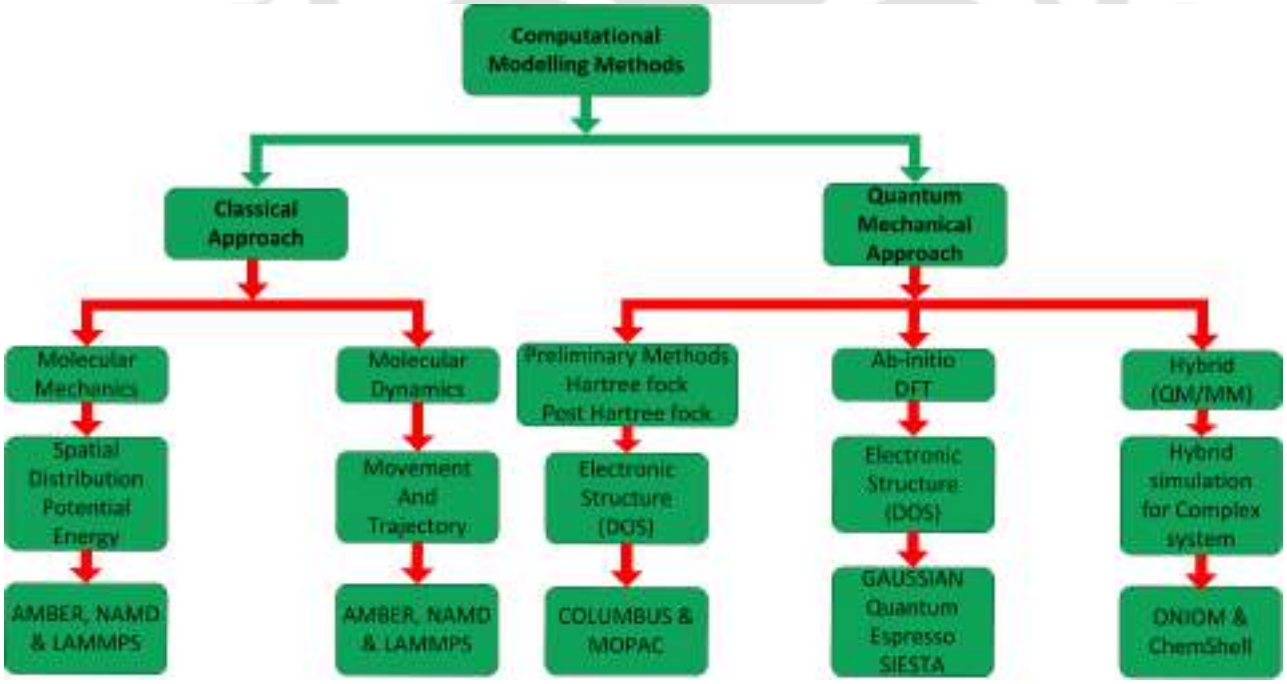

Figure 1.13: Classification of methods for receptor designing [2]- [3].

In order to model the graphene based FET sensor, there are various methodologies; the most common graphene-electrolyte interface capacitance methodology is described as follows:

- Graphene-Electrolyte Interface Capacitance Model: Due to the difference in electrochemical potential, when graphene is immersed in the electrolyte, charges accumulation occurs, forming a double layer. This double layer has capacitance associated with its modelling of this involves using a parallel plate capacitance in series with Quantum capacitance [82].

- Graphene based I-V Model: The I-V characteristics modelling can be done similarly as for a MOSFET, except modified capacitance in this case [83].

The above methodology is only suitable in the case of liquid gating but not applicable otherwise, such as in the case of gas sensing. Moreover, the traditional methodologies based on experimentally determined parameters for modelling failed to estimate and predict the nature of the interaction between the analyte molecule and receptor layer (channel layer) of the sensor without performing the experiments. The methodologies to estimate or predict the interaction between the analyte and receptor layer can be broadly classified into two categories (these methods can be used to design receptor or study receptors), and their further subdivisions are as follows:

- Classical methods

- Quantum mechanical methods

1.5.1 Classical

Classical methods, as the name suggest based on Newton's equation of motion. They can be further classified into two types as follows:

1.5.1.1 Molecular Mechanics

Molecular mechanics is used to performing structural analysis in large molecular systems. It applies the laws of classical mechanics in order to model molecular systems. In this process, the potential energy of a system is calculated by the force fields, which is a functional form and parameter sets are used to calculate the potential energy of the system. These parameter sets can be obtained from experiments or sometimes quantum mechanical calculations. In short, molecular mechanics assumes an atom as a particle with a radius, charge, and polarizability. These parameters are estimated through quantum mechanical calculations and experiments. The bond formation and interaction can be visualized as a spring connection of the atoms with an equilibrium distance equal to the experimental bond lengths [84].

1.5.1.2 Molecular Dynamics

In this type of simulation, the physical movement of a system consists of atoms and molecules studied. In order to study the dynamics, a system of atoms and molecules is allowed to interact for finite time duration, and their trajectories are determined by numerically solving Newton's equations of motion. For a system of interacting particles, where forces between the particles and their potential energies are calculated using interatomic potentials or molecular mechanics force fields [85].

1.5.2 Quantum-Mechanical

1.5.2.1 Preliminary Approaches

Schrodinger's equation was discovered in 1926; soon after that, D. R. Hartree introduced the self-consistent field method to calculate approximate wave functions and energies for atoms and ions. In this theory, the total wavefunction of the system is expressed as a product of one-electron orbitals. However, this violates the principle of antisymmetry of the wave function i.e. valid Electronic Wave-functions must change sign upon exchanging the coordinates of any two electrons hence not following Pauli exclusion principle [86]- [87].

Later on, Hartree theory was modified by using Slater determinant, which constructs the overall wavefunction from single electron wavefunction in such as way so that they will be antisymmetric. However, Hartree-Fock removed the major failing of the Hartree theory, but since electron-electron interactions are not appropriately incorporated in this theory, hence this theory is also not accurate [88].

1.5.2.2 DFT

In 1963, P. Hohenberg and W. Kohn, in their famous paper, suggested that electron density can be used to determine the properties of the system. Later on, in 1965, Kohn and Sham formulated the modern Density functional theory for which Kohn was awarded Nobel Prize in 1990. The electron-electron interaction is incorporated with the help of the exchange and correlation function, which is based on different approximations such as LDA or GGA. Today, DFT is very accurate due to the availability of better models for electron-electron interactions, but it is computationally very expensive [87].

1.5.2.3 Hybrid Methods

Quantum mechanical methods are highly accurate, but at the same time, they are computationally very expensive. The classical methods are fast but not accurate. Hence, the need for such a method was felt in which the advantages of both the methods are present. These methods are called Hybrid methods. Warshel and Levitt first suggested it in 1976, for which they were awarded Nobel Prize in 2013 [89].

Semi-empirical methods are also faster than DFT. They are based on Hartree-Fock formalism but involve approximations and parameters from experimental data. These methods are suitable for moderate size organic molecules [90].

1.5.3 Literature survey on modelling and interaction estimation between analyte and receptor layer i.e. receptor designing

Table 1.15: Few examples of receptor designing from literature

S. No.	Application	Process/Theory	Software	Ref
1	Polymer for Caffeine	MM used to determine binding energy of different polymers with Caffeine	Molecular modeling of structure by Hyperchem 7.5 Binding energy byAMBER-MM	[91]
2	Polymers for 2,4-dichloro phenoxyacetic acid	Study of solvent effect on complex formation by MD simulation	AMBER-MD	[92]
3	Detection of TNT	Ab inito DFT study for molecular interactions of TNT with acrylic acid, and ethylene glycol dimethacrylate	Gaussian-03	[93]
4	Specific monomer for harmane	Investigate the intermolecular interactions between harmane and the selected functional monomers: methacrylic acid and 2-hydroxyethyl methacrylate	Geometry optimization : Semi-emprical PM3 methdos Binding Energy : DFT(B3LYP)Gaussian-03	[94]
5	Sugar transfer	Correlation between macroscopic sugar transfer and nanoscale interactions in cation exchange membranes	NW-Chem	[95]

1.5.4 Density Functional Theory

Electronic structure calculation is a prime interest of scientists. In early 1920, Neils Bohr theoretically determined the energy levels of the hydrogen atom. Later, after the formulation of the Schrodinger wave equation in 1925, published in 1926, the electronic structure of hydrogen-like atoms was explained from quantum mechanics. Application of the Schrodinger equation in atoms with more than one electron is critical due to the presence of electron-electron interactions. Just after the discovery of quantum mechanics, many theories came into the picture, which is based on single-particle Schrodinger equation along with approximation for the electron-electron interactions. However, these theories were not able to depict the experimental results accurately. In the early 1960s, Density functional theory was invented, which was also based on the independent particle method, but now density plays the central role. Also, It incorporates modified models for electron-electron interactions, which makes it highly accurate [87].

1.5.4.1 Need of DFT

If we want to study a system with a well-defined collection of atoms, then the fundamental things we would like to know are the energy of the system and how it changes as the atomic positions changed. As the atomic nucleus is much heavier than electrons, electron response is much faster than the nucleus as the surrounding changes. Hence, according to the Born-Oppenheimer approximation, we can divide our study into two parts. The first part considers fixed positions of the atomic nuclei, then solving for the equations that describe the electron motion, i.e. electron motion in the field of a fixed nucleus. By solving this part, we get the ground state energy configuration of the system. The second part of the study includes the energy change as the nucleus(or atom) moves using potential energy surfaces, i.e. molecular dynamics [86].

Now we will try to solve Schrodinger's wave equation in order to show the complexities involved. Assuming that number of electrons is more than number of nucleus in the system, the Schrodinger equation for a system of N-electrons can be written as:

$$\left[\frac{h^2}{2m}\sum_{i=1}^{N}\nabla_i^2+\sum_{i=1}^{N}V(r_i)+\sum_{i=1}^{N}\sum_{j<i}^{N}U(r_i,r_j)\right]\psi=E\psi \tag{1.4}$$

Here, m is the mass of the electron, and "h" is the plank's constant. The three-term on the left-hand side of the equation is the kinetic energy of each electron, the interaction energy between each

electron and the collection of atomic nuclei, and the interaction energy between different electrons, respectively. The solution of the above equation gives electronic wave function ψ_n with the associated eigenvalues E_n. The overall wave function of N-electrons, which depends on the positions of N-electron, is ψ with the corresponding energy of the system given by E. According to Hartree, overall ψ can be approximate as a product of individual ψ_n i.e.

$$\psi = \psi_1 \times \psi_2 \times \psi_3 ... \times \psi_n \tag{1.5}$$

Let us assume that the above equation is solved for a water molecule with 18 electrons, i.e. N=18. To evaluate the ψ, one has to calculate three positional coordinated of 18-electrons; hence ψ is dependent on 54 variables (18*3) which are very difficult to solve. Now, look at the third term in the equation, which includes electron-electron interaction, which causes simultaneous solution of all the other electron wave functions to get the individual electron wave function.

From the above arguments, it is clear that we cannot calculate individual wave functions directly. Hence, many theories and approximations are done over time, including Hartree and Hartree-Fock method and semi-empirical methods.

1.5.4.2 DFT Formulations: Hosenberg-Kohn and Kohn-Sham approach

Hohenberg-Kohn Theorems

Theorem-I

For any system of interacting particles in an external potential $V_{ext}(r)$, the potential $V_{ext}(r)$ is determined uniquely, except for a constant, by the ground state particle density $n_0(r)$ [15].

Corollary-I: Since the Hamiltonian is thus fully determined, except for a constant shift of the energy, it follows that the many-body wavefunctions for all states (ground and excited states) are determined. Therefore all properties of the system are entirely determined given only the ground state density $n_0(r)$.

Theorem-II

A universal functional for the energy E[n] in terms of the density n(r) can be defined, valid for any external potential $V_{ext}(r)$. For any particular $V_{ext}(r)$, the exact ground state energy of the system is the global minimum value of this functional, and the density that minimizes the functional is the exact ground state density $n_0(r)$ [15].

Corollary-II: The functional E[n] alone is sufficient to determine the exact ground state energy and density. In general, an excited state of electrons must be determined by other means.

The above theorems suggest that one can relate the properties of the system from ground-state density. However, because of two major reasons, it was complicated to proceed from the density:

- Direct relation between density and physical properties is not known.
- The only way to solve the Hosenberg-Kohn functional is to express it into N-wavefunctions form.

Kohn-Sham approach

The above problems are solved by the Kohn-Sham approach, which involves independent particles, but an interacting density [15]- [16]. The approach is based on the following assumptions:

- The exact ground state density can be represented by the ground state density of an auxiliary system of non-interacting particles.
- The auxiliary Hamiltonian is chosen to have the usual kinetic operator and effective local potential Veff(r) acting on electron.

Now density of auxiliary system can be written as:

$$n(r) = \sum_{i=1}^{N} |\psi_i|^2 \tag{1.6}$$

Hence using the Eqn.(2.3) and the Kohn-Sham approach, the ground state energy functional can be written as:

$$E_{KS} = \frac{1}{2}\sum_{i=1}^{N} |\nabla\psi_i|^2 + \int dr V_{ext}(r)n(r) + \frac{1}{2}\int dr^3 dr'^3 \frac{n(r)n(r')}{r-r'} + E_{N-N} + E_{XC}[n] \tag{1.7}$$

Where, E_{N-N} is interactions between nucleus. The above eqn.is solved using variational principle and modified as:

$$\left[-\frac{1}{2}\nabla^2 + V_{ext}(r) + V_{Hartree}(r) + V_{xc}(r)\right]\psi_i = \varepsilon_i\psi_i \tag{1.8}$$

The above equation is an independent particle equation with a potential that is solved self-consistently with the resulting density.

1.5.4.3 Approximations

Kohn and Sham, in their paper, mentioned that solid could be considered close to the limit of the homogeneous electron gas. In that limit, exchange and correlation effects can be considered local, proposing a local density approximation. In LDA, exchange and correlation energy are integral over the entire space with the exchange, and correlation energy density at each point is assumed to be the same as in a homogeneous gas with that density [86].

1.5.4.4 Applications

- Determination of energy and structure of molecules (force, stress etc.)
- Electronic structure calculation (DOS, E-k plot, dipole moment etc.)
- Determination of transition states during a chemical reaction.

1.5.4.5 Flow Chart for DFT Calculation

The algorithm for the DFT calculations followed by the computational software are as follows:

1.6 Research Motivation and the Problem Formulation

Graphene is very popular nano-material because it possesses ultrahigh electron mobility (200,000 $cm^2V^{-1}s^{-1}$) (which is much higher than that of carbon nanotubes), excellent thermal conductivity (4,000 $Wm^{-1}K^{-1}$), and outstanding electrical conductivity(3,189 Scm^{-1}). Moreover, it has an extremely high surface-to-volume ratio (2,600 m^2g^{-1}) and ultra-high capacitance. These superior properties, along with the exceptionally low electronic noise, enable the sensitive detection of various analytes using graphene.

Graphene incorporated within the FET structures can provide better sensitivities, selectivities, and fast response time than traditional FET-based sensors. Moreover, The doping and functional modification of the graphene layer can improve the sensing capabilities towards the analyte molecule. Therefore, the primary motivation behind this study on graphene is to understand the interaction and sensing capabilities of graphene towards various analytes. A thorough study and analysis of the interaction between them can lead to improvement in sensor performance. As per the methodologies described in the previous section, a few theoretical studies have been reported in the literature which

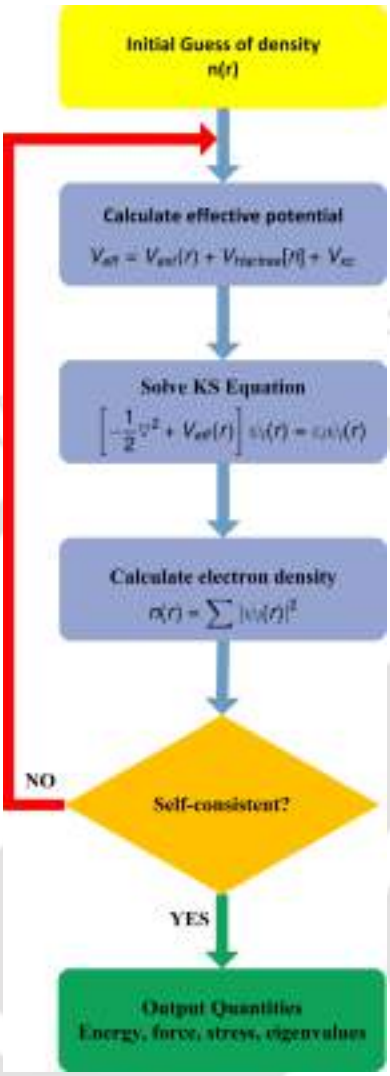

Figure 1.14: Flow chart for DFT calculation [15]- [16].

can estimate and predict the nature of the interaction between analyte and graphene layer. Based on the literature following problems have been identified for further investigation:

- The reported modelling or simulation studies on the interaction between analyte molecule and graphene layer were mainly based on parameters estimated from experiments. Therefore the nature and cause of interaction were not thoroughly investigated. Therefore, there is a scope for further investigation on this front.
- Once the nature and the cause of the interaction are estimated, there is a possibility of improving the same with doping or functional modification of the graphene.

- Synthesis of graphene and functionalized graphene along with the characterization.
- Fabrication of graphene-based sensors for biosensing applications.

In summary, the objectives and direction of this thesis include: studying the electronic structure calculations for graphene and doped graphene structures. After estimating electronic properties, these structures will be explored for small gas molecule adsorption. The same structures can also be employed for bio-molecule adsorption. The thesis will then describe the synthesis and characterization of graphene and functionalized graphene, and finally, the fabrication of graphene-based sensors will be done for bio-sensing applications. The detailed and chapterwise details are provided in the next section:

1.7 Organization of the Thesis

The thesis is organized into the following chapters. The content of each chapter is summarized as follows:

- *Chapter 2*: This chapter employs Density Functional Theory to describe the interactions between gaseous air pollutants, including di-atomic (CO and NO), tri-atomic (CO_2 and HCN), and poly-atomic (HCHO and $COCl_2$) species, and Ti-doped zigzag graphene nanoribbon (ZGNR) structures.
- *Chapter 3*: This chapter elaborates the study of the interaction of Phosgene ($COCl_2$) on two configurations of Titanium doped Graphene Nanoribbons (GNR)- Armchair GNR and ZigZag GNR. In some cases, the splitting of the molecule was also observed. This study was further extended to two other molecules, one with an S-Cl bond ($SOCl_2$ -Thionyl Chloride) and one with an O-Cl bond ($POCl_3$).
- *Chapter 4*: In this chapter, Density Functional Theory (DFT) has been employed to study the interactions between Urea with pristine and transition metal (TM) doped two-dimensional graphene structures. Four TM-dopants, namely, V, Ti, Fe, and Cr, are considered.
- *Chapter 5*: This chapter utilises Density Functional Theory (DFT) to showcase the interaction and adsorption of the three most polluting Chlorofluorocarbons (CFC) molecules namely $CFCl_3$, $CClF_3$, and CCl_2F_2 with pristine and Ti-doped two-dimensional graphene sheet.

- *Chapter 6*: In this chapter, the synthesis and functionalization procedure of graphene is thoroughly discussed, followed by their characterization. Also, the fabrication process of chem-resistor and FET based devices is described in detail. Further, the sensing of Glutathione is demonstrated using antibody immobilized over amine-functionalized graphene as a sensing layer in chem-resistive devices.

- *Chapter 7*: In this chapter, the electrochemical sensing of Lactate is demonstrated using enzyme functionalized Polyaniline as a sensing layer. The sensing action was demonstrated using cyclic voltammetry, and sensing parameters were estimated.

- *Chapter 8*: This chapter presents the conclusive remarks on the work presented in previous chapters. The objectives of the thesis have been assessed, the findings and contribution of each chapter have been highlighted. Further, the future aspects for extending the current objectives have been discussed in this chapter.

2

Adsorption of Gaseous Air Pollutants Over Ti-doped ZGNR Structures: A DFT study

Contents

Outline In this study, we employed the Density Functional Theory (DFT) to study the interactions between gaseous air pollutants, including di-atomic (CO and NO), tri-atomic (CO_2 and HCN), and poly-atomic (HCHO and $COCl_2$) species, and Ti-doped zigzag graphene nanoribbon (ZGNR) structures. During this, two types of doped structures are considered, i.e. SV-ZGNR in which Ti replaces one carbon atom and DV-ZGNR, in which Ti atom replaces two adjacent carbon atoms. All gases under consideration observed to exhibit significant adsorption energy over doped ZGNR except $COCl_2$ for which a catalytic dissociation is observed. Our results indicate that doped ZGNR is better for CO, NO, and HCHO adsorption as compared to doped graphene sheet. Also, DV-ZGNR is preferred over SV-ZGNR in terms of adsorption. Moreover, due to the adsorption, changes in the density of states are observed which confirms that the Ti-doped ZGNR has potential to be used as the sensing platform for these gases.

2.1 Introduction

The detection of biologically and environmentally harmful gases has long been a priority in scientific research. The application of nano-engineered materials in gas sensing has been explored as a possible alternative to traditional sensors. Nanostructures such as nanotubes, nanoribbons, and nanowires have been demonstrated to have advantages due to their greater adsorption capability arising out of a high surface area to volume ratio, and due to their configurability as field effect transistors to develop complete gas sensing circuits without external configuration [96]. The discovery of Carbon Nanotubes in 1991 paved the way for research into the next generation of high-speed electronic devices [97]. In recent years, Carbon Nanotubes have been considered for highly sensitive gas sensing applications due to their unique geometry, morphology and material properties [98]. Similar to carbon nanotubes, Graphene is also an allotrope of Carbon with a two-dimensional nature in which the arrangement of atoms is in a hexagonal lattice, as discovered by Novoselov in 2007 [99, 100]. It possesses remarkable electronic and mechanical properties, such as high electronic and thermal conductivities as well as superior mechanical strength, which make it ideal for diverse applications including chemical and biological sensing, high-speed analog electronics and fuel cells [101, 102]. Moreover, the two-dimensional geometry makes it more suitable for FET-based device fabrication. However, Graphene-based nanostructures further exhibit several properties which an extended 2-D graphene sheet does not possess, for eg. Graphene sheets have zero band gap, and hence they do not exhibit semiconducting behav-

ior [103]. However, it is possible to introduce some band gap and observe semiconducting nature by using graphene nanoribbons instead [104]. Also, the zigzag graphene nanoribbons (ZGNR) exhibit the presence of confined electronic states, and surface states strongly localized near the edges, hence they exhibit good spin-polarized behavior at the edges and are often considered for application in spintronics [105, 106].

The Graphene-based nanostructures such as ZGNRs are very often doped chemically to tailor its properties in a more controlled manner [107]. Doping can help to selectively tailor the properties of the nanoribbon as per our requirement [108]. Few common types of doping such as N, B, and Al are studied for the electronic device and sensing related applications [109, 110]. Apart from these, other types of doping such as transition metal doping have also been explored in recent years for applications in gas adsorption and spintronics [111]. It has been observed that doping a Graphene sheet with Titanium improves its interaction with gas molecules for eg. significant adsorption of H_2 on Ti- doped graphene was reported [112]. In addition to this researchers also studied the adsorption ofNO_2, NO, and O_2 on Ti-doped and N-doped 2-D graphene sheet [107]. They also studied the adsorption of formaldehyde and other gases on pure, Ti-doped and N-doped graphene sheets [112]. However, recent studies focussing on Ti-doped ZGNR structures have reported an improvement in the adsorption of Sulfur containing gases, i.e. SO_2 and H_2S [113] as compared to 2-D graphene sheets. All the above studies are based on Density functional theory (DFT) which is a highly accurate quantum chemistry approach for electronic structure calculations. Greenhouse gases such as carbon dioxide and nitrogen dioxide have received significant interest for the design and modeling of sensors and actuators. However, there is a growing demand for the development of devices with higher sensitivity and higher speeds for sensing the presence of gases. Following the development of the first solid state gas sensing device by Seiyama, there have been multiple attempts to make more sensitive sensors. Recent improvements in graphene deposition methods have led to the increased applicability of graphene in the development of gas sensing devices [114]. In the present study, our aim is to study the interaction of harmful gases CO, NO, CO_2, HCHO, HCN and with Ti doped ZGNR using DFT-based calculations. This doping can be done in two ways, first with single carbon vacancy (SV-ZGNR), in which Ti replaces one carbon atom of the ZGNR; and the other one with dual or double carbon vacancy (DV-ZGNR), with Ti replacing two adjacent Carbon atoms. Hence, we have included both types of doped structure in our study. To the best of our knowledge, the adsorption of these gases on Ti-doped ZGNR structures has

not been reported in the literature. We have studied the adsorption of these gases on our substrate by introducing the gases on the substrate in multiple configurations and analysed the changes in the measurable electrical properties before and after the adsorption of the gases. Our results suggest that Ti-doped ZGNR structures can be a viable alternative to graphene sheets as a sensor for these gases.

2.2 Computational Methods

We performed the Density Functional Theory (DFT) calculations using the SIESTA package [115, 116]. The electron-electron interaction energies are estimated within Generalized Gradient Approximation (GGA) with Perdew, Burke, and Ernzerhof (PBE) as exchange and correlation functional [117]. The Troullier-Martins pseudopotential is used to calculate interaction energies between ions and electrons [118]. Atomic orbitals are realized with Double Zeta basis plus the polarization orbital (DZP) basis set. The k-point grid is taken as 1X1X45 for each case. The mesh cutoff for the diatomic case is 370 Rydberg but for the polyatomic case, it is 360 Rydberg. Before performing the energy and atomic structure calculations, the structures were relaxed using the Conjugate Gradients(CG) Algorithm. The force tolerance was taken as less than 0.001 eV/Ang for the diatomic gases, but in order to reduce the computational costs, it was taken as 0.01 eV/Ang for the polyatomic gases. In the study, a 50 and 49 atoms unit cell (4-ZGNR type) are employed for SV-ZGNR and DV-ZGNR as shown in Fig.1 and Fig.2 respectively. The unit cell is periodic in the Z-direction; a vacuum region of more than 15 Åis kept in the rest two directions to avoid any interactions from neighbouring cells.

2.3 Results and Discussion

The structure of the single vacancy (SV) and dual vacancy (DV) graphene nanoribbons are obtained by first replacing the Carbon atoms with the Titanium atom. In the case of SV-ZGNR, one Carbon atom was replaced by the Titanium atom, while for DV-ZGNR, two adjacent Carbon atoms were replaced. These structures are then relaxed using the CG optimization method to obtain the final relaxed structure as shown in Fig.2.1 and Fig.2.2 respectively and the bond lengths are summarized in Table-2.1 for each case. From the table, it can be seen that the average C-C bond length for Carbon atoms neighboring the Ti atom in both the cases remained almost the same as for an undoped graphene sheet i.e. 1.42 Å, with the C-C bond length in SV ZGNR being 1.422 Å, and that in DV ZGNR being 1.421 Å.

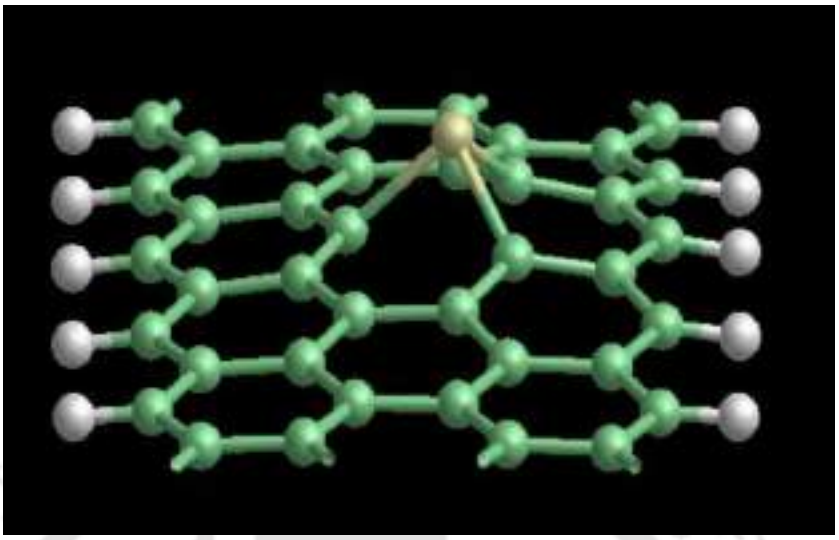

Figure 2.1: Schematic diagram of SV-ZGNR with C, H and Ti atom represented by green, white and yellow colour balls respectively.

However, there was a significant variation observed in the distance between the Titanium and Carbon atoms in both configurations, with the distance between Ti and C being 1.931 Åin the SV case and 2.067 Åin the DV case. Further analysis is done by comparing the Density of States plot before and after the adsorption of the gas. The plots are done after shifting the Fermi energy to 0eV, which helps better analyze the changes in the nature of the Density of States plot.

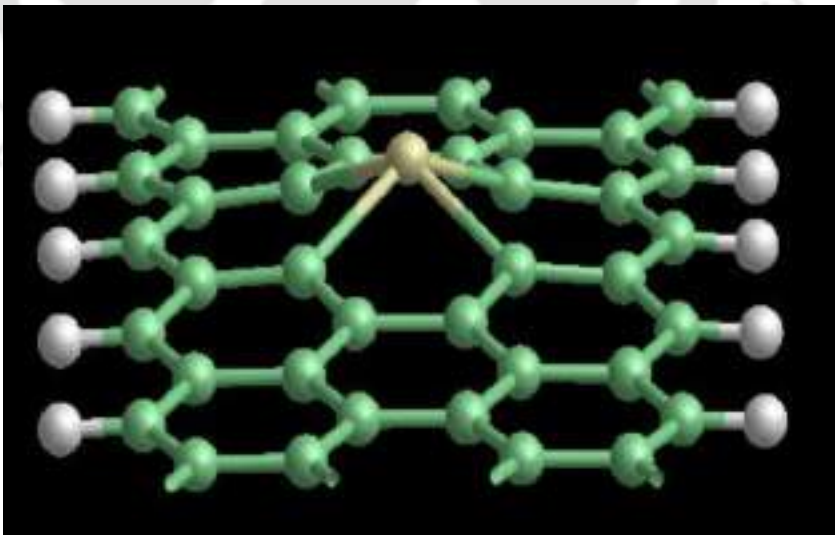

Figure 2.2: Schematic diagram of DV-ZGNR with C, H and Ti atom represented by green, white and yellow colour balls respectively.

However, the Partial Density of States is plotted with the absolute energy values, without shifting the Fermi Energy level to zero. For reference, the Fermi energy levels and the corresponding shifts

in the Fermi energy are documented in Table 2.1. Another important parameter used to judge the interaction between the gas molecule and the doped ZGNR is the adsorption energy (Eads). The Eads for the adsorption of gaseous species over the SV-ZGNR/DV-ZGNR is calculated using Eqn-2.1 and values tabulated in Table-2.3.

$$E_{ads} = E_{SVorDV-ZGNR+Gas} - (E_{SVorDV-ZGNR} + E_{Gas}) \tag{2.1}$$

Where, the $E_{SVorDV-ZGNR+Gas}$, $E_{SVorDV-ZGNR}$ and E_{Gas} is the energy of combined system, energy of layer and energy of the isolated gas molecule.

Table 2.1: The calculated bond length of configurations of doped ZGNR and gas molecules over them.

Bond	**Configurations of doped ZGNR and Gas-doped ZGNR**					
	SV-ZGNR	**SV-ZGNR with CO**	**SV-ZGNR with NO**	**DV-ZGNR**	**DV-ZGNR with CO**	**DV-ZGNR with NO**
C-C (Å)	1.422	1.409	1.459	1.421	1.435	1.419
C-H (Å)	1.101	1.101	1.101	1.101	1.101	1.101
C-Ti (Å)	1.931	1.963	1.985	2.067	2.119	2.122
Ti-Gas (Å)	-	Ti-O: 2.156 Ti-C: 2.326	Ti-O: 2.066 Ti-N: 2.055	-	Ti-O: 2.006 Ti-C: 2.305	Ti-N: 1.988 Ti-O: 2.092

Table 2.2: Analysis of Fermi energy levels

System	**Fermi Level**	**Fermi Level Shift**	**System**	**Fermi Level**	**Fermi Level Shift**
DV-ZGNR	-3.2569 eV	-	SV-ZGNR	-3.1776 eV	-
CO Adsorption	-3.3836 eV	-0.1267 eV	CO Adsorption	-3.3671 eV	-0.1895 eV
NO Adsorption	-3.5165 eV	-0.2596 eV	NO Adsorption	-3.4885 eV	-0.3109 eV
CO_2 Adsorption	-3.6762 eV	-0.4193 eV	CO_2 Adsorption	-3.4528 eV	-0.2752 eV
HCHO Adsorption	-3.2747 eV	-0.0178 eV	HCHO Adsorption	-3.2259 eV	-0.0483 eV
HCN Adsorption	-3.0613 eV	0.1956 eV	HCN Adsorption	-3.0043 eV	0.1733 eV

Table 2.3: Calculated adsorption energies of gases over doped ZGNR structures.

Adsorption Energy of Gas	Doped Structure	
	SV-ZGNR	**DV-ZGNR**
CO	-1.30 eV	-1.96 eV
NO	-2.86 eV	-3.13 eV
CO_2	-0.89 eV	-2.26 eV
HCN	1.86 eV	2.91 eV
HCHO	-2.11 eV	2.34 eV
$COCl_2$	-	-1.98 eV

2.3.1 NO Adsorption

In order to study the gas adsorption over doped ZGNR structures, the gas molecule is relaxed over the doped ZGNR structure until the force per atom is less than 0.001 eV/Ang. The relaxed structures are shown in Fig.2.3 and Fig.2.4. Again the values from Table-2.1 reflects that in both the cases, the distance between the Ti atom and the O atom, and the Ti atom and the N atom is found to be nearly identical. This indicates that the Ti atom interacts with both the N and O atom of the NO gas. In the case of SV ZGNR, we observed an increase in the C-C bond lengths of the Carbon atoms nearest to the Ti atom from 1.422 Åto 1.459 Å, as well as an increase in the Ti-C bond length to 1.985 Å. These changes can be seen because the Ti and C atoms move further out of the plane of the ZGNR in the presence of NO. The changes in bond lengths for DV ZGNR are far less pronounced, as can be seen from the Table-2.1.

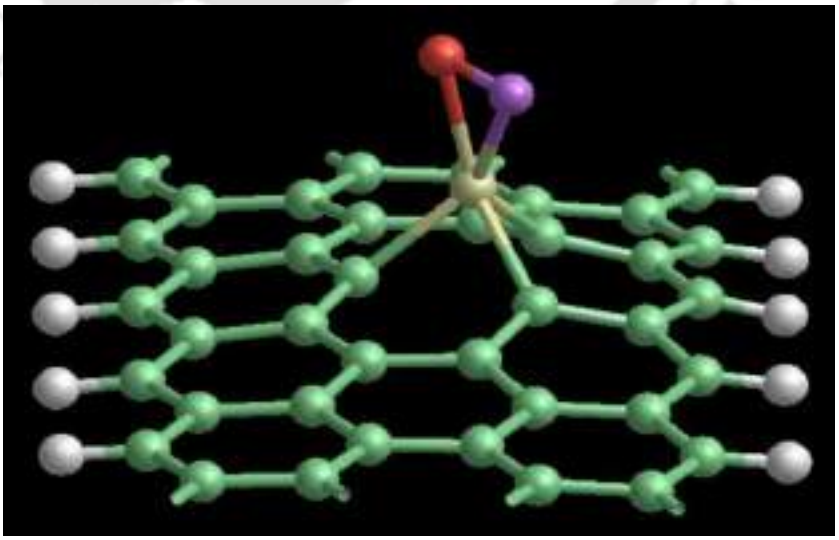

Figure 2.3: Schematic diagram of NO molecule adsorption over SV-ZGNR with C, H, O, N and Ti atom represented by green, white, red, purple and yellow colour balls respectively.

Now, from the Table-2.3, it can be observed that NO molecule has higher adsorption energy over DV-ZGNR than SV-ZGNR, which is -2.86eV and -3.13eV respectively. Also, the adsorption energy values for both SV and DV-ZGNR are significantly higher than reported values for Ti-doped 2D graphene sheet [112]. This shows that adsorption is preferred over Ti-doped DV-ZGNR as compared to SV-ZGNR which is still better than graphene sheet.

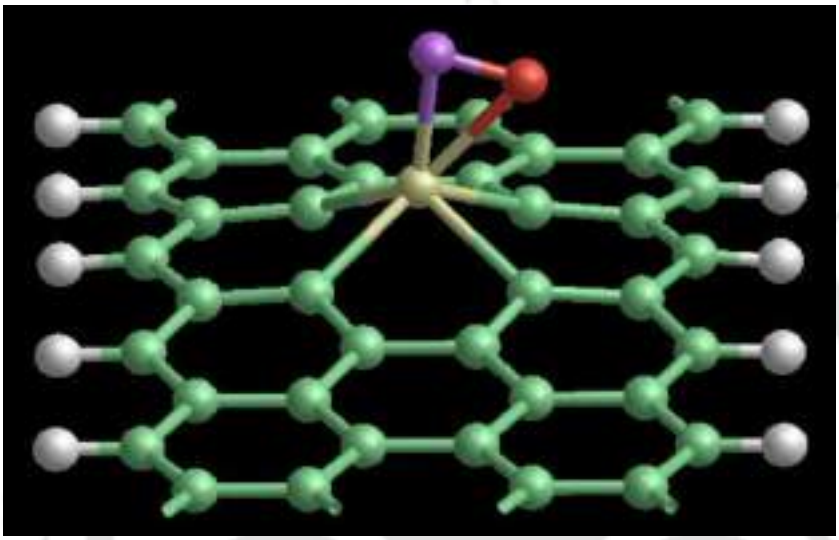

Figure 2.4: Schematic diagram of NO molecule adsorption over DV-ZGNR with C, H, O, N and Ti atom represented by green, white, red, purple and yellow colour balls respectively.

In order to observe the effect of gas adsorption on the electronic structure of ribbon, the density of states (DOS) plotted for the range of -10eV to 10eV as shown in Fig.2.5 and Fig.2.6.

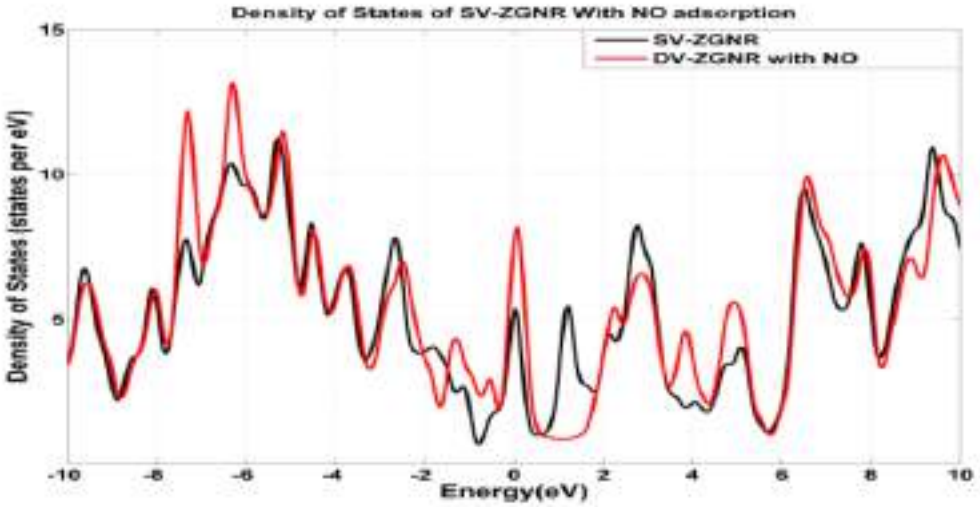

Figure 2.5: Figure representing change in the density of states of SV-ZGNR after NO adsorption.

Due to the interaction of ribbon with the gas molecule, a shift was observed in the DOS. Due to this shift, one can expect the electron density of ribbon to change, which will ultimately be reflected as a change in the current during two probe measurement. There are significant shifts seen in the DOS plots around the Fermi energy level. These changes indicate a change in the I-V characteristics of the substrate after adsorption with NO. Further changes are also observed further away from the Fermi energy level, which however is expected to contribute less to the electron transportation.

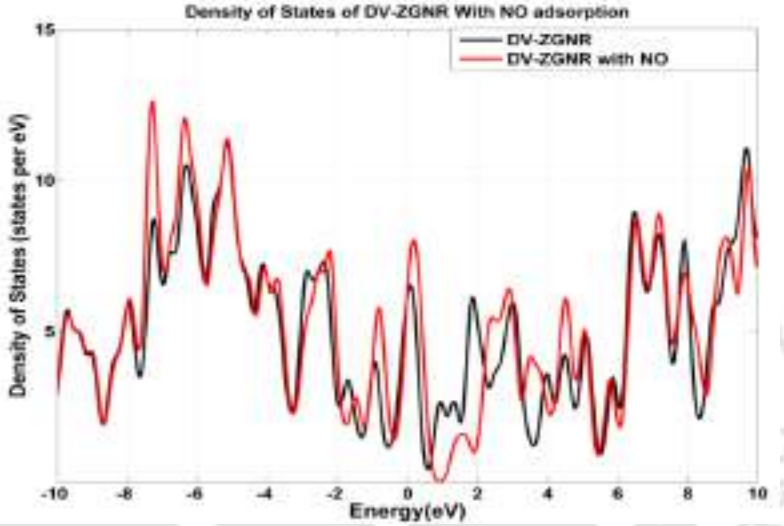

Figure 2.6: Figure representing change in the density of states of DV-ZGNR after NO adsorption.

Further, the partial density of states (PDOS) as shown in Fig. 2.7, is analyzed carefully to observe the interaction between the orbitals of Ti and the atoms of the gas molecule.

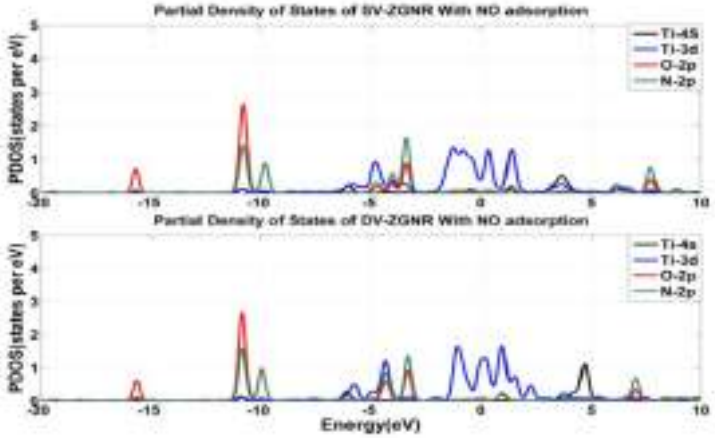

Figure 2.7: Figure representing the PDOS of orbitals of Ti, N, and O atom.

In both the cases of SV and DV-ZGNR, we can observe from the PDOS plot that the 3d orbital

of Ti, 2p orbital of N and 2p orbital of O overlap in the region between -5eV and 0eV. Further, an overlap is also observed near -10eV. This confirms the interaction between the Ti atom and the atoms of the gas molecule.

2.3.2 CO Adsorption

The interactions between CO and Ti-doped ZGNR can be seen in Fig.2.8 and 2.9.

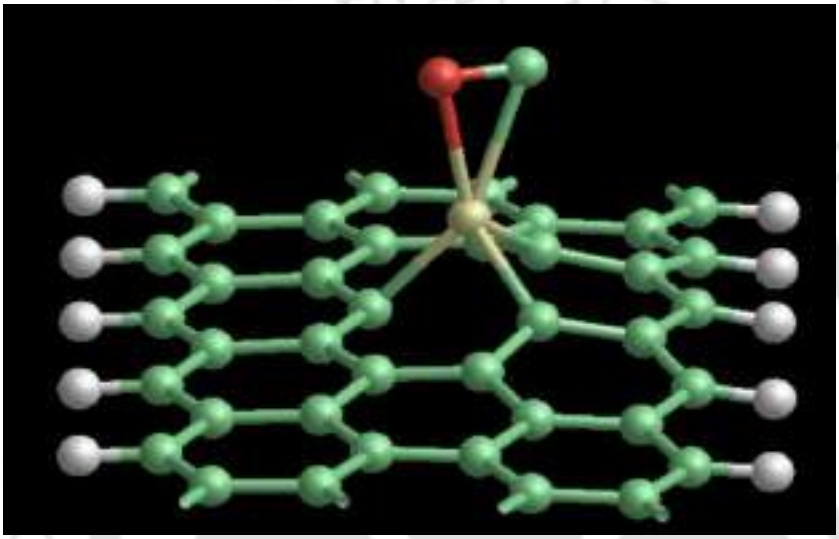

Figure 2.8: Schematic diagram of CO molecule adsorption over SV-ZGNR with C, H, O and Ti atom represented by green, white, red and yellow colour balls respectively

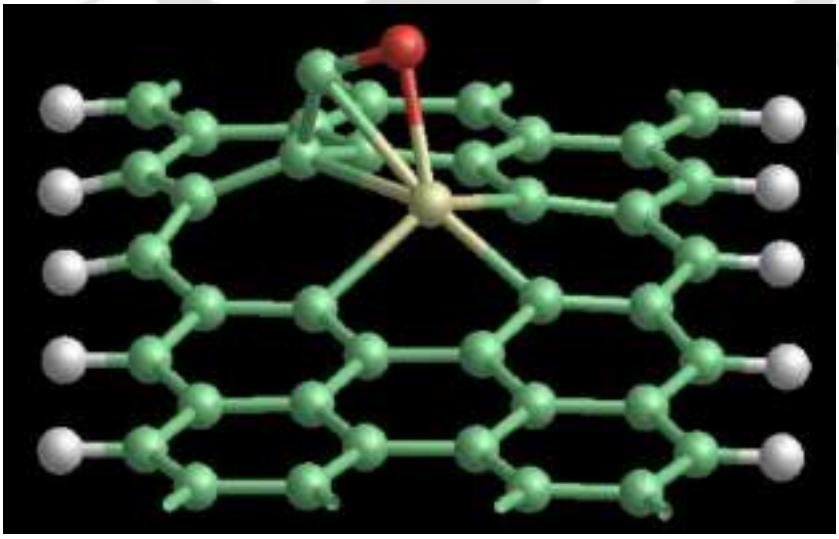

Figure 2.9: Schematic diagram of CO molecule adsorption over DV-ZGNR with C, H, O and Ti atom represented by green, white, red and yellow colour balls respectively

After the adsorption, the O atom is found to be closer to the Ti atom for both the cases, indicating

a stronger interaction these two atoms rather than the Ti atom and the C atom of the gas. However, interestingly, the interaction of the CO gas molecule with the DVZGNR is strikingly different. The C atom of the gas molecule bends slightly towards the nanoribbon and causes a distortion in the structure of the nanoribbon itself. The C atom nearest the C atom of CO gas is raised slightly and interacts with it. After the adsorption, the O atom is found to be closer to the Ti atom for both the cases, indicating a stronger interaction these two atoms rather than the Ti atom and the C atom of the gas. However, interestingly, the interaction of the CO gas molecule with the DV-ZGNR is strikingly different. The C atom of the gas molecule bends slightly towards the nanoribbon and causes a distortion in the structure of the nanoribbon itself. The C atom nearest the C atom of CO gas is raised slightly and interacts with it. Again from the Table-2.3, it can be concluded that adsorption of CO molecule is preferred over DV-ZGNR than SV-ZGNR. Here also, the adsorption energy values for both SV and DV-ZGNR are significantly higher as compared to the reported values for Ti-doped 2D graphene sheet [112]. The Density of States plots were used to study the interaction between the CO and the doped ZGNR (Fig.2.10 and 2.11).

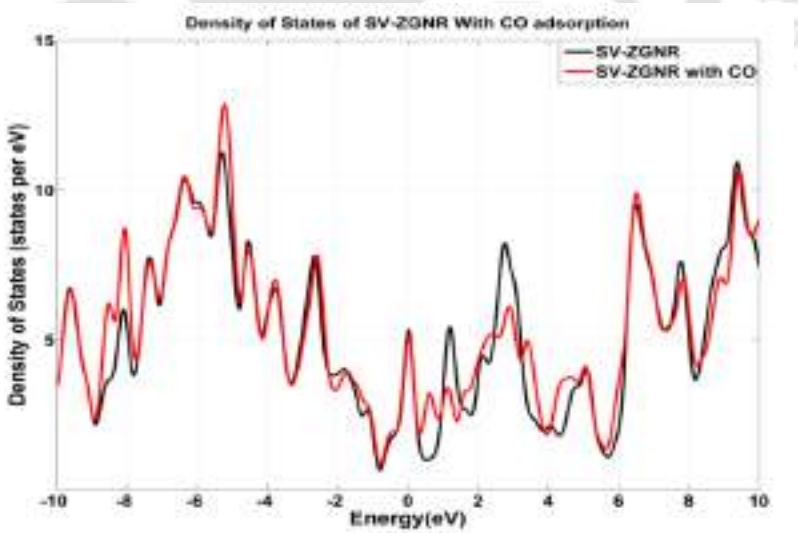

Figure 2.10: Figure representing change in the density of states of SV-ZGNR after CO adsorption.

There are smaller changes observed in the Density of States plot for the two cases, around the Fermi energy level, as compared to the adsorption of NO. These changes are again likely to reflect in the I-V characteristics of the system.

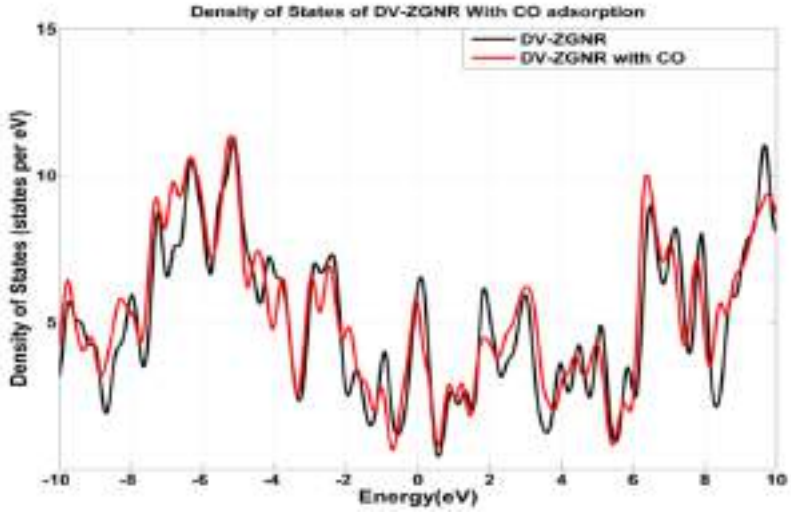

Figure 2.11: Figure representing change in the density of states of DV-ZGNR after CO adsorption.

From the PDOS plot shown in Fig.2.12, we can observe the overlap between the 3d and 2p orbitals of Titanium and Oxygen respectively, especially in the region between -5eV and 0eV.

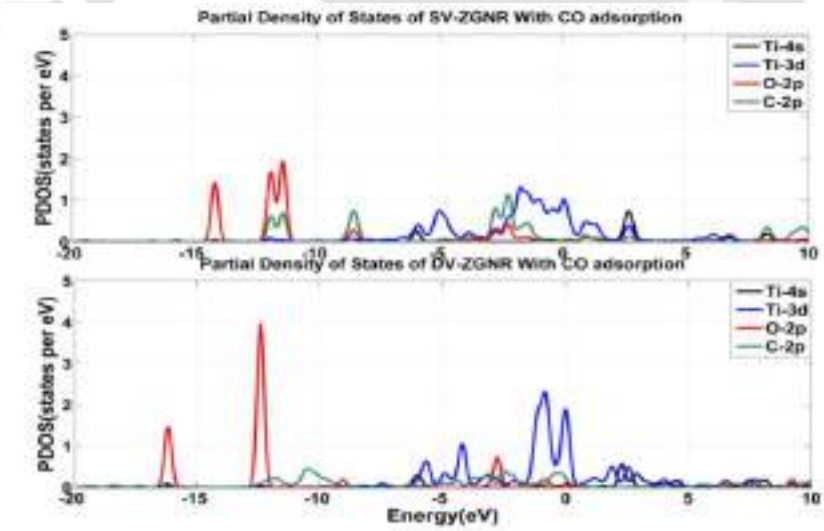

Figure 2.12: Figure representing the PDOS of orbitals of Ti, C, and O atom

In the case of SV-ZGNR, there is an overlap observed between the 2p orbital of C atom and the 3d atom of Ti atom, whereas this overlap is almost negligible in the case of DV-ZGNR.

2.3.3 CO_2 Adsorption

The interactions between CO_2 and doped ZGNR vary in the case of SV-ZGNR and DV-ZGNR (Fig.2.12 and 2.1313). After the adsorption, the O atom is found to be closer to the Ti atom for both

the cases, indicating a stronger interaction these two atoms rather than the Ti atom and the C atom of the gas.

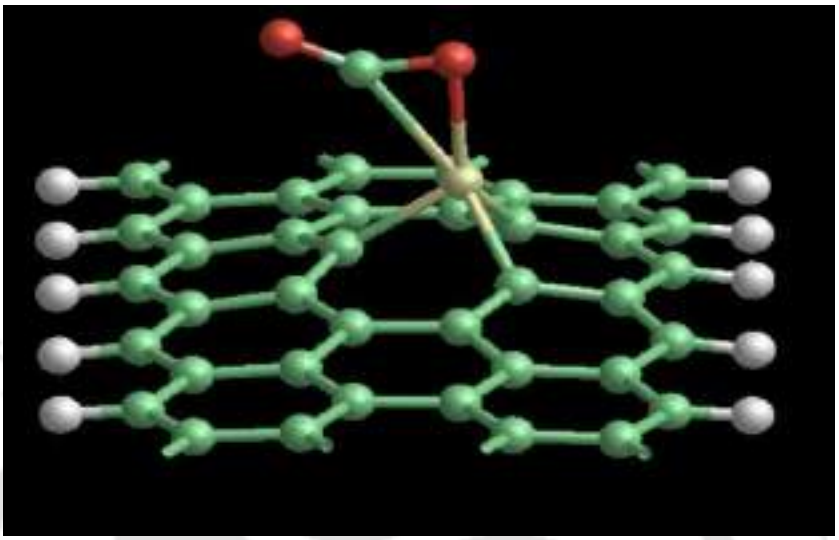

Figure 2.13: Schematic diagram of CO_2 molecule adsorption over SV-ZGNR with C, H, O and Ti atom represented by green, white, red and yellow colour balls respectively.

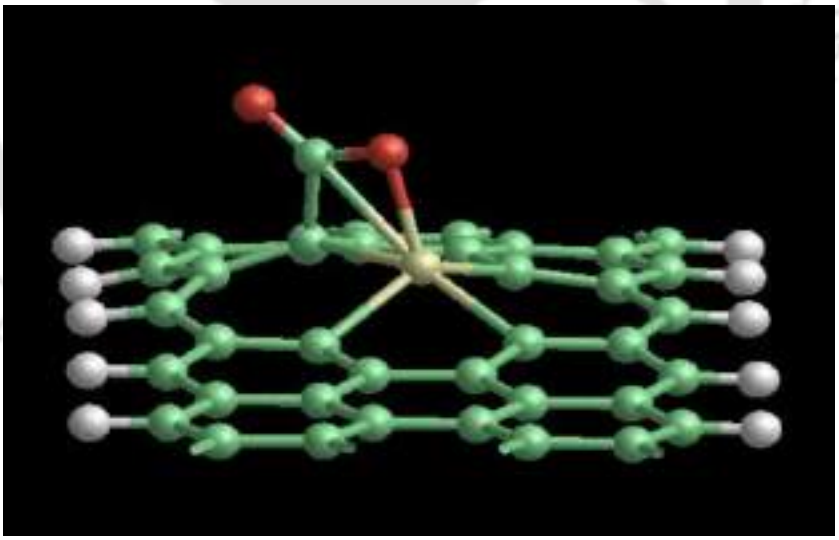

Figure 2.14: Schematic diagram of CO_2 molecule adsorption over DV-ZGNR with C, H, O and Ti atom represented by green, white, red and yellow colour balls respectively

The interaction of the CO_2 gas molecule with the DV-ZGNR is strikingly similar to that of Carbon Monoxide. The C atom of the gas molecule bends slightly towards the nanoribbon and again causes a distortion in the structure of the nanoribbon. The C atom of the nanoribbon nearest the C atom of CO_2 gas is raised slightly and interacts with it. Again, from Table-2.3, it can be concluded that adsorption of CO_2 molecule is preferred over DV-ZGNR as compared to SV-ZGNR, similar to the case

of NO and CO. Inspecting the DOS graph plotted, we observe that for the case of SV-ZGNR, there is a significant shift observed between the DOS plots between 0eV and 5eV as shown in Fig.2.15. Again, a similar shift is observed between -5eV and 0eV for the case of DV-ZGNR as shown in Fig.2.16.

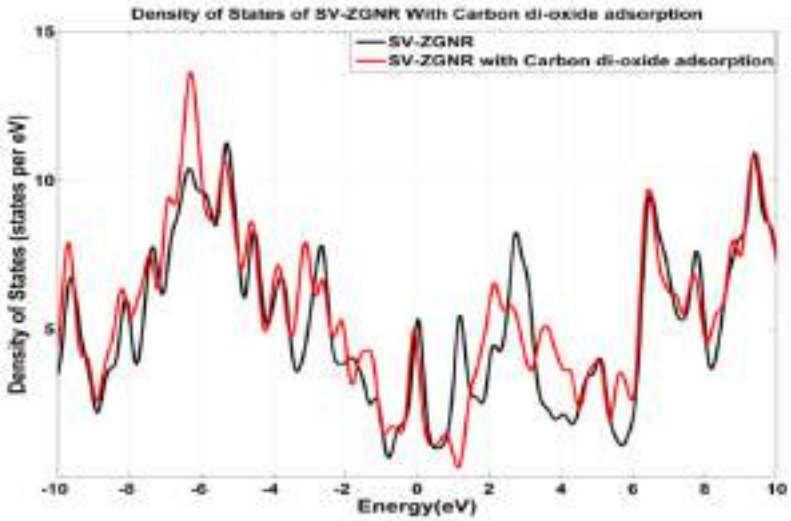

Figure 2.15: Figure representing change in the density of states of SV-ZGNR after CO_2 adsorption.

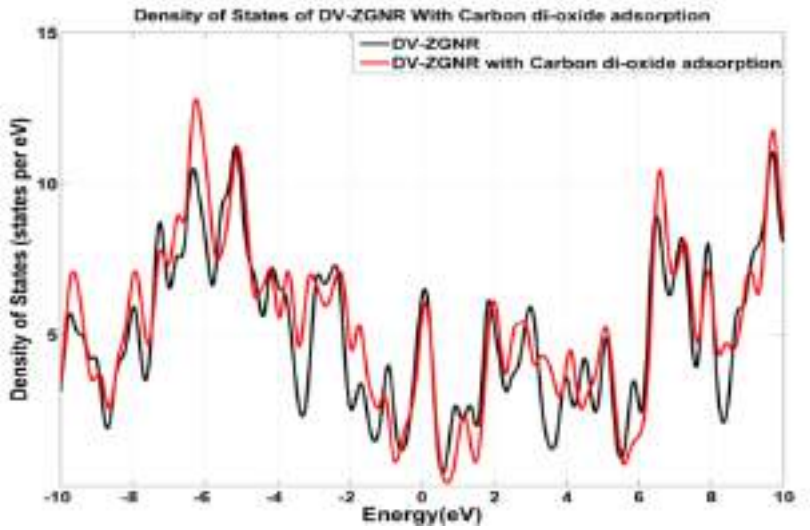

Figure 2.16: Figure representing change in the density of states of DV-ZGNR after CO_2 adsorption.

Again from PDOS plots in shown in Fig.2.17, in both cases, there is significant overlap witnessed between the 3d and 2p orbitals of Titanium and Oxygen atom respectively, in the region between -5eV to 0eV. For the same energy range, an overlap is observed between the Ti orbitals and the 2p-orbital of C atom of the gas in the case of SV-ZGNR, but it is almost negligible for DV-ZGNR hence it can be concluded that Ti-3d and O-2p are the major cause of the interactions in the second case.

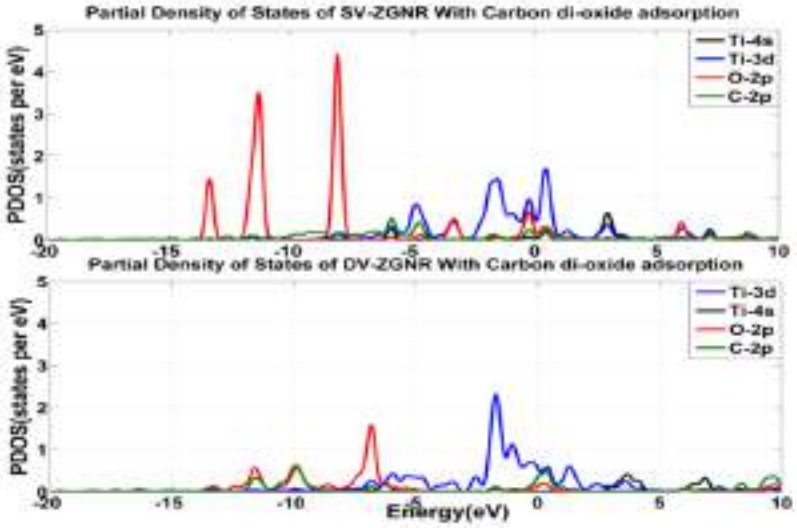

Figure 2.17: Figure representing the PDOS of orbitals of Ti, C, and O atom.

2.3.4 HCN Adsorption

The interactions between HCN and doped ZGNR are again studied in the case of SV-ZGNR and DV-ZGNR (Fig. 2.18 and 2.19).

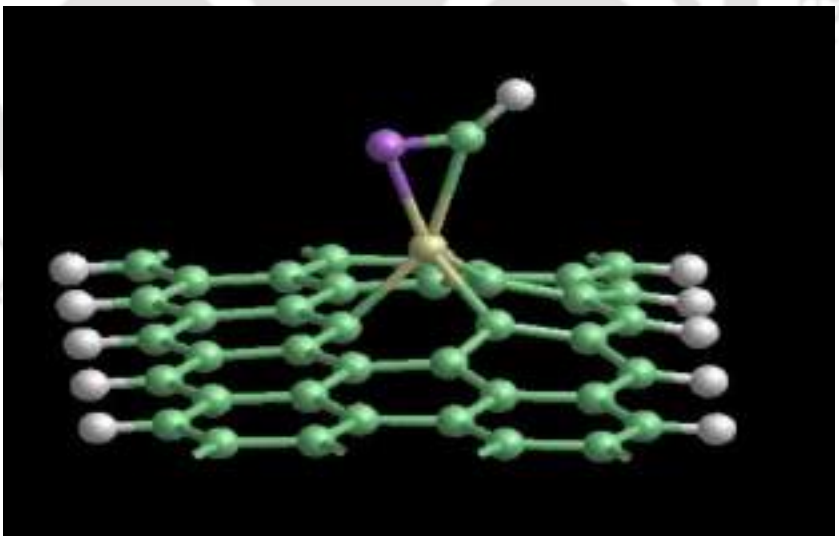

Figure 2.18: Schematic diagram of HCN molecule adsorption over SV-ZGNR with C, H, N and Ti atom represented by green, white, purple and yellow colour balls respectively

The Hydrogen Cyanide molecule is introduced into the system in multiple configurations, with the Carbon atom and Nitrogen atoms respectively closer to the Titanium atom. The interaction of HCN with SV-ZGNR and DV-ZGNR vary significantly, Similar to the case of adsorption of CO and CO_2, in the case of DV-ZGNR, the Carbon atom interacts with the substrate, forming a strong interaction

with the substrate chain. This further causes an increase in the adsorption energy of the gas.

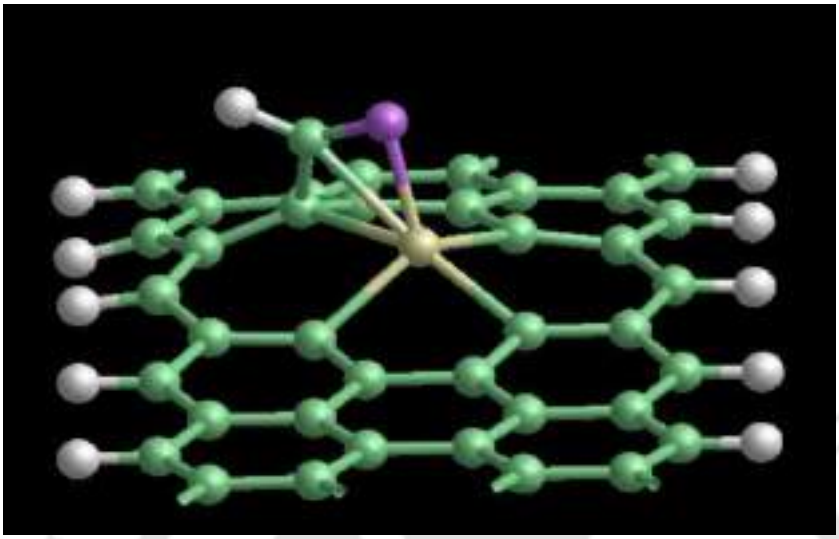

Figure 2.19: Schematic diagram of HCN molecule adsorption over DV-ZGNR with C, H, N and Ti atom represented by green, white, purple and yellow colour balls respectively

The values for the adsorption energy hence calculated indicate once more that the adsorption of HCN is preferred over DV-ZGNR. Proceeding as before, here also the DOS is plotted. For both cases, there is a significant shift observed between the DOS plots close to 0eV as shown in Fig.2.19, especially between 0eV and 5eV, as shown in Fig.2.20 and Fig.2.21.

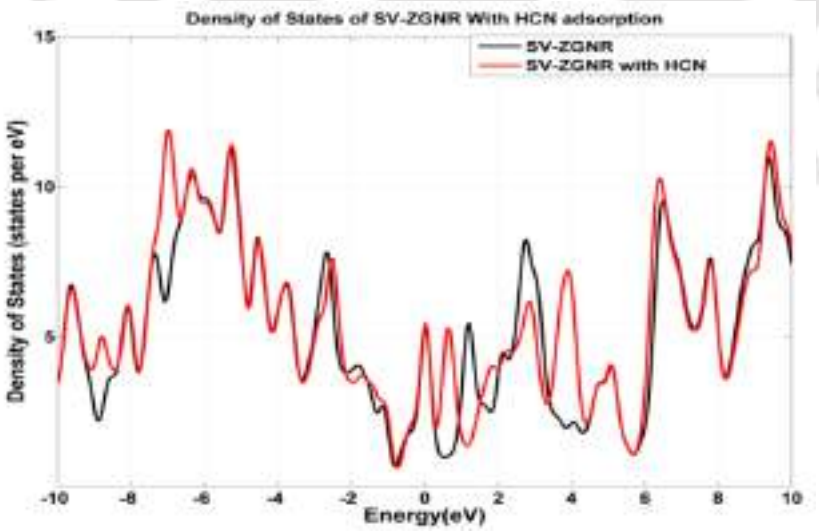

Figure 2.20: Figure representing change in the density of states of SV-ZGNR after HCN adsorption.

Further, HCN has a unique attribute of having a positive shift in the Fermi energy level, as against the negative shift observed in all other cases.

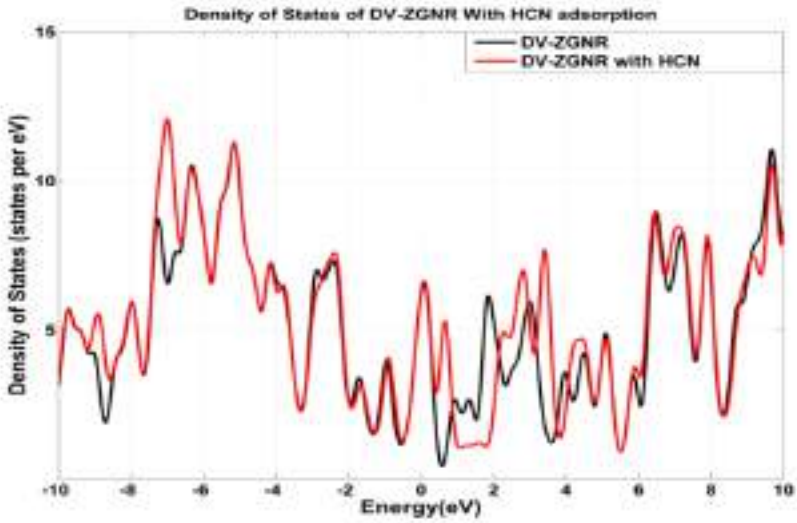

Figure 2.21: Figure representing change in the density of states of DV-ZGNR after HCN adsorption.

Again from PDOS plots in shown in Fig.2.22, in the case of SV-ZGNR, there is significant overlap witnessed between the 3d orbitals of Titanium and the 2p orbitals of Carbon and Nitrogen atoms, in the region between -5eV to 0eV.

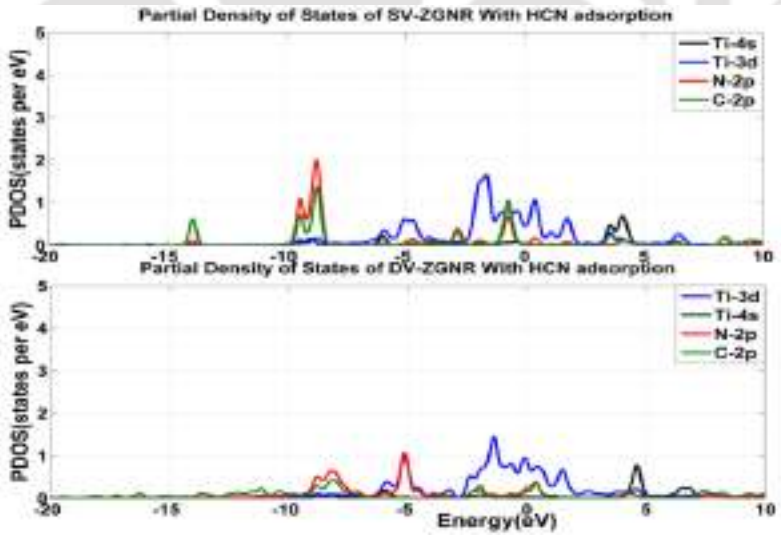

Figure 2.22: Figure representing the PDOS of orbitals of Ti, C, N and O atom.

For the energy range of -5eV to 2eV, an overlap is observed between the Ti 3d orbitals and the 2p-orbital of C atom and N atom of the gas in the case of DV-ZGNR. However, the principle interaction in the second case is due to the interaction of the C atom of the gas with that of the nanoribbon.

2.3.5 HCHO Adsorption

The interactions between HCHO and doped ZGNR vary slightly in the case of SV-ZGNR and DV-ZGNR (Fig. 2.23 and 2.24). Initially, the formaldehyde molecule was introduced with Oxygen atoms, as reported by Zhang et. al. [112] in the interaction of formaldehyde with the graphene sheet. The interaction of HCHO with SV-ZGNR and DV-ZGNR appears similar in terms of the interaction between the gas molecule and the graphene nanoribbon, with only slight variations in the bond lengths of C-Ti and Ti-O. The adsorption energies are calculated from Eqn.2.1 and tabulated in Table-2.3.

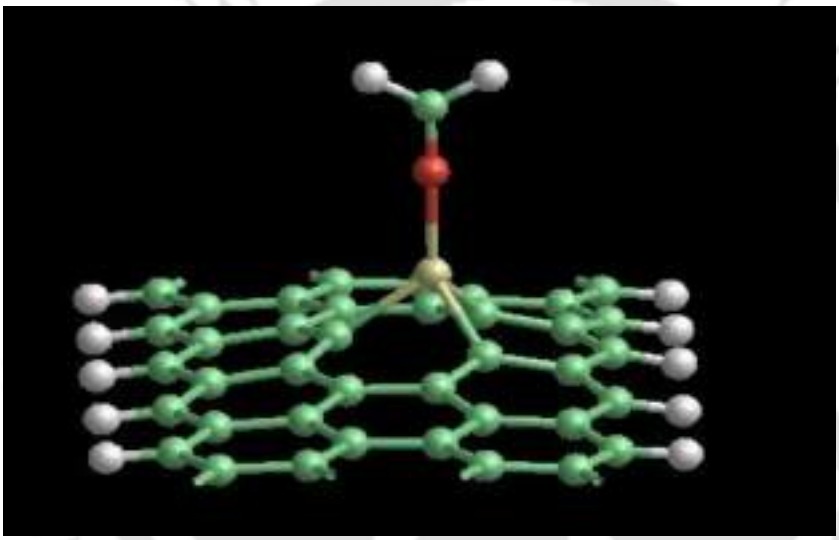

Figure 2.23: Schematic of HCHO molecule adsorption over SV-ZGNR with C, H, O and Ti atom represented by green, white, red and yellow colour balls respectively

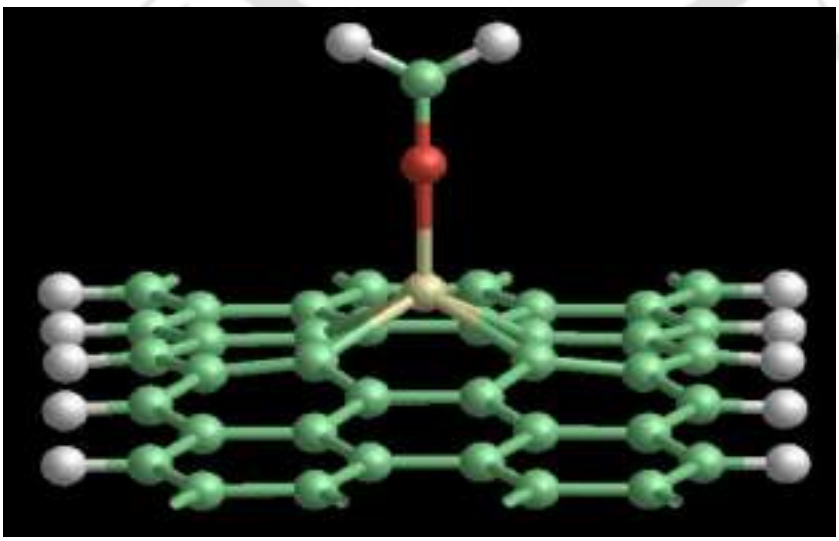

Figure 2.24: Schematic of HCHO molecule adsorption over SV-ZGNR with C, H, O and Ti atom represented by green, white, red and yellow colour balls respectively.

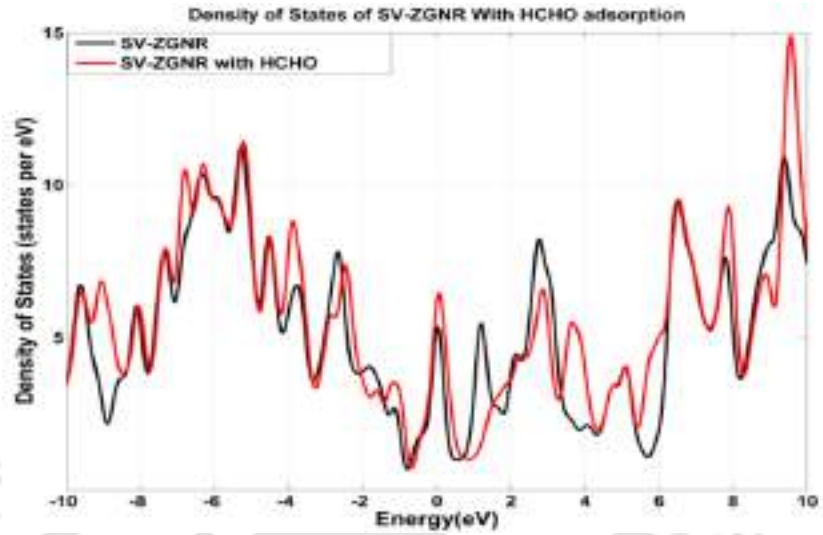

Figure 2.25: Figure representing change in the density of states of SV-ZGNR after HCHO adsorption.

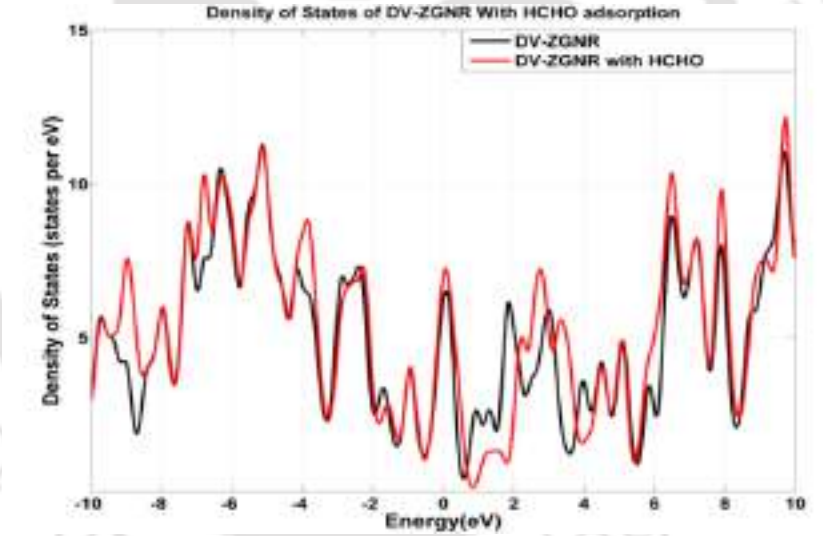

Figure 2.26: Figure representing change in the density of states of DV-ZGNR after HCHO adsorption.

Again from the Table-2.3, it can be concluded that adsorption of HCHO molecule is preferred over DV-ZGNR than SV-ZGNR. Here also, the adsorption energy values for both SV and DV-ZGNR are higher as compared to the reported values for Ti-doped 2D graphene sheet [96].

Similar to the previous gases studied, adsorption is also preferred over Ti-doped DV-ZGNR as compared to SV-ZGNR which is altogether better than doped graphene sheet [96]. Similarly, here also the DOS is plotted.

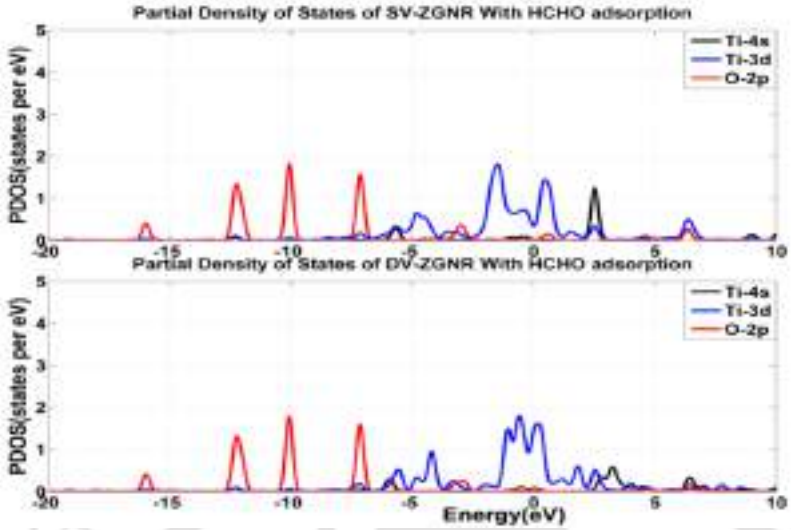

Figure 2.27: Figure representing the PDOS of orbitals of Ti, N and O atoms.

For the case of SV-ZGNR, there is a significant shift observed between the DOS plots between 0eV and, as shown in Fig.2.25. A similar shift is observed between 0eV and 5eV, close to the Fermi energy level for the case of DV-ZGNR as shown in Fig.2.26. Again, from the PDOS plot shown in Fig.2.27, in the case of SV-ZGNR, there is a significant overlap witnessed between the 3s and 2p orbitals of Titanium and Oxygen atoms respectively in the energy ranges -7eV to 0eV and 5eV to 10eV. For the energy range of -5eV to 0eV, an overlap is observed between the Ti orbitals and the 2p-orbital of C atom of the gas in the case of DV-ZGNR. Hence, the interactions are primarily between 3d of Ti and 2p of O atom.

2.3.6 $COCl_2$ Adsorption

The interaction of Phosgene on the Ti-doped ZGNR structure occurs in an interesting manner. Titanium acts as a catalyst for phosgene. Phosgene dissociates into carbon monoxide and chlorine gas. The interaction of SV-ZGNR with phosgene was studied under various configurations, and in all configurations, the catalytic action of Titanium caused Phosgene to split into Chlorine molecule and Carbon Monoxide gas. Similar to the case of SV-ZGNR, the interaction with DV-ZGNR results in dissociation phosgene is introduced with Chlorine atom closer to the Ti atom. However, when phosgene is introduced with Oxygen atom closer to the Titanium atom, a strong interaction occurs between Oxygen atom and Titanium atom, without causing the catalysis of phosgene with the adsorption energy close to 2eV. Moreover, more extensive analysis needed for better understanding of

this phenomenon.

2.4 Summary

The study and analysis of the adsorption of harmful gases on the surface of Ti-doped ZGNR substrates are essential for the formulation of a method to detect these gases. Our study demonstrates that for the adsorption of NO, both SV and DV-ZGNR showed significant adsorption energies of -2.86 eV and -3.13 eV respectively. In the case of CO gas, the adsorption energies are lower at -1.3 eV and -1.96 eV for SV and DV-ZGNR respectively. In the case of Formaldehyde, the adsorption energy observed are almost identical for SV and DV-ZGNR respectively. The adsorption energies for all 3 gases are significantly higher than the values reported for the 2D-graphene sheet. Other than these gases, adsorption of HCN over both types of doped structures are observed with moderate adsorption energies of -1.86 eV and -2.91 eV for SV and DV-ZGNR respectively. The adsorption of CO_2 over the doped structure varies with very small adsorption energy of -0.89 eV for SV-ZGNR to a fairly considerable value of about -2.26 eV for DV-ZGNR. In the end, by looking at the difference between the adsorption energy for SV and DV-ZGNR, one can conclude that for all gases under consideration adsorption is preferred over DV-ZGNR substrate. The case of $COCl_2$ is unique, as catalytic dissociation is observed on interaction with the substrate. Doped ZGNR structures can hence have great future applications as gas-sensing platforms.

3

Adsorption of Phosgene on Titanium doped Graphene Nanoribbons: A DFT Study

Contents

Outline This chapter elaborates the study of the interaction of Phosgene ($COCl_2$) on two configurations of Titanium doped Graphene Nanoribbons (GNR)- Armchair GNR and ZigZag GNR. We analyze the changes in the electronic structure of the substrate before and after the adsorption of Phosgene, with the help of Density Functional Theory (DFT) calculations. The Titanium doping was assumed to be substitutional. The Phosgene gas molecule was introduced in multiple configurations to account for the randomness of the incoming gas molecule on the substrate. Our results indicate that the Titanium atom causes a catalytic splitting of the C-Cl bond, reducing the toxic gas into less harmful by-products. Carbon mono-oxide gas is released after the adsorption, while the Chlorine atoms attach to the substrate. The Oxygen atom in the gas can partially shield the C-Cl bond and form a physical barrier to the splitting. However, this effect was seen only in a small minority of the cases we studied. This study was further extended to two other molecules one with an S-Cl bond ($SOCl_2$ -Thionyl Chloride) and one with an O-Cl bond ($POCl_3$). Our results demonstrate that Ti-doped graphene nanoribbons have great potential to be used as a platform for toxic gas treatment as well as sensing.

3.1 Introduction

$COCl_2$, commonly known as Phosgene, is an industrial intermediate chemical used in the production of isocyanate-based polymers, dyes, pesticides, and pharmaceuticals [119]. It is an extremely toxic gas, and exposure to it can lead to pulmonary edema [120]. It was also used during in various military applications [121]. Phosgene has a mildly pleasant odor and initially only causes slight irritations in the upper respiratory system and skin. This can lead to the victim not seeking a route for escape before severe damage occurs in the lower respiratory system [122]. Further, the research has shown that Phosgene symptoms may not appear immediately after exposure, and typically after a latency period of up to 24 hours, at which point a breakdown occurs in the blood-air barrier, and death usually occurs within 48 hours [123]. Hence, the detection of phosgene in lower concentrations becomes critical.

The development of novel nanomaterials has long been a top priority for application in gas sensing. In 1991, the discovery of carbon nanotubes opened a new era of research on the next generation of high-speed electronic devices [124]. Carbon-based nanostructures such as the carbon nanotubes (CNT), graphene nanoribbons (GNR), and graphene sheets have a high adsorption capability due to their

high surface area to volume ratio. Moreover, owing to their 2D structure, they can be integrated with current field-effect transistor (FET) fabrication techniques, and we can consequently develop a complete gas sensing circuit without the need for any external circuitry [125]. Carbon Nanotubes have subsequently been considered for gas sensing applications due to their unique structure and properties. Graphene, like CNT, is also an allotrope of carbon. It has a two-dimensional arrangement of atoms in a hexagonal lattice, as reported by Novoselov in 2007 [126, 127]. Its outstanding properties, such as high electronic and thermal conductivities, as well as its exceptional mechanical strength, make it an ideal candidate for various sensing applications [128, 129]. Further, its two-dimensional geometry facilitates FET-based device fabrication.

Despite these advantages, pristine graphene has found limited applications as a gas sensor, primarily due to its limited chemical interaction capability with most gas molecules. Most gases react with graphene via physisorption, producing little to no change in the electrical properties of graphene. These properties of GNR can be tailored with the help of doping [130]. Theoretical and experimental studies have shown that doping graphene with transition metals such as Titanium enhances the adsorption of gas molecules [131]. Further, studies have also shown that doped graphene structures can be experimentally synthesized with good thermal stabilities [132, 133]. The strong interaction between the transition metal and gas molecule greatly aids the molecular adsorption. Further, it was observed that the Titanium doped graphene sheet exhibits good adsorption of H_2 [134]. The adsorption of NO_2, NO, and O_2 on Titanium and Nitrogen- doped graphene sheet has also been reported previously [135].

In the present study, our aim is to observe and analyze the interaction of Phosgene with Ti-doped carbon nanostructures- Zigzag GNR and Armchair GNR, with the help of DFT calculations. In this study, we have considered two types of Ti doping. In the first type, the Ti atom replaces one carbon atom from the GNR substrate. We denote this as the Single Vacancy Doping or SV-ZGNR. The second type is when the Ti atom replaces two adjacent Carbon atoms from the GNR substrate. We denote this as the Dual Vacancy Doping or DV-ZGNR. Zhang et. al. reported the interaction of phosgene with transition metal-doped Graphene sheets but the interaction (and splitting) of the same with two different types of Ti-doping over ZGNR and AGNR was not covered [136]. Hence, our aim is to study the adsorption of these gases on the GNR by introducing the gas molecule in various unique arrangements and analyzed the difference in the electronic properties of GNR before and after the adsorption of the gases. Our results demonstrate that Titanium possesses a strong catalytic

tendency towards the Oxygen-Chlorine bond. To further verify our results, we have performed the same simulations for other compounds which have a similar Oxygen-Chlorine bond, and the results indicate a promising trend in the catalytic activity of the gas.

3.2 Computational Details and Input Parameters

We performed the first-principles Density Functional Theory calculations using the SIESTA package [137, 138]. The electron exchange-correlation energies are estimated with Perdew, Burke, and Ernzerhof (PBE) exchange functionals within the generalized gradient approximation (GGA) [139]. The Troullier-Martins Pseudopotential is used to calculate interaction energies between ions and electrons [140]. Atomic orbitals are realized with the double zeta basis plus the polarization orbital (DZP) basis set. The k-point grid is taken as 7x7x1 for each case. The mesh cut off is taken as 350 Rydberg. Before performing the energy calculations and atomic structure calculation, the structures were relaxed using conjugate gradients (CG) algorithm. The force tolerance was taken as less than 0.01 eV/Ang. The unit cell is periodic in the z-direction; a vacuum region of more than 15 is kept between the layers, to avoid interactions from neighboring cells.The strength of interaction between gases and GNR is analyzed using adsorption energy (E_{ads}). The adsorption energy can be estimated 3.1, which is given here:

$$E_{ads} = E_{SVorDV-ZGNR+GAS} - (E_{SVorDV-ZGNR} + EGas) \tag{3.1}$$

Where,$E_{SVorDV-ZGNR+GAS}$is energy for the gas adsorbed over the substrate,$E_{SVorDV-ZGNR}$is the energy of the substrate andis the energy of the gas molecule. The energy value calculated is then adjusted for the Basis Set Superposition Error (BSSE).

3.3 Results and Discussion

We now study the interaction of phosgene on the graphene substrates. To account for the inherent randomness of the incoming gas molecule, we introduce the gas in multiple configurations. For our analysis, we rely on the adsorption energy, changes in the density of states, charge sharing estimated through Mulliken charge analysis, and finally charge density plots. From the result of the DFT calculations, the structure of the system is analyzed at the end of each stage. The bond lengths of the relaxed structure are measured to analyze the nature of the bonds formed after adsorption. First, we will discuss the interaction of the gas molecule on the SV and DV-ZGNR substrates. Next, we will

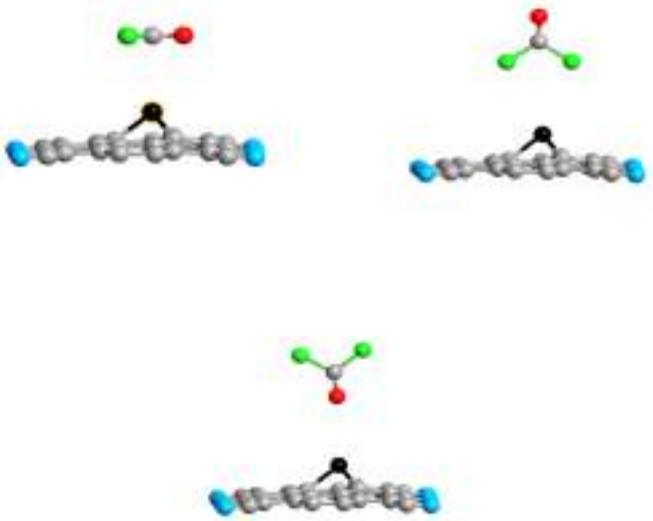

Figure 3.1: The Gas introduced in three independent configurations on the Single Vacancy (SV) ZGNR substrate.

proceed with the same analysis for the AGNR substrate. The analysis is then extended to other gases with similar structures, namely $POCl_3$ (Phosphorous Oxychloride) and $SOCl_2$ (Thionyl Chloride).

3.3.1 Ti-doped SV-ZGNR

The gas is introduced in three configurations, as shown in Fig.3.1. The interaction of the gas on the substrate differs in each case. First, the gas is introduced in the plane of the substrate, with the C atom at a separation of 3 to the Ti atom of the SV-ZGNR substrate, as shown in Fig. 3.1. In Fig 3.1,Hydrogen atom is in blue, Oxygen atom in red, Titanium atom in black, Carbon atom in grey and Chlorine atom in green. The length and width of ribbon is 12.3 and 9.28 respectively. In this case, the gas molecule splits, resulting in the formation of CO gas, while the Cl atoms are absorbed on Ti-atom. The observed Ti-Cl bond length is 2.27, which is slightly greater than the Ti-Cl bond length of 2.17 observed in the TiCl4 molecule. The CO molecule isnt released in the process. Instead, a weak interaction exists with the Titanium atom, which is confirmed by a Ti-C bond length of 2.19, as against the 1.93 reported previously for the interaction of CO with the Ti atom of SV-ZGNR. To better understand the mechanism involved, the individual steps calculated by the DFT process are plotted.

The first step involves the breaking of one C-Cl bond in the gas molecule and the simultaneous formation of a bond between the free Chlorine atom and the Ti atom of the substrate. Next, the second C-Cl bond breaks, and the nascent Cl atom exists in an unstable state. The Cl atom attaches

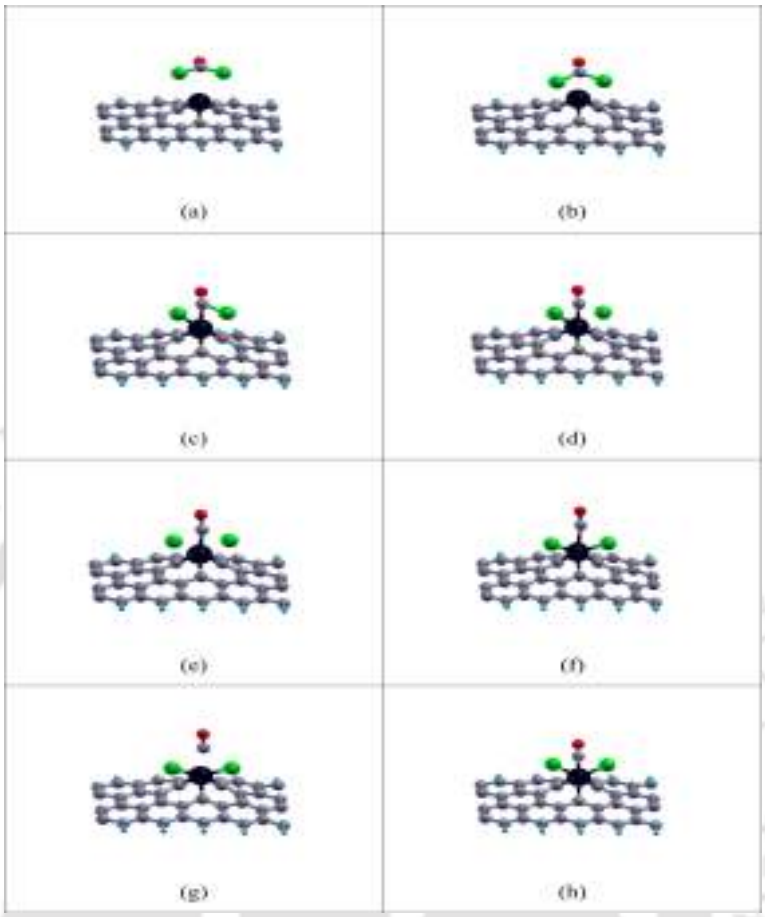

Figure 3.2: Step by step interaction of the gas on the SV-ZGNR substrate, when the gas is introduced with C atom closest to the Ti atom. (a) Initial configuration of the setup. (b) The Chlorine atoms move towards the Ti atom, leading to increased interaction. (c) The first C-Cl bond splits, and the Cl atom simultaneously bonds with the Ti atom. (d) The C atom also bonds with the Ti atom. Anunstable intermediate complex is hence formed. (e) Other C-Cl bond breaks, and the Cl atom is in nascent state. (f) The Ti-Cl bond temporarily breaks, and both Cl atoms exist in a nascent state. (g) The Cl atoms, which are in an unstable state, bond with the Ti atom. (h) CO gas is released temporarily in the configuration, CO atom re-attaches to the Ti atom, forming the final complex.

to the Ti atom, which is followed by the breaking of the C-Ti bond. The CO molecule is, however, unable to escape and re-attaches to the Ti atom. Fig. 3.2 demonstrates the flow of the interaction gas molecule with Ti-doped ZGNR, as described (a-h).

Hydrogen atom is in blue, Oxygen atom in red, Titanium atom in black, Carbon atom in grey and Chlorine atom in green. The length and width of ribbon is 12.3 and 9.28 respectively. The entire process results in the release of 3.778 eV of energy, indicating an energetically favorable reaction.

An important conclusion that can be drawn from this reaction sequence is the affinity of the Cl atom to the Ti atom. The gas, although introduced with the C atom closest to the dopant, sees the migration of the Cl atom towards the substrate. The interaction with the Ti atom causes both the

C-Cl bond to split one-by-one. An unstable intermediate complex is formed. This further splits off, and the final state sees the two Cl atoms bonded to the Ti atom with a charge overlap of 0.421e approximately, indicating the formation of a strong covalent bond. The Ti-C bond formed at the end of the reaction is comparatively weaker with a charge transfer of 0.26e.

Next, we observe and analyze adsorption when the Cl atom is closest to the Ti-atom in the initial configuration. Again, we observe the splitting of the C-Cl bond and the release of the CO molecule. To better understand the reaction mechanism, the DFT steps were studied again. In this case, since the C atom is relatively further away, it never forms a strong interaction with the Ti atom. As a result, the Cl atoms are split off one by one, and CO gas is released in a relatively free state, and can subsequently escape (due to the lower attraction force on the electron cloud of C). The energy released in this process is 2.446 eV, which is less than that in the previous case. This can be explained by the fact that the release of CO molecule from the intermediate complex requires the breaking of the weak interaction between the C-atom of the gas and the Ti atom of the ZGNR, which leads to a reduction in the adsorption energy calculated. Interestingly, the bond lengths and charge sharing in the Ti-Cl bond are almost identical to the previous case.

In the third configuration, an interesting effect is observed. The O atom acts as a shield for the C-Cl bond, preventing any interaction Cl atoms of gas and Ti-atom of ZGNR. Consequently, no splitting is observed, and the $COCl_2$ molecule simply attaches itself to the Ti atom. The electron overlap data from the table confirms a weak bond between Ti and O atoms. Energetically, the reaction in this configuration is the least favorable with an adsorption energy of 1.5853 eV.

3.3.2 Ti-doped DV-ZGNR

The interaction of the Phosgene with the DV-ZGNR substrate is almost identical to the case of SV-ZGNR. One noticeable difference which arises is in the case when C atom is closest to the Ti atom in the initial configuration. The CO molecule, in this case, is observed to be released from the substrate. This is confirmed by the negligible charge overlap between the Ti and O atoms. The C-Cl bond length was observed is 2.28A, which is almost identical to the previous case of SV-ZGNR. The adsorption energy observed in this case, -3.01 eV, is significantly lower than the corresponding SV-ZGNR case, due to the release of CO gas from the substrate. The interaction of the gas in the other two configurations is similar to the DV-ZGNR case. Fig.3.3,(a) depicts the C atom closest on an SV-ZGNR substrate. In (b) Cl atom closest on an SV-ZGNR substrate. (c) showcases O atom

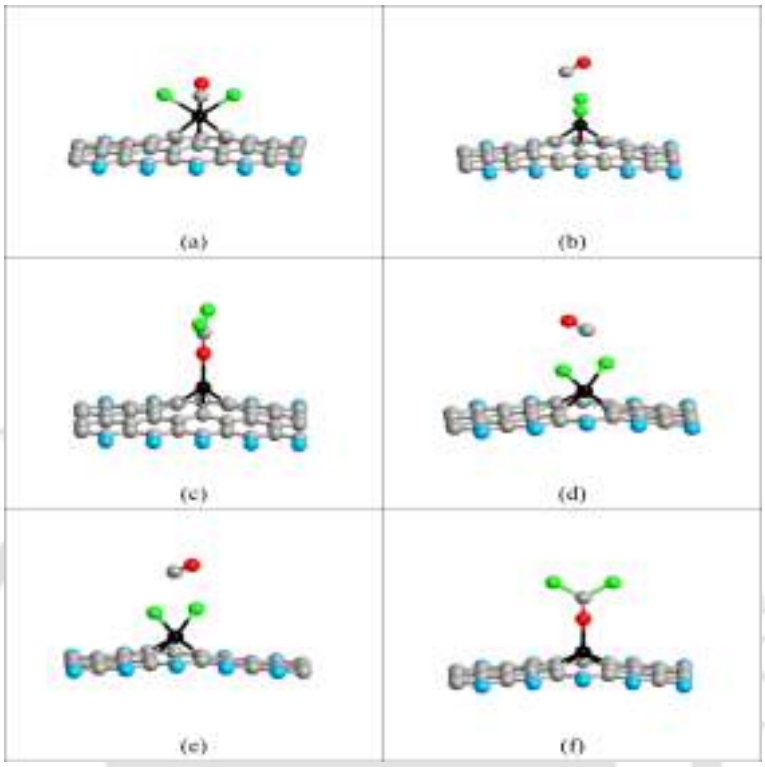

Figure 3.3: The final relaxed structures obtained after the adsorption of Phosgene on Single Vacancy (SV) ZGNR and Double Vacancy (DV) ZGNR substrates.

closest on an SV-ZGNR substrate whereas (d) represents C atom closest on a DV-ZGNR substrate and (e) shows Cl atom closest on a DV-ZGNR substrate. In (f) O atom is closest on a DV-ZGNR substrate. Fig.3.3(d), (e), and (f) show the final relaxed structure of the gas adsorption. Consistent with the previous case of the adsorption on SV-ZGNR substrate, we notice that the Oxygen atom tends to shield the C-Cl bond from the Titanium dopant atom. In this case, Table 3.1 shows that the charge overlap between Titanium atom and the Oxygen atom is 0.281e, which represents a weak covalent bond between the two. The charge overlap between Ti and Cl and C atoms is negligible.

3.3.3 Ti-doped SV-AGNR

The DFT results of relaxation of the base structure for the AGNR indicate that the nanoribbon is stable only in the Single Vacancy case here. The doping in the Double Vacancy case causes the substrate to fold significantly, causing the structure to become unstable. Hence, we have reported the results of the interaction of the gas with the SV substrate only. The results obtained from the simulations on a SV-AGNR substrate are almost identical to the SV-ZGNR case. In fact, the interaction of the gas with the C-atom closest to the substrate results in the splitting of the molecule

Table 3.1: Comparison of the Properties of the Final Relaxed Structure in the Different Cases Studies.(NB)-NO BOND FORMATION

	Bond	Ti-Cl		Ti-C		Ti-O		C-O		Adsorption Energy (eV)
Substrate	*Configuration*	*Bond Length(A)*	*Charge Overlap(e)*	*Bond Length(A)*	*Charge Overlap(e)*	*Bond Length(A)*	*Charge Overlap(e)*	*Bond Length(A)*	*Charge Overlap(e)*	
SV-ZGNR	C Close	2.2711	0.421	2.1936	0.260	3.3289(nb)	-0.006	1.1450	0.861	-3.778
	Cl Close	2.2463	0.431	3.7240(nb)	0.020	4.2878(nb)	0.000	1.1470	0.860	-2.446
	O Close	4.4506(nb)	0.003	3.2513(nb)	-0.012	2.0112	0.262	1.2416	0.679	-1.5853
DV-ZGNR	C Close	2.2826	0.396	3.7994(nb)	0.014	4.3595(nb)	0.000	1.1485	0.857	-3.01
	Cl Close	2.2814	0.398	3.7912(nb)	0.014	4.3524(nb)	0.000	1.1486	0.857	-3.011
	O Close	4.3757(nb)	0.003	3.2262(nb)	-0.010	1.9838	0.278	1.1244	0.670	-1.934
SV-AGNR	C Close	2.2528	0.421	3.7921(nb)	0.016	4.2934(nb)	0.000	1.1472	0.859	-3.336
	Cl Close	2.2665	0.426	2.2043	0.258	3.3412(nb)	-0.006	1.1445	0.862	-4.214
	O Close	4.4036(nb)	0.002	3.2474(nb)	-0.012	2.0081	0.263	1.2426	0.677	-1.785

with the release of the CO molecule. The adsorption energy calculated in this case, -3.36 eV, is almost identical to that in the case of SV-ZGNR with Cl atom closest to the gas. Interestingly, the interaction with the Cl atom closest to the Ti atom does not result in the release of CO, as may be expected. Instead, the CO molecule attaches to the Ti atom. This observation also accounts for the higher adsorption energy (-4.21 eV) observed in the case when the Cl atom is introduced closest to the substrate, than when the C atom is closest to the substrate. The adsorption energy, in this case, is again almost identical to that of the SV-ZGNR case with the C atom closest to the dopant. The interaction with O atom closest to the substrate is again limited by the shielding effect of the Oxygen atom. Electron charge transfer data from Table 3.1 shows the same, with the Ti-O and the C-O bond showing the maximum charge transfer, and minimal charge sharing between the other atoms.

3.3.4 Discussion on Electronic Structure

Next, we look at the Density of States, Band structure, and Electron Density plot for the studied substrates. Since our main aim is to use these substrates in FETs, we need to be able to observe significant changes in the electronic properties of the system before and after the adsorption of the gas molecule. These changes would then result in a change in the I-V characteristics of the devices and produce a measurable change. First, we analyze the change in the Density of States of the system by contrasting the DOS before and after the gas adsorption (Fig.3.4).

The changes in the DOS plots reflect the changes in the I-V characteristics we can expect, and consequently exploit to design a gas sensor on these substrates. The Fermi level in the two devices has been centered to 0 eV. In both cases, we notice a spike in the DOS of the system with the adsorbed gas molecule very close to the Fermi level, at 0eV. This leads to a marked increase in the conductance

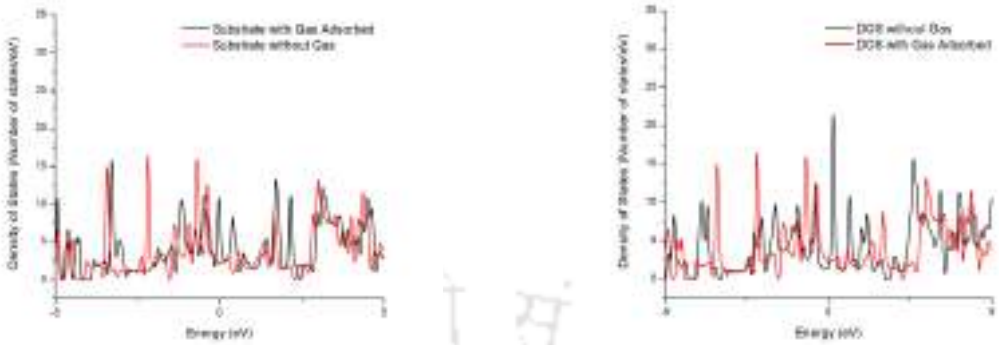

(a) (a) C atom closest on an SV-ZGNR substrate.

(b) (b) Cl atom closest on an SV-ZGNR substrate

Figure 3.4: The density of states for the SV-ZGNR system with Phosgene adsorbed, compared against the underlying substrate DOS (Fermi level adjusted plot)

of the substrate after the adsorption of the gas molecule. These results further support our hypothesis of a detectable change in the current characteristics of the ZGNR substrate. The subsequent analysis we perform is the band structure analysis of the final system, with the gas molecule adsorbed on the system. The band structure data paints an interesting picture of the working of the substrates. We know from the literature [141] that ZGNRs does not have a bandgap. This result is validated by the simulation results we observe. The presence of the Fermi energy level above the bandgap indicates that the FET device having this substrate as a channel, will be an always ON device, and in order to turn it off, we would need negative biases. The SV-AGNR is a different case altogether. In this scenario, the Fermi-level lies within an energy bandgap. This makes this an ideal candidate for use in conventional FET technology. Further, the adsorption of Phosgene has another desirable effect on the zigzag nanoribbon substrate. As discussed previously, pristine zigzag nanoribbons do not have a bandgap. However, the chemical adsorption of Phosgene on the ZGNR substrate leads to the formation of a bandgap in both the SV and DV substrates which can lead to turning off phenomena in the always ON type FET device (Fig.3.7 shows the formation of bandgap after the adsorption of Phosgene, while a similar gap is observed close to, but below, the Fermi energy level in Fig. 3.5a).

While not directly proving it, this result does predict that the adsorption of Phosgene would result in a change of the current-voltage characteristics of such devices. However, to understand the performance of these materials in a FET-based sensor device, various aspects such as coupling of electrode material, i.e., source and drain, and the effect of back gate voltages, which influence the

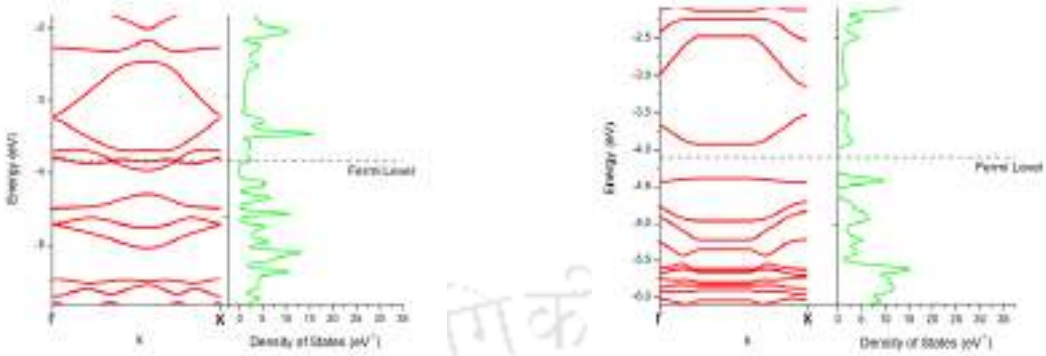

(a) Configuration with C atom closest on an SV-ZGNR substrate.

(b) Configuration with the C atom closest on an SV-AGNR substrate

Figure 3.5: The band structure and corresponding density of states for the SVZGNR and SV-AGNR system after adsorption of Phosgene.

electrostatic fields on the atomic thick channel material (ZGNR), are to be considered. These aspects can be incorporated through the Non-Equilibrium Green Function transport based DFT simulations [142,143]. Previous studies on graphene-based sensors have demonstrated that the electronic structure of graphene makes it immune to electrostatic noise from the environment [144, 145], while atomic Graphene Nanoribbons have also shown excellent structural stability in the ambient environment [146]. In summary, these materials are promising for the development of highly sensitive sensors, which are robust against electrostatic noises. To further understand the nature of the interaction observed previously, we now plot the electron charge density of the systems. These diagrams show an interesting result. The take-away from these is that at the chemical adsorption site on the substrate, there is a local migration of the electrons into the Cl atom, and away from the Ti atom, which is as expected due to electro-negativity difference between the two atoms.

Fig.3.6 shows the iso-surface corresponding to an iso-value of 0.2, as obtained from DFT calculations at each point in the unit cell lattice. The gas was introduced with the C atom closest to the Ti atom. The final structure shows the splitting of the C-Cl bonds, as well as the subsequent formation of CO, which forms a weak covalent bond with the Ti atom. The isosurface corresponds to isovalue of 0.2. The figure shows that after the adsorption, charge is accumulated mostly over chlorine atoms, indicating a migration of electrons to the Cl atom. In Fig 3.7 The adsorption of $COCl_2$ causes the formation of a bandgap (0.085 eV in this case) in the zero bandgap zizag graphene nanoribbon substrate. The formation of the bandgap allows us to use these substrates as FET transistors which

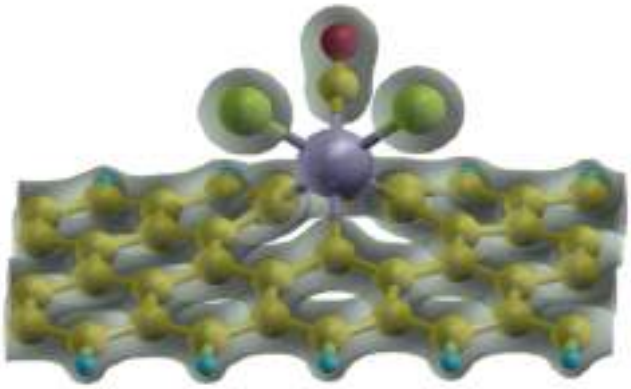

Figure 3.6: The electron density plot of the relaxed zigzag graphene nanoribbon substrate after the adsorption of the gas.

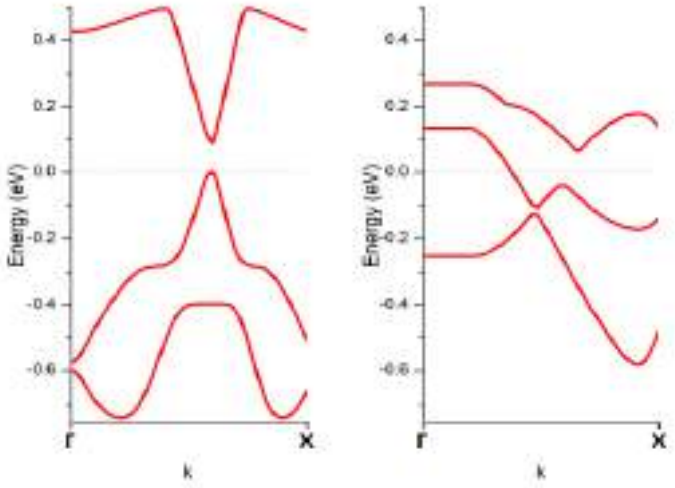

Figure 3.7: Bandstructure before and after adsorption of Phosgene on the DVZGNR substrate.

can be turned off after the adsorption of Phosgene. (Note: The Fermi level for both structures has been centered to 0 eV. In an absolute sense, however, this does not correspond to the same energy value). Our electronic analyses so far demonstrate that there are significant changes in the electronic structure of the devices before and after adsorption.

3.4 Comparative Analysis of Adsorption of Similar Gases

To further understand the nature of the interaction observed previously, similar studies were carried out for $SOCl_2$ and $POCl_3$, which have a similar structure to that of phosgene. Again, during the simulations, the gas was introduced in various unique configurations on the different substrates. The

results obtained from the simulations agree with the observations made previously. Firstly, a general trend of shielding is observed when the O-atom is close enough to interact with the substrate. This is observed in the interaction of both $POCl_3$ and $SOCl_2$ with the sensing substrates. However, interestingly, in the interaction of $SOCl_2$ with the DV-ZGNR substrate, a departure from this trend is observed, with one of the S-Cl bonds being split even with Oxygen shielding present. In all other cases, the oxygen atom prevents the direct interaction between the other atoms of gas and substrate. The interaction in other configurations is less generalizable. However, in all cases, a catalytic split in the Cl-central atom bond due to the Ti atom is observed. In $POCl_3$, different substrates and configurations cause the split of either one or two P-Cl bonds.

3.5 Summary

Previously, studies have been carried out to investigate the sensing behavior of various substrates for phosgene. However, the catalytic effect of doped graphene sheets has not been explored previously. A study carried out by Zhang et.al. [147] reported interaction energy of -1.065 eV on Ti-doped single vacancy graphene sheet. Further, the interaction of BN with Phosgene has also been previously reported, indicating variable values ranging from -1.058eV to -6.328 eV [136]. Our simulation studies indicate that the doped Titanium atom of the Graphene Nanoribbon substrate acts as a catalyst for the splitting of the C-Cl bond. The results of simulation studies indicate that in all configurations in which the Ti atom interacts with the C-Cl bond, a split is observed. However, in the configuration in which the O atom appears closest to the Ti atom, a shielding effect takes place, and consequently, no splitting takes place. The electron overlap data indicates that in this case, adsorption of phosgene on the substrate takes place. This result has previously been reported in the literature. Further, analysis with similar gases further indicate that the splitting of the P-Cl and S-Cl bond also takes place in the presence of Titanium, indicating that the presence of the oxygen on the central atom, and the presence of Ti atom allows the Cl atoms to break free, and the remaining molecule forms a complex with the sensing substrate.

4

Adsorption of Urea over Transition Metal Doped Graphene: A DFT Study

Contents

Outline This work deploys the Density Functional Theory (DFT), to study the interactions between Urea with pristine and transition metal (TM) doped two-dimensional graphene structures. Four TM-dopants, namely, V, Ti, Fe, and Cr, are considered in this study. Each of these doped structures has one TM-atom replacing one carbon atom from two-dimensional graphene sheets. Our results indicate that TM-doped graphene possesses strong chemical interactions with urea molecule and hence, has a better affinity towards urea as compared to pristine 2-D graphene sheet. Significant charge transfer has also been observed between TM and O-atoms. Moreover, among all the TM-doped structures, V-doped structure is preferred in terms of adsorption energy. The electronic structure also changes after adsorption, which can be observed through the change in the density of states (DOS). Our study suggests that TM-doped graphene have the potential to be the sensing platform for Urea.

4.1 Introduction

Urea, also known as carbamide is an organic molecule with two amine groups attached to a carbonyl group with a chemical formula of NH2-CO-NH2. It first came into notice of a Dutch chemist Herman Boerhaave while working with evaporates of urine in the year 1727 [148]. After that, the procedure of obtaining urea from urine evolved over almost a century until Friedrich Whler discovered the artificial synthesis in the year 1828 [149]. Since then, this compound has gained significant importance and is heavily used in laboratories, explosives, and chemical industries [150–153]. In the area of agriculture, medical, and human health, urea plays a crucial role. In agriculture, urea is widely used as a cost-effective fertilizer with high nitrogen content. Therefore, it can boost plant growth and crop production Moreover, the overuse of urea acidifies the soil, and hence, various preventive actions are being taken to avoid the same [154–156]. In mammals, ammonia is produced during the metabolism involved with amino acids and nitrogenous compounds, which is very toxic. This ammonia is converted to urea and CO_2 by the liver through a series of biochemical reactions known as urea cycle [157]. The produced urea is carried to the kidneys through blood where it is finally excreted out from the body through urine. The amount of urea in the blood can thus provide vital information about the health of liver and kidney. The corresponding test for the same, in medical terms, known as Blood Urea Nitrogen (BUN) [158]. Therefore, it is imperative to estimate the concentration of urea in both environmental entities such as soil, groundwater, as well as in human body fluids like blood and urine. In the past few years, developments of two-dimensional materials such as graphene have gained

popularity in almost every research community, especially the sensor community [159]. The two-dimensional nature has enabled various extraordinary properties such as high thermal and electrical conductivities, high surface to volume ratio, fulfilling the prime requirement of a sensing layer [160]. Moreover, the planer nature makes it ideal for integration with field-effect transistor (FET) fabrication, thus creating a highly sensitive sensing platform [161, 162]. The pristine graphene does not possess significant interactions with many sensing targets like toxic gases, biomolecules. But, these interaction capabilities towards the target can be significantly altered by doping [163]. Theoretical studies have shown that doping of graphene with transition metal atoms can significantly improve the adsorption of carbonyl group containing organic compounds such as HCHO [164, 165]. The transition metals are also known to have a strong interaction with the oxygen- containing compounds. Therefore, doping with TM atoms can result in strong adsorption of such gases, and they exhibit strong oxygen reduction reactions [166]. Furthermore, these doped structures can be synthesized in laboratories, and they show excellent thermal stabilities; hence, they are fancied for sensing applications. During this study, our focus is to investigate the interaction of urea molecule with transition metal doped two-dimensional graphene sheet through the density functional theory based simulations. V, Ti, Fe, and Cr are the four TM-dopants considered as they exhibit strong interactions with oxygen and carbonyl-containing compounds, and few of them are already synthesized and experimentally studied [167–170]. For this study, we incorporated a simple doping strategy in which the dopant will substitute a C-atom from the layer. This type of strategy has already been explored in most of the cases because they are easy to analyze, yet can provide deep insight. The study of adsorption process comprises various unique configurations of urea molecule over graphene and doped graphene. The changes in electronic properties before and after the adsorption are analyzed, through the change in the density of states. We observed that pristine graphene have very weak interaction, whereas the doped graphene has significant interactions with the molecule. Further, the adsorption process is thoroughly investigated in terms of change in bond lengths, adsorption energies, and charge transfer. Our results demonstrate that doped graphene can be used to develop a sensing platform for urea.

4.2 Computational Details

The first principle density functional theory calculations are performed using the SIESTA package [171, 172]. The electron-electron exchange-correlation energies are estimated with Perdew, Burke,

Figure 4.1: The optimized 55 pristine graphene sheet, carbon atoms are in grey.

and Ernzerhof (PBE) exchange functionals within the generalized gradient approximation (GGA) [173]. The Troullier-Martins pseudopotentials are used to incorporate the interaction between ions and electrons. The double zeta basis plus the polarization orbital (DZP) basis set is used to construct atomic orbitals [174]. We have considered a 55 graphene sheet, as shown in Figure 4.1 and Figure 4.2 with 50 carbon atoms. During doping, one carbon atom is replaced by a TM-atom, resulting in 2% of doping [175, 176]. The k-point grid is taken as 771 with 350 Rydberg as the mesh cut off. Before performing the adsorption and electronic structure calculations, each structure was relaxed using conjugate gradients (CG) algorithm. The force tolerance was taken to be less than 0.01 eV/Angstrom. The unit cell is periodic in the x and y-plane; a vacuum region of more than 15 Angstroms is kept in the z-direction to avoid interactions from neighboring cells.

The strength of the interaction between urea and graphene is analyzed using adsorption energy (Eads). The adsorption energy can be estimated using Equation-1, given below:

$$E_{ads} = E_{Substrate+Urea} - (E_{Substrate} + E_{Urea}) \tag{4.1}$$

Where, $E_{Substrate+Urea}$ is the energy of the urea adsorbed over the substrate, $E_{Substrate}$ is the energy of the substrate, and E_{Urea} is the energy of isolated urea molecule.

H

(a) Cr doped, carbon atoms are in gray and Cr atom is light blue color balls

(b) V doped, carbon atoms are in gray and V atom is light gray color balls

(c) Ti doped, carbon atoms are in gray and Ti atom is in white color balls

(d) Fe doped, carbon atoms are in gray and Fe atom is orange color balls

Figure 4.2: The TM-doped 55 graphene sheets

4.3 Results and Discussion

The interaction and adsorption of urea molecule with graphene and doped graphene are studied in two steps: first, the simulation has been carried out to estimate the nature and strength of adsorption for pristine graphene. Secondly, the effect on the adsorption phenomenon caused by TM-doping is assessed. The urea molecule was introduced over the sheet in several different but unique orientations for each case. This consists of urea molecule's parallel planer and perpendicular orientations over the sheet. There are a total of 11 such orientations. Each case was thoroughly analyzed in terms of adsorption energy, charge transfer, and change in structural, electronic properties. Following sections describe the same.

4.3.1 Urea over Pristine Graphene:

Initially, the graphene sheet and urea molecule were relaxed individually. Post relaxation, length of the C-C bond was found to be 1.42 Angstroms that is in accordance with other theoretical and experimental works [177]. The urea molecule after relaxation possessed C-O, C-N, and N-H as 1.225, 1.281, and 1.010 Angstroms, respectively, which are again in concurrence with the experimentally reported values in the literature [178].

To get the most energetically favorable position, adsorption energy was calculated for each orientation using Equation-1. It was observed that the urea molecule tends to be adsorbed in a parallel planer manner as shown in Figure 3 with Eads -0.776 eV which is more than the value for single walled

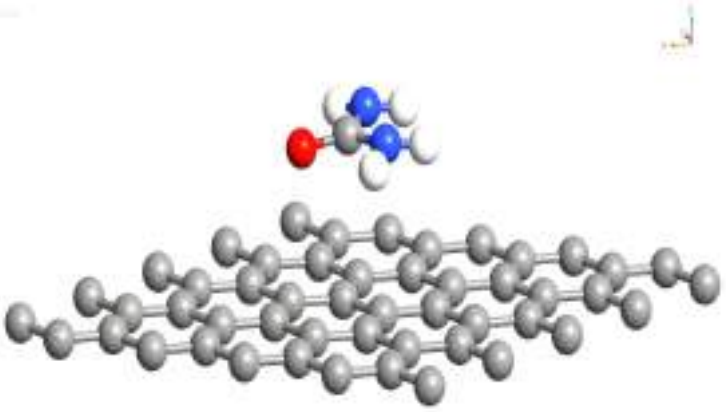

Figure 4.3: The optimized structure obtained after urea adsorption over pristine graphene. Carbon, nitrogen, oxygen and hydrogen atoms represented with gray, blue, red and white color balls respectively.

boron nitride nanotubes and KCl surface but less than the reported value for ZnO surface [179–181]. The structural changes both in sheet and molecule are estimated through the change in bond lengths, as shown in Table 4.1.

Table 4.1: The comparison of bond-lengths for pristine, TM-doped graphene and urea molecule before and after the adsorption.

Substrate		Substrate Bond Lengths		Urea Bond Lengths			Nearest Atom and Distance	
		C-C	C-TM	C=O	C-N	N-H	Nearest atoms	Distance
Pristine Graphene	*Before Adsorption*	1.421	-	1.225	1.381	1.01	-	-
	After Adsorption	1.42	-	1.231	1.383	1.014	C-O	2.86
V-doped Graphene	*Before Adsorption*	1.412-1.437	1.889-1.904	1.225	1.381	1.01	-	-
	After Adsorption	1.414-1.439	1.887-1.915	1.273	1.341-1.355	1.01-1.02	V-O	2.003
Ti-doped Graphene	*Before Adsorption*	1.413-1.432	1.925-1.926	1.225	1.381	1.01	-	-
	After Adsorption	1.411-1.437	1.922-1.953	1.271	1.342-1.356	1.01-1.02	Ti-O	2.05
Fe-doped Graphene	*Before Adsorption*	1.415-1.429	1.782-1.783	1.225	1.381	1.01	-	-
	After Adsorption	1.420-1.433	1.763-1.767	1.272	1.343-1.356	1.01-1.02	Fe-O	1.91
Cr-doped	*Before Adsorption*	1.410-1.438	1.902-1.903	1.225	1.381	1.01	-	-
	After Adsorption	1.412-1.423	1.896-1.908	1.271	1.343-1.356	1.01-1.02	Cr-O	2.006

As per the values form Table 4.1, no significant change in the bond length was observed. The nearest atom to the sheet is O-atom, which is around 2.86 Angstroms from the sheet. The high distance between the molecule and the sheet and low adsorption energy reflects that the interaction nature is weak chemisorption. In order to observe the change in the electronic structure after adsorption, DOS

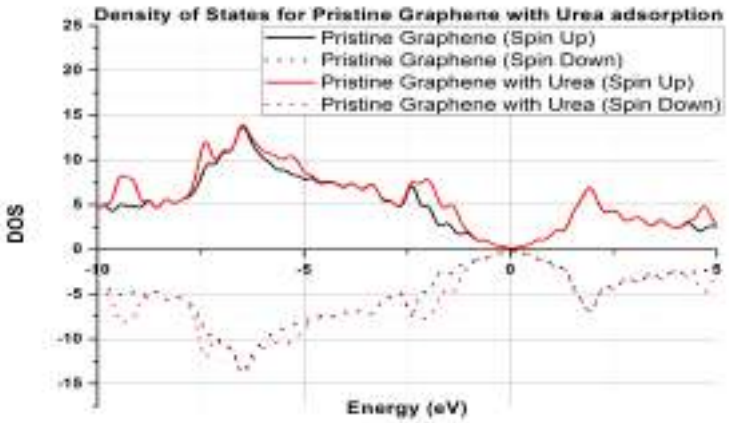

Figure 4.4: The density of states (arb. units) plot for pristine graphene before and after urea adsorption with Fermi level shifted to zero.

was calculated, as presented in Figure 4.4. There are slight changes between -5 to 0 eV in DOS plot after adsorption, but no changes at Fermi level were observed. The charge transfer was calculated through Mulliken Population analysis; in this case, a very small charge 0.065e transfer from layer atoms to atoms of urea was observed, reflecting that the adsorption process is weak chemisorption

4.3.2 Urea over V-doped Graphene

The relaxation of V-doped graphene sheet was carried out initially. After relaxation, the C-C bond length in the sheet was found to be in the range of 1.413-1.432 Angstroms, which is due to the presence of V-atom, causing deformations in the pristine graphene structure. Whereas, the C-V bond length was 1.88-1.90 Angstroms, which is in accordance with the available other theoretical and experimental works in the literature [177, 182]. As before, after analyzing adsorption energy for each orientation, it was observed that the urea molecule tend to be adsorbed in the perpendicular manner rather than parallel planer manner that is observed in the former case. The distance between O and V atom of the sheet is approximately 2.003 Angstroms as shown in Figure 4.5 with adsorption energy of -2.792 eV (which is significantly higher than the values reported in the literature and tabulated in Table 4.2).

The reason for such high adsorption energy is twofold. First, it is due to the strong interaction between V and O-atoms, which is confirmed through the significant charge shared (0.249e) between them. Second is due to adsorption in the perpendicular manner; therefore, not only oxygen but

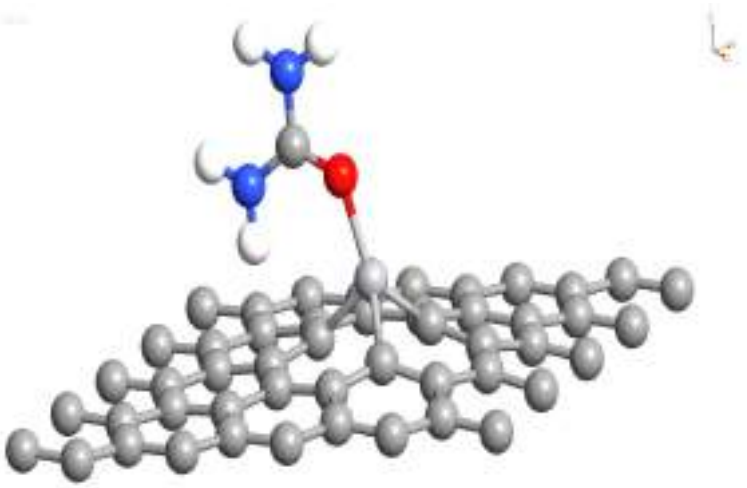

Figure 4.5: The optimized structure obtained after urea adsorption over V-doped graphene. Carbon, vanadium, nitrogen, oxygen and hydrogen atoms represented with gray, light gray, blue, red and white color balls respectively.

other atoms of the molecule (particularly the hydrogen atom near to sheet) is also interacting with C atom of the sheet through small charge sharing. Hence, together, they amplify the adsorption process, resulting in high adsorption energy in this case. The evidence of this strong interaction can be visualized in terms of changes in the bond lengths (Table 4.1) of urea molecule and V-doped graphene after adsorption. During the adsorption process, a total of 0.127e charge was transferred to the graphene layer by urea molecule. Moreover, due to the presence of unpaired d-orbital electrons, V-doped graphene exhibit magnetic behavior with a total magnetic moment of about 1.086 B [182]. However, due to the interactions (charge sharing/transfers) with urea molecule, the magnetic behavior gets affected and the total magnetic moment for the system after the adsorption was observed to be around 1.0 μB.

The change in electronic properties can be observed through DOS plot shown in Figure 4.6. There were significant changes, which can be observed at Fermi level as well as for the entire range of -10 to 5 eV in DOS plot after adsorption. It suggests that V-doped graphene can be used as a sensing layer in electronic sensor platforms.

4.3.3 Urea over Ti-doped Graphene

As before, after the relaxation, the C-C bond lengths were found to be in the range of 1.413-1.432 Angstroms. It is due to the deformations caused by Ti-doping in the graphene structure. Whereas, the C-Ti bond length was 1.925-1.926 Angstroms, which is in accordance with theoretical and experimental

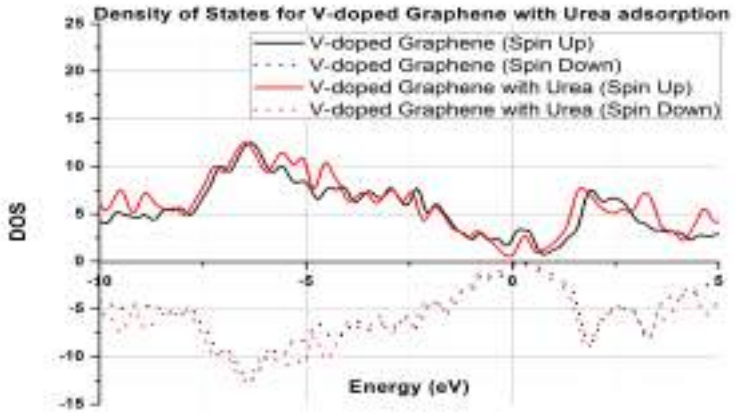

Figure 4.6: The density of states (arb. units) plot for V-doped graphene before and after urea adsorption with Fermi level shifted to zero.

works in the literature [177, 182]. After careful analysis of adsorption energies for each case, similar to the previous case, the urea molecule tends to get adsorbed in the perpendicular manner as shown in Figure 4.7, with Eads -2.702 eV (Table 4.2) having a distance of approximately 2.05 Angstroms between O and Ti atom of the sheet.

Table 4.2: The comparison of adsorption energies for urea adsorption over TM-doped graphene with that of other adsorbent surfaces reported literature.

S.No.	Adsorbent	Theory	Adsorption Energy	Ref.
1.	Single walled Boron Nitride Nanotubes	DFT-GGA	-0.325 eV	[32]
2.	ZnO (1 00) surface	DFT-GGA	-1.613 eV	[33]
3.	KCl Surface	DFT-GGA	- 0.65913eV for {100} orientation	[34]
			-0.88029 eV for {110} orientation	
			-0.86295 eV for {111} orientation	
4.	Pristine Graphene	DFT-GGA	-0.776 eV	This work
5.	V-doped Graphene	DFT-GGA	-2.792 eV	
6.	Ti-doped Graphene	DFT-GGA	-2.70 eV	
7.	Fe-doped Graphene	DFT-GGA	-2.460 eV	
8.	Cr-doped Graphene	DFT-GGA	-2.439 eV	

The adsorption energy was observed to be slightly less as compared to the previous case of V-doping. In this case, urea donates 0.141e charge to the graphene layer, which is more, but charge shared between urea molecule and layer is less in this case as compared to the previous case. The similar changes in the bond lengths after adsorption observed are summarized in Table 4.1. However,

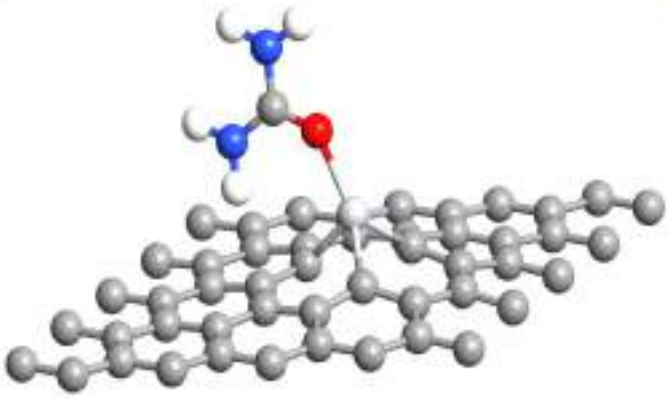

Figure 4.7: The optimized structure obtained after urea adsorption over Ti-doped graphene. Carbon, titanium, nitrogen, oxygen and hydrogen atoms represented with gray, light gray, blue, red and white color balls respectively.

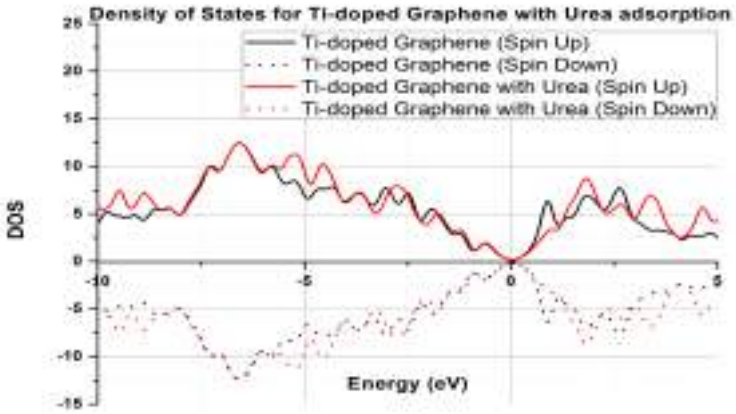

Figure 4.8: The density of states (arb. units) plot for Ti-doped graphene before and after urea adsorption with Fermi level shifted to zero.

unlike the previous case, Ti-doped graphene exhibited no magnetism, i.e., the total magnetic moment for the system was observed to be zero [182], which remains unchanged even after adsorption of urea molecule. Significant changes were observed in the DOS plot (Figure 4.8) between 0-5 eV and between -10 to -1eV after adsorption, but no changes were observed at Fermi level, which was present in the previous case.

4.3.4 Urea over Fe-doped Graphene

In this case, due to the deformation caused by Fe-atom, after the relaxation, the C-C bond lengths were found to be in the range of 1.415-1.429 Angstroms. Whereas, the C-Fe bond length was 1.782-

1.783 Angstroms, in accordance with other theoretical and experimental works in the literature [177, 182]- [183].

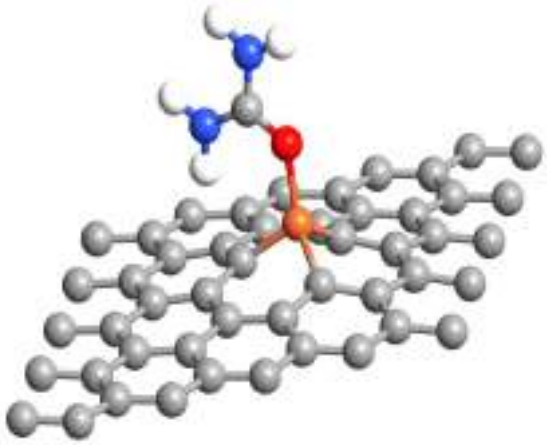

Figure 4.9: The optimized structure obtained after urea adsorption over Fe-doped graphene. Carbon, iron, nitrogen, oxygen and hydrogen atoms represented with gray, orange, red, blue and white color balls respectively.

Again, in this case, the urea molecule tends to get adsorbed in the perpendicular planer manner similar to V and Ti-doped cases with Eads -2.460 eV (Table 4.2), as shown in Figure 4.9. The distance between O and Fe atom of the sheet was approximately 1.91 Angstroms. In this case, the total charge transfer to layer was 0.084e, which is less, but the charge shared between urea molecule and layer was more than previous cases. The similar pattern in the variation of the bond lengths after adsorption can be observed in Table 4.1.

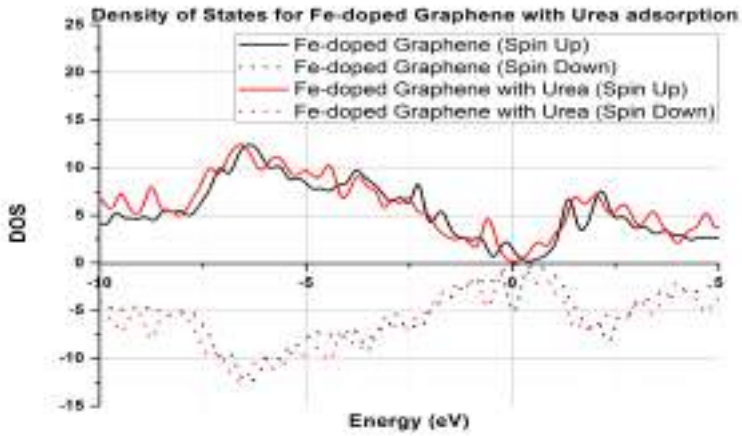

Figure 4.10: The density of states (arb. units) plot for Fe-doped graphene before and after urea adsorption with Fermi level shifted to zero.

The magnetic moment for the Fe-doped graphene changed from 1.73 μB to zero upon adsorption.

The changes in DOS plot can be observed in Figure 4.10. The changes were not only at Fermi but also over the entire energy range, which is similar to that of the V-doped case.

4.3.5 Urea over Cr-doped Graphene

After relaxation, the C-C bond lengths were found to be in the range of 1.410-1.438 Angstroms whereas the C-Cr bond length was 1.90 Angstroms, which is in accordance with the available theoretical and experimental works [177, 182]. The trend of urea molecule adsorption in the perpendicular planer manner as the rest of the doped cases continues here with Eads -2.439 eV (Table 4.2), and the distance between O and Cr atom of the sheet was approximately 2.006 Angstroms as shown in Figure 4.11.

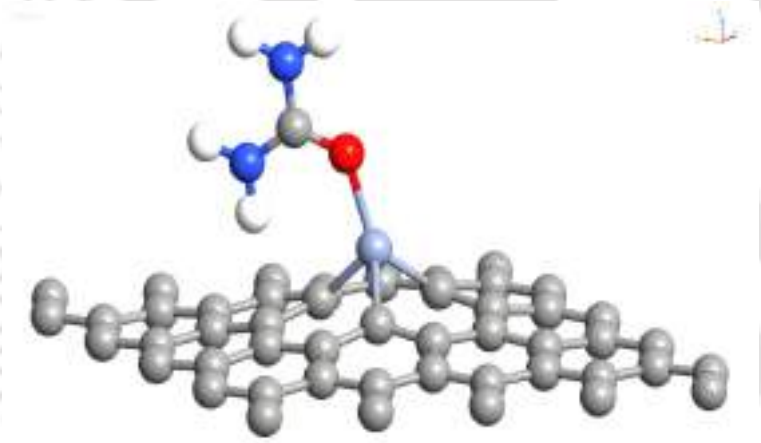

Figure 4.11: The optimized structure obtained after urea adsorption over Cr-doped graphene. Carbon, chromium, nitrogen, oxygen and hydrogen atoms represented with gray, light blue, blue, red and white color balls respectively.

In this case, the total charge transferred to layer was 0.11e, which is slightly higher, but the charge shared between urea molecule and layer was less than the previous case of Fe-doping. Again, the trend in the change of bond lengths after adsorption continues, as showcased in Table 4.1.

Moreover, the Cr-doped graphene exhibit magnetism with a total magnetic moment of about 2.16 μB, that was slightly decreased to 2.0 μB upon adsorption of urea molecule. Even here, the significant change in DOS at Fermi and over the entire energy range can be observed in Figure 4.12, which is similar to the V and Fe-doped case.

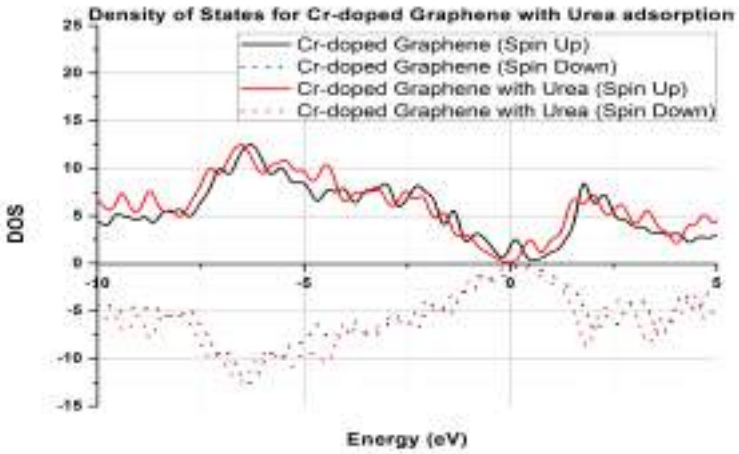

Figure 4.12: The density of states (arb. units) plot for Cr-doped graphene before and after urea adsorption with Fermi level shifted to zero.

4.4 Summary

The objective of this paper is to study the interaction of the urea molecule over pristine as well as TM-doped 2-D graphene sheets. The interaction between urea and pristine graphene sheet is very weak and caused by weak chemisorption. Hence, change in electronic properties is inconsiderable, and so is the charge transfer. Whereas, the interaction with the doped graphene sheet is very strong, caused by strong chemisorption, resulting in significant changes in electronic properties and large charge transfer. The charge transfer was from the molecule to layer for each doping case. All the TM-doped graphene structures involved in this study exhibit significantly higher adsorption energy as compared to the reported values for several other adsorbent surfaces, as showcased in Table 4.2. Finally, after a thorough analysis of each case, it is observed that V-doped graphene has the strongest interaction with urea. In this case, a significant charge is transferred to the layer. Hence, V-doped graphene can be an excellent candidate for urea adsorption. After the adsorption, the electronic properties are significantly modified as well; therefore, V-doped graphene can be used as a sensing layer in electronic sensing platforms such as chemi-resistor or FET. Therefore, it can be concluded from our study that the doped graphene is a good candidate for developing point of care (POC) diagnostic devices.

5

First Principle Study of Adsorption of Chlorofluorocarbons over Ti-doped Two-Dimensional Graphene Sheet

Contents

Outline The work utilises Density Functional Theory (DFT) to showcase the interaction and adsorption of the three most polluting Chlorofluorocarbons (CFC) molecules namely $CFCl_3$, $CClF_3$, and CCl_2F_2 with pristine and Ti-doped two-dimensional graphene sheet. Substitutional doping of one Ti-atom with one carbon atom from a two-dimensional graphene sheet is considered. An optimum orientation and configuration of each CFC molecule are obtained on graphene and Ti-doped graphene with the help of geometry optimizations. The obtained results indicate strong chemical interaction of the Ti-doped graphene with the Cl atom of the CFC molecules exhibiting better affinity towards the molecules in comparison to pristine graphene sheet. Moreover, in the case of $CFCl_3$ and CCl_2F_2, the strong interaction between Ti and Cl atom can result in de-chlorination which is splitting of C-Cl bond. This forms a free radical entity that is weakly adsorbed over the sheet, whereas the chlorine atom gets attached to the Ti-atom. However, for $CClF_3$ no such effect was observed as the de-chlorination energy required is more compared to the previous case. Apart from a few cases of splitting, strong adsorption of these gases over Ti-doped graphene was observed compared to weak adsorption in pristine graphene. Also, a significant transfer of charge is noticed between Ti and CFC molecules. The variation in the electronic structure after the adsorption was estimated and analysed through the change in the density of states (DOS). The results suggest that Ti-doped graphene has the potential to be the sensing platform for CFC molecules.

5.1 Introduction

Chlorofluorocarbons or CFCs are fully halogenated hydrocarbons that contains only carbon, chlorine, and fluorine atoms. Due to their low boiling points, they are widely used as refrigerants, and propellants [184]. Commercially they are known as Freons, which is a trade name for a group of CFC produced by the DuPont Company [185]. In 1890s, Frdric Swarts, a Belgian scientist perfected the indirect fluorination process of the production of chlorofluoro compounds. In 1892, he demonstrated the application of antimony fluoride (treated with chlorine or antimony pentafluoride, called as Swartz reagent) as a fluorinating agent, which can effectively replace the chlorine atoms of chloro compound; the reaction is known as Swarts reaction [186]. Later, he also demonstrated mercurous fluoride for the same process. With the aid of these reagents, he was able to synthesize and isolate trichlorofluoromethane and various other chlorofluoro compounds. However, these CFCs were not used as refrigerant until the 1920s. In late 1920s, an American engineer Thomas Midgley Jr. along with his

team members proposed trichlorofluoromethane as an alternative to the traditional refrigerant such as ammonia. The team also improved the Swartz's method to produce the CFCs efficiently [187]. After that, CFCs were widely used for refrigeration, aerosol in world war-II, etc. But in later decades, the harmful effects of CFCs, particularly ozone depletion were realized by the scientists [188]. Therefore, it was started regulated in 1976 and then in 1987, it was decided to start reducing and completely eliminate the production of CFCs in the Montreal treaty [189]- [190]. But, there was no clause for recycling CFCs in the treaty, and there are serious worldwide issues related to the smuggling of CFCs. The existing CFCs whether in the warehouses or in existing equipment which will be eventually released in the atmosphere once their life time is over were also not regulated under the treaty [191]. Therefore, the atmospheric levels of CFCs are not dropping as per the expected levels, and in the case of a few CFCs, the levels are increased in last few years. Hence, the CFCs is still a big problem to the environment and their concentration estimation is vital.

Other than as refrigerants, CFCs are regularly used in laboratories as solvents and in various protocols such as oil-in-water assays. They are widely used in hydrology studies, and sometimes, they are produced as by-products. $CFCl_3$ is also used as an NMR reference [192]- [193]. Due to their frequent use, laboratories are also becoming a major source of CFC pollution, and such laboratory environments have adverse effects on health. Groppi et al. studied the effects of $CFCl_3$ inhalation, gas chromatography analysis shows its concentration in various issues. The highest concentration was found in heart tissues which causes the toxic action which finally results into arrhythmia and cardiac arrest along with hypoxemic asphyxiation [194]. A study conducted by Oenbrink described the adverse effects of $CFCl_3$, and CCl_2F_2 as medication propellants on patients [195]. $CFCl_3$ is readily used in NASA space missions, and since it is most cardio toxic of all CFCs and can affect central nervous system therefore during the missions exposures have to be carefully monitored, the acceptable maximum concentration for $CFCl_3$ should not be more than 140ppm [196]. CFCs are not soluble in water, but due to salinity and higher temperature, they are soluble in seawater, and various studies are conducted to monitor their presence in sea water [197]. Hence, CFC concentration estimation is becoming a necessity.

Graphene is a two-dimensional arrangement of carbon atoms in hexagonal lattice. It was discovered by Novoselov and Geim in 2004 [198] and is known to be the strongest material. The two-dimensional nature enables its unique electrical, thermal transport properties which are fancied for electrical device

prospective [199]- [200]. Also, it gives graphene a very high surface-to-volume ratio. Due to this, graphene is ideal for adsorbent and sensor applications [201]. Pristine graphene sheets are explored for gas adsorption and gas sensing as well as biosensors [202]. In some cases, the pristine graphene properties are not well suited. However, the desired properties can be easily altered with doping or functionalization [203]. Doping can improve the adsorption and sensing capabilities towards the target. Moreover, doping with transition metal atoms can enable unique catalytic properties and add new application areas such as oxygen reduction or in fuel cells [204]. The transition metal doping can significantly improve their interaction and hence adsorption of organic compounds with carbonyl as well as halogen groups [205], [206], [207]. These doped structures have been synthesized, and they possess good stabilities therefore, the doped graphene structures are appropriate for sensing applications and gained popularity among the research community.

The focus of this work is to determine the interactions of the three most polluting CFC molecules $CFCl_3$, $CClF_3$, and CCl_2F_2, with Ti-doped two-dimensional graphene sheet using the first principle DFT simulations. The doping with the Ti atom is considered because it exhibits strong interactions with halogen atoms. The doping strategy in which the dopant substitutes a C-atom from the graphene layer is incorporated in this study. Such doping strategies are straightforward in analysis and still can provide deep insights. In this study, several unique configurations of CFC molecules on graphene and doped graphene have been considered. Each configuration has been thoroughly investigated for change in bond lengths, adsorption energies, and charge transfer. The post adsorption variation in electronic properties were estimated by evaluating the change in the density of states. It was observed that the doped graphene has significant interactions with the CFC molecules as compared to the pristine graphene, which have very weak interaction. Further, it can be inferred from the results that graphene doped with Ti-atom could be a promising candidate to be used in sensing platforms for CFC molecules.

5.2 Computational Method

The calculations of the first principle DFT are conducted with the SIESTA package [208]- [209]. Also, Perdew, Burke, and Ernzerhof's (PBE) exchange functionals are utilized to reckon the electron-electron exchange-correlation energies. The calculations are made within generalized gradient approximation (GGA) [210]. The ions and electrons interactions are estimated by utilizing Troullier-Martins

pseudopotentials [211]. Atomic orbitals are constructed with double zeta basis and the polarization orbital (DZP) basis set.

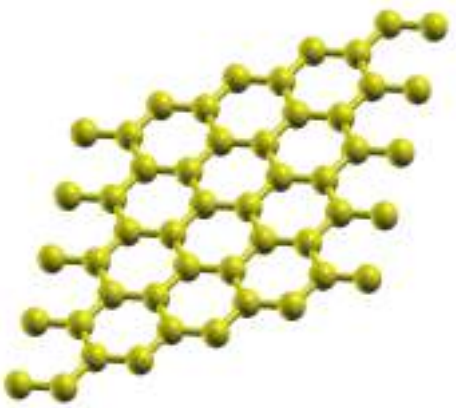

Figure 5.1: The optimized 5×5 pristine graphene sheet. The carbon atoms are in yellow.

As depicted in Fig.5.1 and Fig. 5.2, a 5×5 graphene sheet with 50 carbon atoms is being considered for our proposed work. Also, we have taken doping of 2%, which is obtained by replacing one carbon atom with one TM atom [212]- [213]. A $7 \times 7 \times 1$ K point grid with 350 Rydberg is taken as the Mesh cutoff. Every structure is first relaxed by utilizing the conjugate gradient (CG) algorithm, and then adsorption and electronic structure computations are performed. The force tolerance is considered below 0.01ev/Angstrom. The periodicity of a unit cell is maintained in x and y planes. However, to prevent interactions among neighboring cells, a vacuum region more significant than 15 Angstrom is retained in the Z direction.

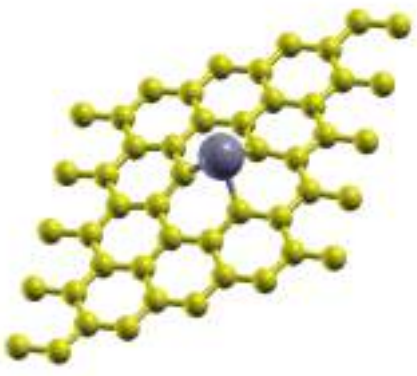

Figure 5.2: The optimized 5×5 pristine graphene sheet. The carbon atoms are in yellow and Ti atom is in grey.

Table 5.1: The comparison of bond-lengths, adsorption distance, and charge transfer for pristine graphene and CFC molecules before and after the adsorption.

Gas		Substrate Bond Length (in Angstroms)	Gas Bond Lengths (in Angstroms)		Nearest Atoms	Distance (in Angstroms)	Charge Transfer
		C-C	C-Cl	C-F			
$CFCl_3$	Before Adsorption	1.421	1.774, 1.774, 1.774	1.351	–	–	–
	After Adsorption	1.420	1.778, 1.777, 1.778	1.352	C-Cl	3.161	0.034e
CCl_2F_2	Before Adsorption	1.421	1.773, 1.774	1.346, 1.346	–	–	–
	After Adsorption	1.420	1.774, 1.769	1.352, 1.351	C-Cl C-F	3.187 2.743	0.044e
$CClF_3$	Before Adsorption	1.421	1.772	1.342, 1.343, 1.343	–	–	–
	After Adsorption	1.420	1.772	1.346, 1.345, 1.337	C-F C-Cl	2.807 3.195	0.042e

5.3 Result and Discussion

During this study, a 5 x 5 graphene sheet with 50 C atoms have been considered. After the optimization, the C-C bond length was found to be 1.421$\mathring{A}$, which is in good accordance with the reported literature [199]. Also, the CFC molecules were individually optimized followed by optimization of CFC molecules over graphene sheet. The adsorption energy (E_{ads}) is utilized to analyze the interaction strength between graphene and CFC molecules. Equation (1) gives the estimation of adsoption energy:

$$E_{ads} = E_{Substrate+CFC} - [E_{Substrate} + E_{CFC}] \tag{5.1}$$

$E_{Substrate+CFC}$ is the energy of the CFC molecule adsorbed on the substrate, whereas, $E_{Substrate}$ is the energy of the substrate, and E_{CFC} is the energy of isolated CFC molecule.

5.3.1 $CFCl_3$ over Pristine Graphene

Before the adsorption studies, the $CFCl_3$ molecule was optimized first and the obtained bond-lengths were found to be in good agreement with the literature and database [214]. For the adsorption study, the molecule was oriented in six different posssible orientations over the graphene sheet and then then relaxed. After the relaxation of individual cases, it was observed that the $CFCl_3$ molecule prefers to adsorb in a fashion all the Cl atom near the sheet as shown in Fig.5.3 with an adsorption energy of -0.665 eV.

The distance between the Cl atoms and nearest carbon atoms was 3.161$\mathring{A}$. There were no significant changes in the bond length of the graphene sheet (Table5.1). However, there was a minute variation

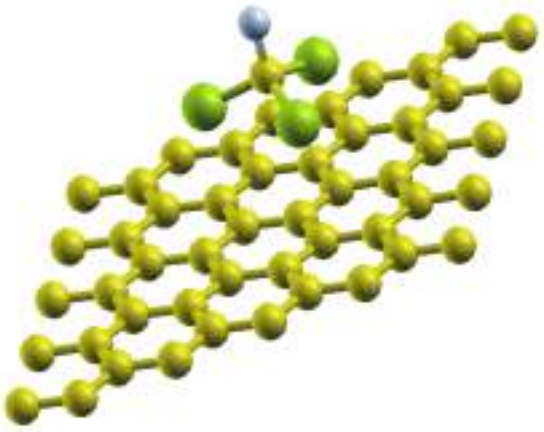

Figure 5.3: The optimized structure obtained after the adsorption of $CFCl_3$ over pristine graphene. Carbon, Chlorine, and Fluorine atoms represented with yellow, green, and blue color balls respectively.

in the bond length of the molecule. There was negligible charge transfer (0.034 e donated to layer by the molecule) between the molecule and sheet. Fig. 5.4 depicts variation in the electronic structure with the plot of density of states (DOS). The variation in DOS can be observed from -10 eV to 5 eV except near the fermi level. Since there are minor changes in the bond lengths, DOS, and charge transfer, it can be concluded that the $CFCL_3$ is weakly adsorbed over the sheet.

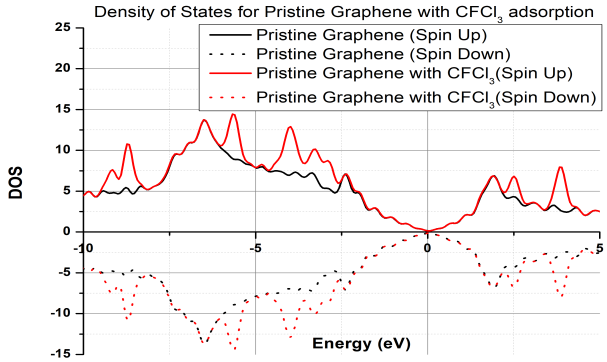

Figure 5.4: The density of states (arb. units) plot for pristine graphene before and after CCl_F3 adsorption with Fermi level shifted to zero.

5.3.2 CCl_2F_2 over Pristine Graphene

Before the adsorption studies, the CCl_2F_2 molecule was optimized first and the obtained bond-lengths were found to be in good agreement with the literature and database [214]. For the adsorption study, the molecule was oriented in seven different possible orientations over the graphene sheet and

the relaxed. After the relaxation of individual cases, it was observed that the CCl_2F_2 molecule prefers to adsorb in a fashion with two F atom and one Cl atom near the sheet represented in Fig.5.5 with an adsorption energy of -0.588 eV. The distance between the F atom and Cl atoms with the nearest carbon atoms were 2

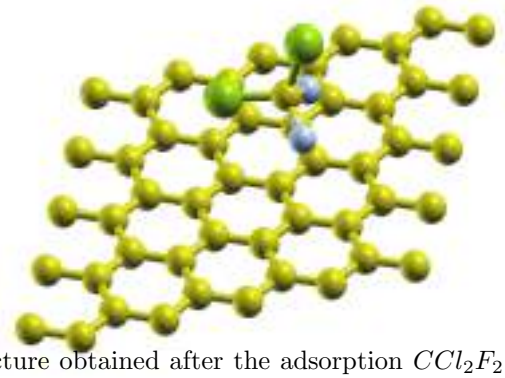

Figure 5.5: The optimized structure obtained after the adsorption CCl_2F_2 over pristine graphene. Carbon, Chlorine, and Fluorine atoms represented with yellow, green, and blue color balls respectively.

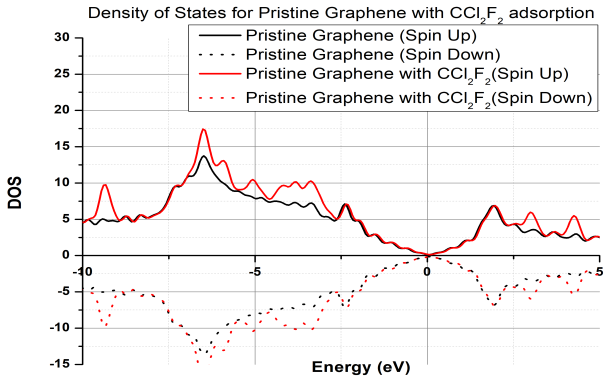

Figure 5.6: The density of states (arb. units) plot for pristine graphene before and after CCl_2F_2 adsorption with Fermi level shifted to zero.

There were insignificant changes in the bond length of the graphene sheet (Table 5.1). However, minuscule changes were observed in the bond lengths the molecule. There was a negligible charge transfer (0.044 e donated to layer by the molecule) between the molecule and sheet. Fig.5.6 represents the DOS potraying the change in the in the electronic structure. Again, it can be seen that the DOS changes from -10 eV to 5 eV except near the fermi level. Similar to the previous case, the changes in the bond lengths, DOS, and charge transfer are insignificant. Hence it can be concluded that the CCl_2F_2 is weakly adsorbed over the sheet.

5.3.3 $CClF_3$ over Pristine Graphene

Before the adsorption studies, the $CClF_3$ molecule was optimized first, and the obtained bond-lengths were found to be in good agreement with the literature and database [214]. For the adsorption study, the molecule was oriented in six different posssible orientations over the graphene sheet and the relaxed.

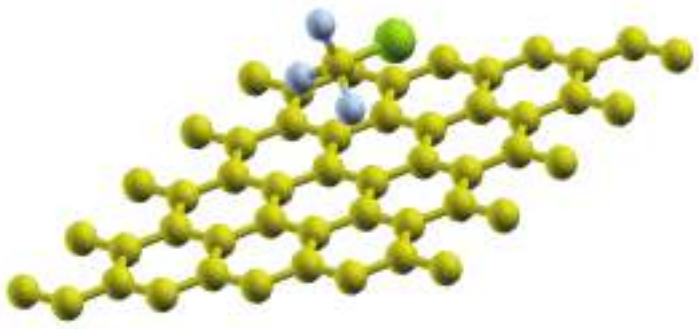

Figure 5.7: The optimized structure obtained after the adsorption of $CClF_3$ over pristine graphene. Carbon, Chlorine, and Fluorine atoms represented with yellow, green, and blue color balls respectively.

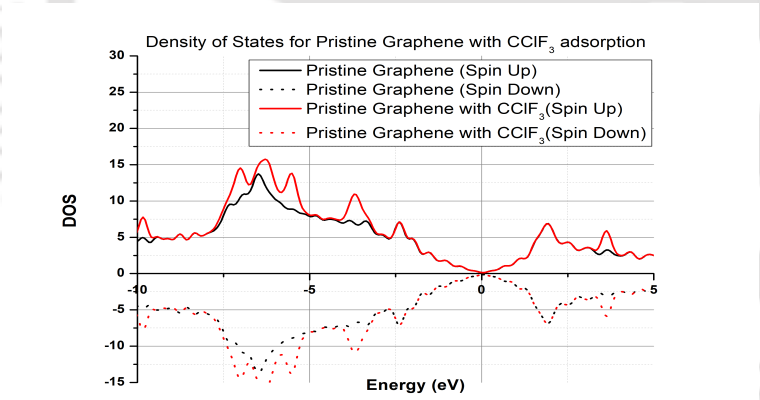

Figure 5.8: The density of states (arb. units) plot for pristine graphene before and after $CFCl_3$ adsorption with Fermi level shifted to zero.

After the relaxation of individual cases, it was observed that the $CClF_3$ molecule prefers to adsorb in a fashion with 2 F atoms and one Cl atom near the sheet as represented in Fig. 5.7 with an adsorption energy of -0.584 eV. The distance between Cl and F atom from sheets were 3.195$\mathring{A}$ and 2.807$\mathring{A}$. There were no significant changes in the bond length of the graphene sheet. However, there was a very negligible change in the bond length and bond angle of the molecule. There was minuscule charge transfer (0.042 e donated to layer by the molecule) between the molecule and sheet.

A DOS has been plotted to evaluate the electronic structure's change as shown in Fig.5.8. The

DOS changes in the -10 eV to -2.5 eV range, but no changes were observed at fermi level. Once again, the changes in the bond lengths, DOS, and charge transfer are insignificant. Hence it can be concluded that the $CClF_3$ is weakly adsorbed over the sheet.

Table 5.2: The comparison of bond-lengths, adsorption distance, and charge transfer for Ti-doped graphene and CFC molecules before and after the adsorption.

Gas		Substrate Bond Length (in Angstroms)		Gas Bond Lengths (in Angstroms)		Nearest Atoms	Distance(in Angstroms)	Charge Transfer
		C-C	C-Ti	C-Cl	C-F			
$CFCl_3$	Before Adsorption	1.418	1.925	1.774, 1.774, 1.774	1.351	–	–	–
	After Adsorption	1.420	1.965	1.921, 1.909, 1.747	1.323	C-Cl	2.521	0.285e
						C-Cl	2.535	
CCl_2F_2	Before Adsorption	1.418	1.925	1.773, 1.774	1.346, 1.346	–	–	–
	After Adsorption	1.419	1.945	1.850, 1.868	1.323, 1.321	C-Cl	2.56	0.361e
						C-Cl	2.579	
$CClF_3$	Before Adsorption	1.418	1.925	1.772	1.342, 1.343, 1.343	–	–	–
	After Adsorption	1.420	1.934	1.812	1.377, 1.316, 1.316	C-F	2.444	0.339
						C-Cl	2.596	

5.3.4 $CFCl_3$ over Ti-doped Graphene

Similar to the previous cases, the $CFCl_3$ gas molecule and Ti-doped Graphene sheet were optimized first, and the bond-lengths were in good agreement with the reported literature. After the individual optimizations, the molecule was oriented in six unique orientations, and then the relaxation was performed. The relaxed structures obtained from each of these were carefully analyzed and compared with the help of adsorption energies, structural changes, and change in the electronic structure. It was observed that the adsorption of the molecule is more favorable than that of pristine graphene.

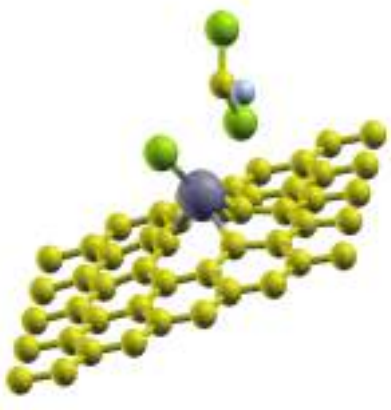

Figure 5.9: The optimized structure obtained after the dissociation of $CFCl_3$ over Ti-doped graphene. Carbon, Titanium, Chlorine, and Fluorine atoms represented with yellow, green, grey, and blue color balls respectively.

It is noticed that both Cl and F atoms of the $CFCl_3$ molecule interact with the Ti atom differently

when the molecule with one Cl and one F atom is introduced symmetrically over Ti atom ($4\mathring{A}$ away). As a result, the dissociation-like phenomenon or particularly the weakening of the C-Cl bond was observed. It led to increase in the bond length from $1.774\mathring{A}$ to $2.874\mathring{A}$. Finally, the adsorption of the Cl atom over the layer is found to be energetically favorable (Fig.5.9). The Cl-Ti bond length is $2.292\mathring{A}$, which is very close in this case. The change in the energy for this phenomenon is about 1.731 eV. Also, there was significant charge shared between Cl and Ti, but negligible charge shared between Cl and C, which again reflects the dissociation-like phenomena forming the CCl_2F molecule. The CCl_2F molecule weakly adsorbed over the layer through the small charge transfer/sharing between the Cl and Ti atoms.

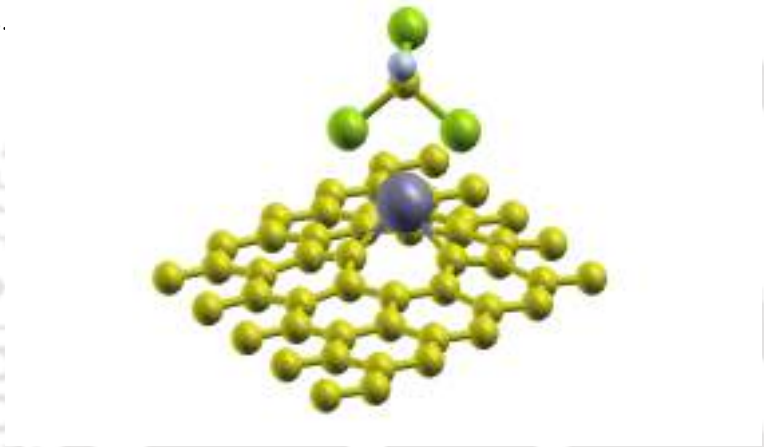

Figure 5.10: The optimized structure obtained after the adsorption of $CFCl_3$ over Ti-doped graphene. Carbon, Titanium, Chlorine, and Fluorine atoms represented with yellow, green, grey, and blue color balls respectively.

However, as compared with the previous orientation, when there are two Cl atom oriented symmeterically over the Ti atom, they both interact with the Ti atom in a similar manner. This balance the molecule over the layer, resulting in adsorption rather than dissociation like behaviour. Also, among all the other orientations, this one is the most favorable orientation for the adsorption with an adsorption energy of 1.7175 eV. The relaxed structure has those two Cl atoms near the layer with distances $2.521\mathring{A}$ and $2.535\mathring{A}$ respectively, from the Ti atom as shown in Fig.5.10.

Significant changes were observed in the bond lengths of the layer as well as the molecule after the adsorption as tabulated in Table 5.2. The C-Ti bond length is increased to $1.965\mathring{A}$ as compared to perviously found $1.925\mathring{A}$. Due to the interaction between Ti and Cl atoms, the C-Cl bond lengths were increased from $1.774\mathring{A}$ to $1.921\mathring{A}$ and $1.909\mathring{A}$, respectively, but for non interacting Cl atom, the change in the bond length was negligible. The DOS in Fig.5.11 depicts the change in the electronic structure. The shift in the DOS can be seen from -20 eV to 5 eV. The adsorption causes a significant

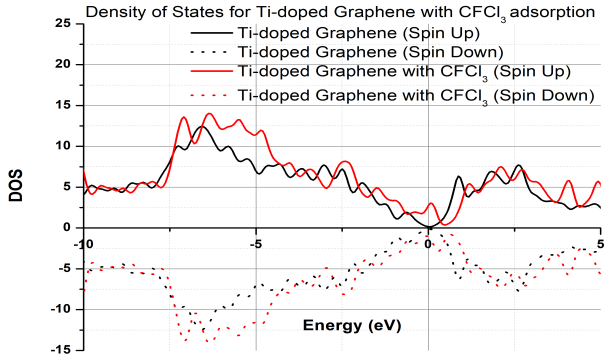

Figure 5.11: The density of states (arb. units) plot for Ti-doped graphene before and after $CFCl_3$ adsorption with Fermi level shifted to zero.

increase the DOS at the fermi level. It was estimated by charge analysis that a significant charge of 0.285e transferred to the layer signifying that $CFCl_3$ acts as a donor. All of these structural changes, DOS changes, and charge transfer prove that the molecule have strong chemisorption.

5.3.5 CCl_2F_2 over Ti-doped Graphene

Similar to the $CFCL_3$ case, the different orientations have been relaxed, and all of them result in adsorption except the one with 2 F atom and 1 Cl atom arranged symmetrically over Ti atom of the layer tends to dissociation-like phenomenon (Fig.5.12). In this case, the C-Cl bond of the gas gets weakened. The bond length increased from 1.77$\mathring{A}$ to 1.96$\mathring{A}$, the shared charge between them also gets reduced. This Cl atom comes closer to the Ti atom, and a small charge is shared between them. The distance between them is 2.438$\mathring{A}$ which is slighly more than the previous $CFCl_3$ case. Again the 2 Cl atom near the layer are most energetically favorable for the adsorption with an adsorption energy of 1.596 eV. The distance between those two Cl atoms and Ti atom are 2.579$\mathring{A}$ and 2.56$\mathring{A}$, respectively. The optimized geometry can be seen in Fig.5.13. After the adsorption, the bond lengths of the layer, as well as the molecule varied significantly as shown in Table 5.2. The C-Ti bond length gets increased to 1.945$\mathring{A}$ as compared to before 1.925$\mathring{A}$.

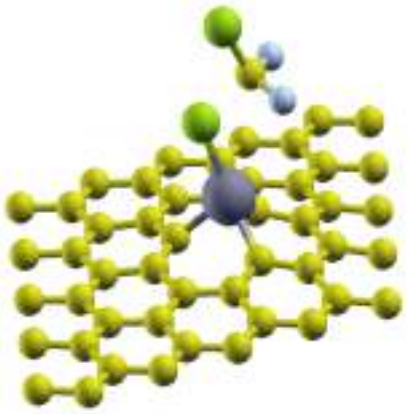

Figure 5.12: The optimized structure obtained after the dissociation of CCl_2F_2 over Ti-doped graphene. Carbon, Titanium, Chlorine, and Fluorine atoms represented with yellow, green, grey, and blue color balls respectively.

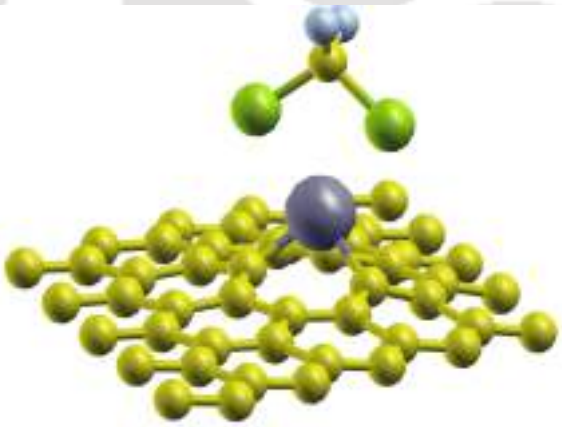

Figure 5.13: The optimized structure obtained after the adsorption of CCl_2F_2 over Ti-doped graphene. Carbon, Titanium, Chlorine, and Fluorine atoms represented with yellow, green, grey, and blue color balls respectively.

Due to the interaction between Ti and Cl atoms, the C-Cl bond lengths were increased from 1.774$\mathring{A}$ to 1.850$\mathring{A}$ and 1.868$\mathring{A}$. Since the F atoms are not directly interacting to the layer, the changes in the bond lengths were trivial. There was a charge transfer of 0.361e to the layer. The electronic struture change can be reckoned form the DOS plotted in Fig.5.14. The shift in the DOS can be seen from -20 eV to 5 eV. The adsorption caused a significant increase in the DOS at the fermi level. The evaluation of charge analysis reflected a significant transfer of 0.361e charge to the layer. This shows that CCl_2F_2 act as a donor. All of these structural changes, DOS changes, and charge transfer prove that the molecule has strong chemisorption.

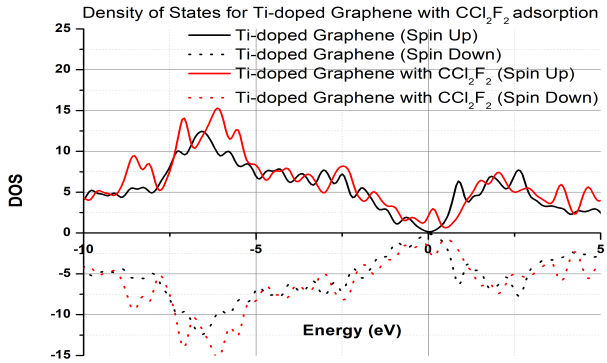

Figure 5.14: The density of states (arb. units) plot for Ti-doped graphene before and after CCl_2F_2 adsorption with Fermi level shifted to zero.

5.3.6 CClF3 over Ti-doped Graphene

Following the pattern of previous cases, the different orientations have been relaxed, and all of them result in adsorption. Here, the orientation with 1 Cl atom and 1F atom placed symmetrically near the layer results in the most energetically favorable for the adsorption, the adsorption energy is 1.309 eV. The distance between Cl atom, F atoms, and Ti atom are 2.596 and 2.444, respectively, as shown in Fig.5.15.

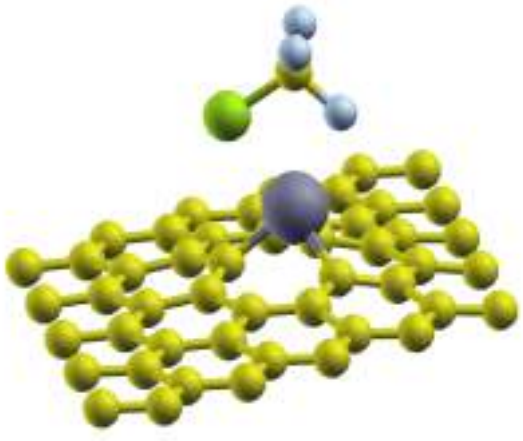

Figure 5.15: The optimized structure obtained after the adsorption of $CClF_3$ over Ti-doped graphene. Carbon, Titanium, Chlorine, and Fluorine atoms represented with yellow, green, grey, and blue color balls respectively

The changes in the bond lengths of the layer after the adsorption were in close correlation with the previous two cases. However, the changes in the bond length is considerable for the Cl and F atoms near the layer. Due to the interaction between these atoms and Ti atoms, the C-Cl bond lengths

were increased from 1.774 to 1.812, and C-F bond length increased from 1.342 to 1.388. Seeing that the F atoms are not directly interacting to the layer, the changes in the bond lengths were negligible. There was a charge transfer of 0.3639e to the layer. All of these structural changes and charge transfer prove that the molecule has strong chemisorption. A DOS has been plotted to observe the variation in the electronic structure (Fig.5.16). The shift in the DOS can be seen from -20 eV to 5 eV. Due to the adsorption, there was a significant increase in the DOS at the fermi level. The presented charge analysis reflected that a significant charge of 0.339e transferred to the layer; therefore, $CFCl_3$ acts as a donor. All of these structural changes, DOS changes, and charge transfer prove that the molecule has strong chemisorption.

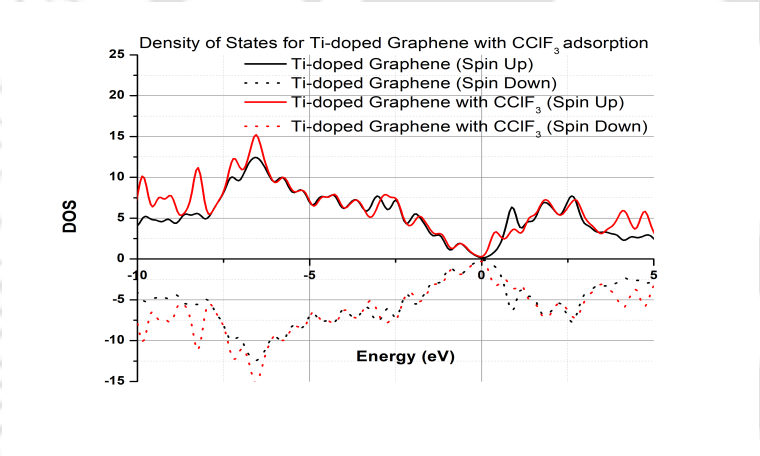

Figure 5.16: The density of states (arb. units) plot for Ti-doped graphene before and after $CClF_3$ adsorption with Fermi level shifted to zero.

5.4 Summary

Interactions of the CFC molecules over pristine and Ti-doped 2-D graphene sheets are explored in this paper. The mentioned CFC molecules get adsorbed through weak chemisorption as they have a small interaction with the pristine graphene sheet. This makes the charge transfer and variation in electronic properties negligible. However, their interaction with the Ti-doped graphene sheet is very strong. It was observed that the interaction between the Cl and Ti atoms is particularly significant. Due to this intense interaction, sometimes the C-Cl bond gets broken in $CFCl_3$ and CCl_2F_2 gases, forming a free-radical which gets adsorbed over the sheet while the Cl atoms form a strong bond with Ti-atom. This phenomenon is known as de-chlorination. Since the Ti-doped sheet causes de-chlorination, it may be used as a catalyst during gas reactions or conversions. However, de-chlorination

was not observed for $CClF_3$ due to high energy requirements [215]. Apart from the minor cases of splitting, strong chemisorption was observed, resulting in significant variations in electronic properties and large charge transfer. Finally, a thorough analysis of each case shows that a significant charge transfer to the layer is noticed for the case of $CFCl_3$. Therefore, it can be stated that the doped sheet has the highest sensitivity of molecular adsorption for $CFCl_3$. Our study concluded that the Ti-doped graphene could be a good candidate for detecting these CFC gases, and experimental efforts should be promoted in this direction.

6

Graphene Oxide and Functionalized Graphene Oxide based Devices for Label-Free Sensing of Glutathione

Contents

Outline Glutathione is a master antioxidant present in cells and tissues of the human and animal body. It is also a well-known cancer bio-marker. The elevated levels of it indicate cancer or tumor growth. In this work, the trench-based sensor devices fabricated through the optical lithography techniques with GO and antibody immobilized NH_2-GO as the channel materials were explored for Glutathione detection applications. The synthesized materials were thoroughly characterized and then drop casted between channel regions. These devices were electrically characterized upon exposure to varying concentrations of Glutathione molecules, and the changes in the current were examined. It was observed that the GO device is sensitive towards the Glutathione molecules but due to the lack of any bio-recognition element GO device suffered from selectivity aspects. Therefore, the antibody functionalized NH_2-GO devices were explored for Glutathione detection. The device exhibits an excellent sensitivity towards Glutathione molecules. The device possesses a fast response time which is less than 5 seconds. The device was also tested for selectivity, and the negligible current change with respect to other amino acids reflects that it is highly selective. The proposed device proves to have a better performance towards Glutathione sensing as compared to the reported literature, with some additional benefits of the trench during the pouring of analyte and estimation experiments. Therefore, it can be concluded that the proposed device has the potential to be used as a point-of-care sensing application.

6.1 Introduction

Glutathione (GSH) is a tri-peptide made of three amino acids glutamine, glycine, and cysteine. GSH is found in humans, plants, fungi, and even in bacterias. GSH prevents cellular damage of cells and tissues caused due to any stress such as reactive oxygen species (ROS), heavy metals, etc. [216]. In normal cells and tissues, it exists mostly in its reduced form of GSH along with some remaining oxidized form of GSSG. In its reduced form, the cysteine part acts as a reducing agent. On encountering any ROS, free radicals, or heavy metal, GSH tries to neutralize them and, in the process, converting itself to GSSG [217]. Therefore, the primary role of GSH is to act as an antioxidant in cells and the body. Other than that, it helps during the synthesis of various mediator molecules such as leukotrienes, prostaglandins and has an important role in the nitric oxide cycle and metabolism of xenobiotics [218].

GSH is also an important biomarker and is used for the diagnosis of malignant tumors in liver cancer. In the case of cancer or tumor growth, GSH and its enzyme Glutathione-S-Transferase were

found to be over-expressed [219]. Therefore, detection and estimation of GSH is not only important in ROS or heavy metal stress cases but even more crucial in the case of cancer and tumor growth. Because of such importance of GSH, a number of methods have been explored, such as optical, spectroscophotometric [220], high-performance liquid chromatography (HPLC) [221], nuclear magnetic resonance (NMR) [222]etc. However, these techniques are costly, time-consuming, and require specialized personnel. Some techniques like optical are a bit easy, but they suffer from optical interferences. The reported voltammetric methods also have poor selectivities and very weak responses. Therefore, the development of electrochemical biosensors is of paramount importance. The incorporation of biochemical assays in these devices helps to obtain selectivity aspects. The development of the VLSI fabrication process over the last few decades enables miniaturization of these biosensor devices. Hence, a cost-effective and point-of-care bio-sensor device can be achieved [223].

In this work, we explored a trench-based sensor device fabricated through the standard silicon fabrication processes such as optical lithography techniques. The sensor device with Graphene Oxide (GO) and antibody immobilized over Amine functionalized Graphene Oxide (NH_2-GO) as channel material were explored for Glutathione detection applications. It was observed that GSH molecules interact with oxygen-containing groups present over GO flakes. Therefore, good sensitivity sensing was observed. However, in the absence of any biochemical assay or any biorecognition element, the GO device suffered from selectivity issues. Hence, the incorporation of antibody-based sensing was encouraged. We explored the antibody immobilized over NH_2-GO channel device for the first time. The proposed device has excellent sensitivities and selectivities towards GSH molecules. Owing to the miniaturized structure, the requirement of analyte is significantly less, and so is the response time. The detailed synthesis and fabrication process of the sensor device is explored in the following sections.

6.2 Materials

Graphite powder was purachsed from Alfa Aesar. Other chemicals which are H_2SO_4, H_2O_2, APTES, $NaNO_3$, $KMnO_4$, EDC, and NHS were purchased from Sigma Aldrich and used without any further purification. The solvants such as Acetone, Iso-propanol, Ethanol were procured from Loba Chemie and Finar. The Glutathione antibodies were obatined from Thermo-Fisher.

6.3 Synthesis

6.3.1 Graphene Oxide Synthesis

Graphene oxide was synthesized by adopting Hummers method from various literature with some minor modifications [224]. The detailed procedure for the same are given as follows: the graphite powder (0.5 g) was mixed thoroughly with concentrated sulfuric acid (23 ml) in a 500 ml round bottom flask first with bath sonication and then with magnetic stirrer for 5-10 minutes till a homogenous mixture is obtained. The flask shifted to ice bath, and sodium nitrate ($NaNO_3$, 0.50 g) was added slowly under magetic stirring. After that, potassium permanganate ($KMnO_4$, 3 g) was added to the mixture in a extremely delicate and slow manner over the period of 3 h keeping the temperature maintained below 5 degrees Celsius for the whole duration. This process is vulnurable and can cause over oxidation at some local points, therefore, all these considerations are important. The temperature of the mixture slowly raised to room temperature (30-35 degrees Celsius) after the addition of $KMnO_4$ is over and kept under vigorous stirring for atleast 30 min. Now, DI water (46ml) added to the reaction mixture and as a result the temperture increased, and kept under stirring for 30 min more. Finally, the reaction quenched with adding more DI water (140ml) and H_2O_2 (10 % v/v, 10m) to the reaction. The mixture was filtered with vacuum filteration and obtained product was brownish yellow in color. In order to remove the Mn and Cl ions present in the resulting product, it was washed 5 times with dilute HCl (5% v/v, 200 ml) and then 3 times with lukewarm (65-70 degrees Celsius) DI water. The GO powder was obatined after drying overnight in oven at 50 degrees Celsius.

6.3.2 Amine functionalization of Graphene Oxide

The GO powder (100 mg) obatined from previous process was added to anhydrous ethanol (30 ml) and subjected to sonicated for 2 h inorder to obatin a uniform dispersion. The dispersion was transferred to a round bottom flask with vigorous magetic stirreringunder water bath at 70 degrees Celsius. Then, APTES (1 ml) was added drop-wise followed refluxing of mixture for 6 h. The obatined mixture at the end of the reaction was centrifuged at 10,000 rpm for 30 min followed by several washing and re-sonicating in anhydrous ethanol and centrifuge cycles to remove un reacted or residual APTES. The resultant product was dried over night in vacuum oven at 50 degrees Celsius. This amine functionalized GO powder was stored under vacuum for further use [225].

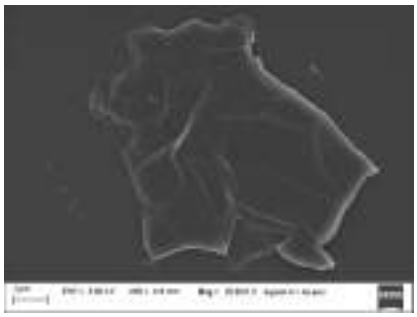

(a) Image at low magnification (25KX).

(b) Image at high magnification (35KX).

Figure 6.1: FESEM image for synthesized Graphene Oxide.

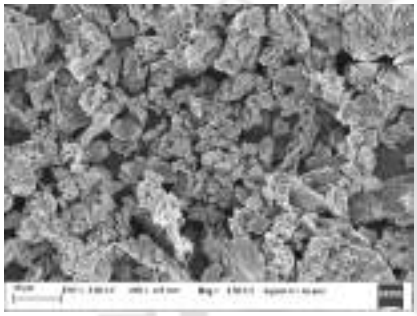

(a) Image at low magnification (3.5KX).

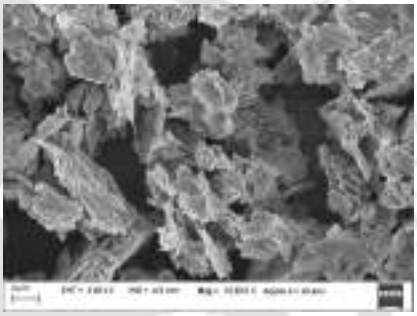

(b) Image at high magnification (10KX).

Figure 6.2: FESEM image for synthesized Amine functionalized Graphene Oxide.

6.4 Characterization

6.4.1 FESEM

The morphologies of synthesized GO and NH_2-GO were investigated with FESEM analysis and presented in Figure 6.1 and 6.2. The FESEM image for the synthesized GO at low and high magnifications is given in gure 6.1. The graphene oxide flakes can be observed. After performing the amine functionalization of the GO, the changes in the morphologies can be noticed from the Figure 6.2.

6.4.2 XRD

The crystallinity sturucture of the synthesized GO and NH_2-GO were probed through XRD analysis. The powder xrd for GO is given in Figure 6.3a, the sharp peak around 2 $\theta = 9.06$ corresponding to an interlayer distance of about 0.98 nm, which is larger than that of pristine graphite (0.33 nm), this proves the formation of GO. The increase in the interlayer disance of GO depicts the formation of funational groups such as carboxyl, hydroxyl during Hummers process. This increase in the interlayer

distance cause exfoliation of graphite powder in the hydration which ultimately result in formation of GO sheets [226]. However, XRD spectra in Firure 2b after the amination process shows that the peak around 11 degrees is not completely disappeared but a sharp peak around 5.76 degrees was observed which corresponds to an interlayer distance of 1.53 nm, this incease in the interlayer distance confirms the intercalation of APTES hence proves the amine functionalization of GO sheets [227].

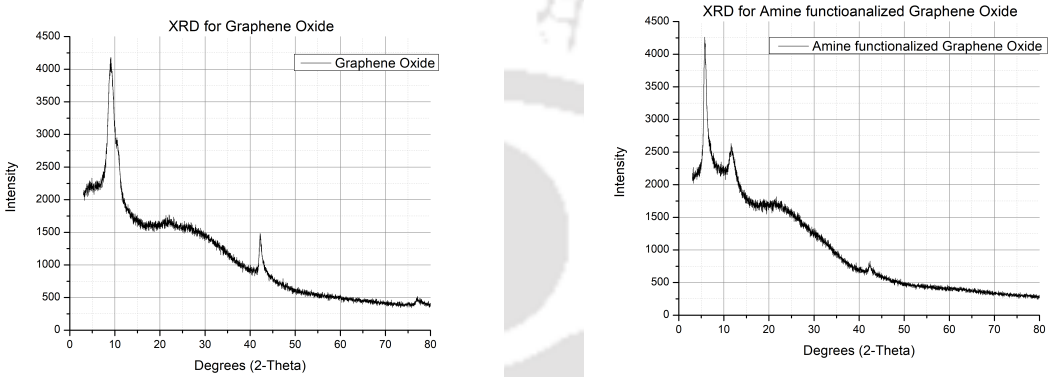

(a) XRD spectra of Graphene Oxide.

(b) XRD spectra of Amine functionalized Graphene Oxide.

Figure 6.3: Characterization Using XRD

FTIR

The functional groups formed in synthesized GO and Amine functionalized GO were characterized through FTIR spectra Figure 6.4.

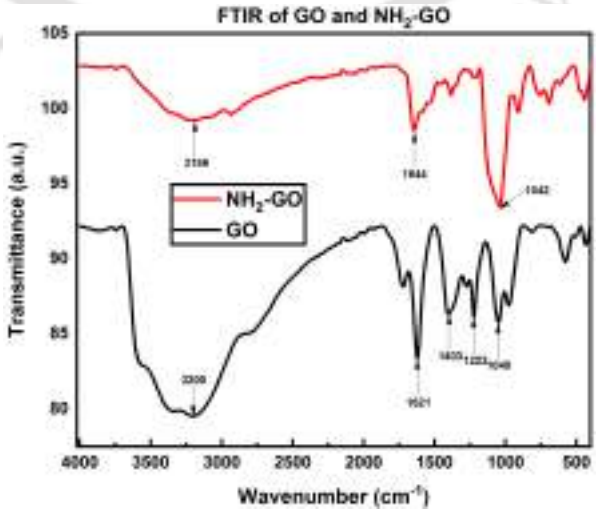

Figure 6.4: FTIR spectra of synthesized Graphene Oxide and Amine functionalized Graphene Oxide

The peaks observed at 1048, 1222, 1403, 1621, and 3200 are corresponds to CO-O-CO strectching, C-O vibration, O-H strectching , C=C vibration of graphene, and O-H strectching repectively. The FTIR spectra of NH_2-GO possessed peaks at 1042, 1644, and 3186 which are attributed to Si-O-Si strectching, C-NH-C stretching and O-H group repectively [228]- [229]- [230]. This confirms the amine functionalization of GO.

6.4.3 RAMAN

The synthesized GO and NH-GO were also characterized through widely used RAMAN spectroscopy. As shown in Figure 4a, GO exhibit its characteristics D peak at 1337 and G peak at 1593. In the case of NH_2-GO these bands shifts to 1338.5 and 1591.29 respectively, Figure-4b. The ratio of Id/Ig can indicate the disorders was decreased from 0.9676 to 1.0611, i.e., after the functionalization, the defects were present, which indicates the covalent functionalization of GO [230]- [231].

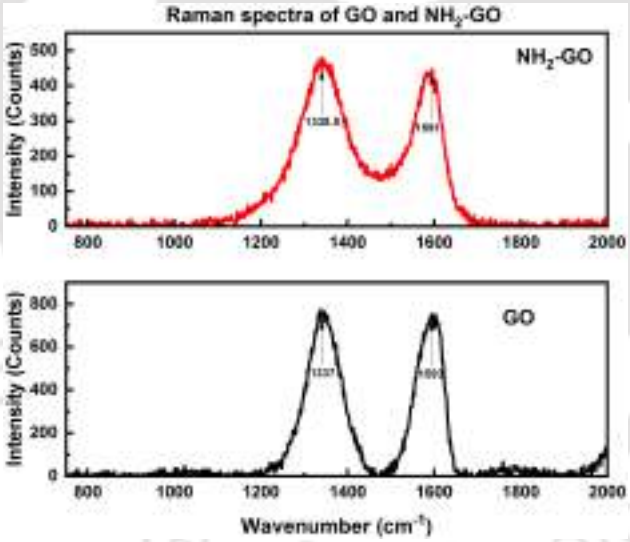

Figure 6.5: RAMAN spectra of synthesized Graphene Oxide and Amine functionalized Graphene Oxide

6.5 Sensor Fabrication

This section describes the detailed process flow for the sensor fabrication. The aim of the process flow is to fabricate a trench structure within two terminal chem-resistive over SiO2/Si wafer. This trench structure lies between the two electrodes with a reservior at one end. This type of structure is capable of accomodating the analyte liquid during the sensing experiments, and therefore, eliminating the need of external structures to achieve the same. Due to which, the complications fabrication process of the sensor fabrication reduced. Also, due to this intrinsic arrangement od trench within

sensor minimizes the leakage and electrode shorting issues. The fabrication was carried out employing standard silicon fabrication in class 100/1000 clean room, the process flow is described in the Figure 6.6 (image of the fabricated device can be seen in Fig. 6.7), the details of each step shown in Figure 6.6 can also be found in the Appendix A.1 and A.2.

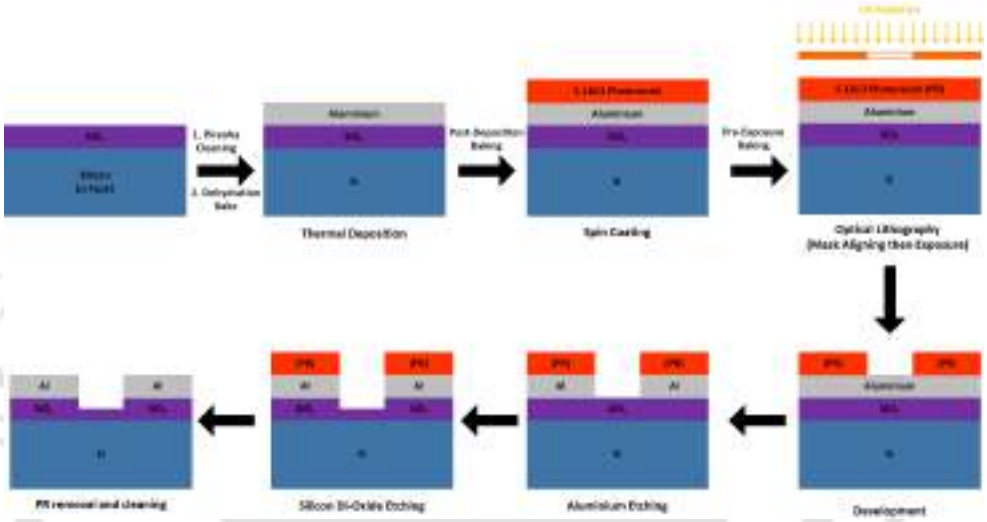

Figure 6.6: Process flow for sensing device fabrication.

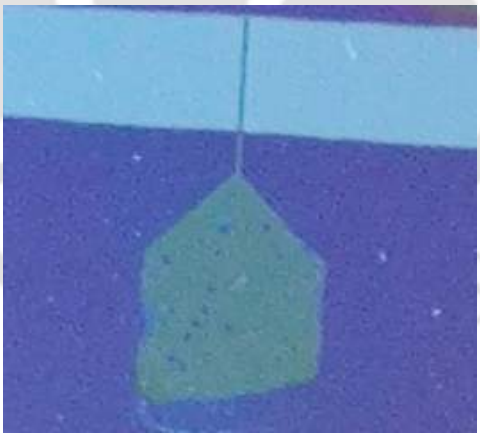

Figure 6.7: The optical image of the fabricated device for sensing application.

6.5.1 Antibody Immobilization

The antibody immobilization was performed over the functionalized graphene channel as per the carbaamide chemistry, the scheme is shown in Figure 6.8.

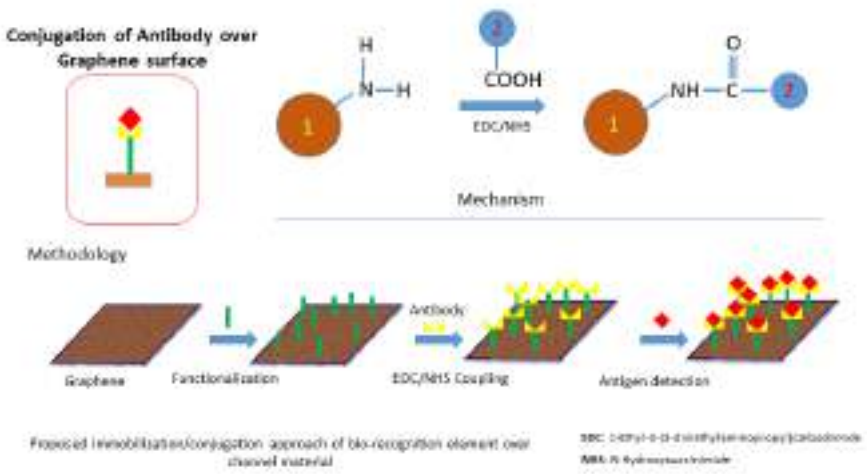

Figure 6.8: Scheme for Antibody immobilization over Amine functionalized Graphene Oxide.

The functionalized graphene was treated with EDC solution for 15 minutes at room temperature. After that, NHS solution was added to the same and left to react for 15 minutes at room temperature. In the end, the antibody solution was added to the mixture and let it bind overnight at 4 degrees Celcius.

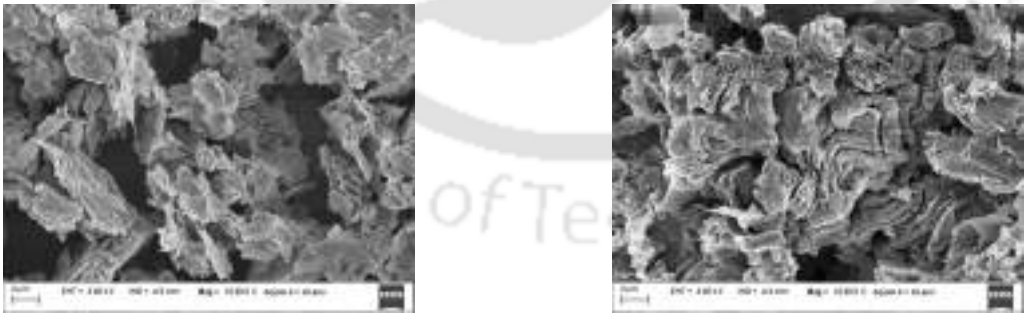

(a) FESEM image at low magnification. **(b)** FESEM image at high magnification.

Figure 6.9: FESEM image for synthesized Amine functionalized Graphene Oxide.

Once the binding process gets completed, the channel was gently washed with DI water 3-4 times to remove any unreacted chemicals and unbonded antibodies. The washed and dried device was stored at 4 degrees Celcius for further use. Once the immobilization process was completed, the FESEM images were taken to observe the morphological changes in the amine functionalized graphene. As

evident from the Figure 6.9, the morphological changes can be seen, proving the immobilization of antibodies over the amine functionalized graphene flakes. Further, these final devices (stored at 4 degrees Celcius) were then subjected to the sensing experiments.

6.6 Electrical Characterization

The interaction between GO and antibody immobilized NH_2-GO with Glutathione was investigated through electrical characterization with the fabricated devices having one of them as a channel material. The electrical characterization of these devices can reflect the utility of them as a sensor for Glutathione detection. The devices with GO and antibody immobilized NH_2-GO as channel were electrically probed Keithley 4200A-SCS Pulse Parameter Analyzer, and a thorough discussion is given as follows:

6.6.1 Graphene Oxide devices for Glutathione detection

The devices with GO as a channel were probed in chem-resistive or two-terminal fashion. The voltage sweep results of the same in the range of 0-4 Volt are given in Figure 6.11.

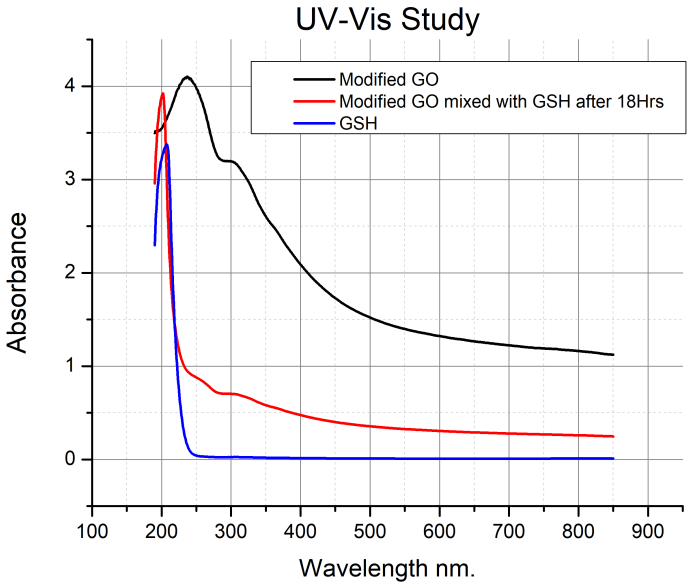

Figure 6.10: UV-Vis spectoscopy of GO before and after GSH treatment.

The characteristics in the Figure show typical diode-like characteristics, which arise due to the Schottky type barrier between GO layers and Aluminium contacts. Moreover, in order to explore the

interaction between Glutathione and GO, the solution of Glutathione was poured into the fabricated reservoir, which flows it to the channel. The Glutahione molecules get adsorbed over the GO flakes, and the interaction between these molecules and the oxygen containing groups commenced, the consequence of the same is reflected in decrement of the current as of the concentration of the Glutathione increased. The interaction between the Glutathione molecule and GO flakes is also examined through UV-Vis spectroscopy, as shown in Figure 6.10. The most prominent peak of the GO flakes is obtained near 230 nm, which attributes to π - π^* transition corresponding to aromatic C=C bonds of GO. However, a shoulder around 300nm is also present, which is due to the n-π * transition present in the C=O bonds of the oxygen-containing groups. This shoulder peak is diminished and tends to disappear after treatment with Glutathione. This clearly proves the strong interaction between the Glutathione molecule and GO flakes. The molecules get adsorbed and start altering the oxygen-containing groups which ultimately tends to remove them. Because of such interaction, the decrement in the current was observed during the electrical characterization. Therefore, it can be concluded that GO devices can act as Glutathione detection. However, these devices suffered from selectivity issues. Therefore, the biorecognition element is required over GO flakes. Hence, the antibody functionalized NH_2-GO device is needed.

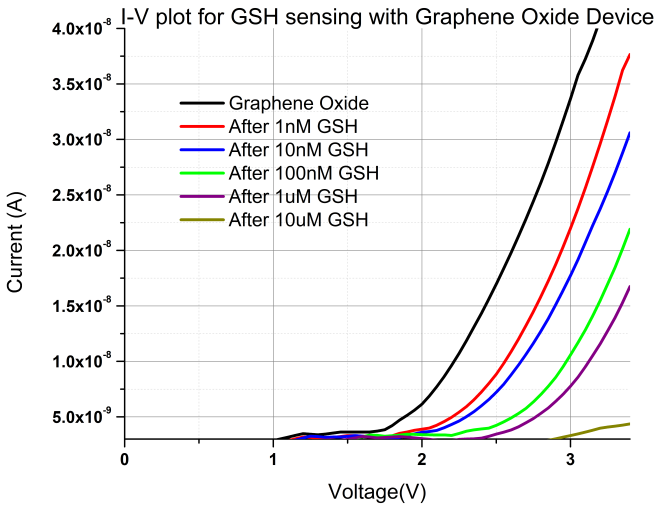

Figure 6.11: DC characterization of GSH sensing over Graphene Oxide chemiresistor sensing device.

6.6.2 Antibody immobilized NH_2-GO device for Glutathione detection

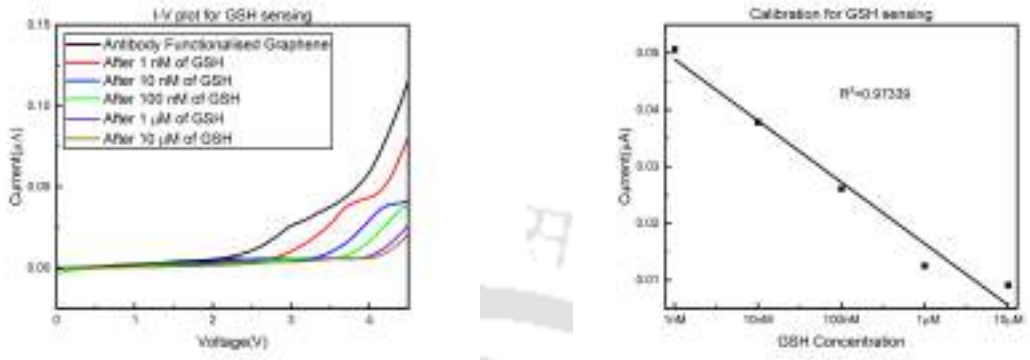

(a) I-V characteristics. **(b)** Calibration Curve.

Figure 6.12: DC characterization of GSH sensing over Antibody immobilized over Amine functionalized Graphene Oxide chemiresistor sensing device.

The devices with Antibody immobilized NH_2-GO as channel was again probed in chem-resistive or two-terminal fashion, the voltage sweep results of the same in the range of 0-4 Volt are given in Figure 6.12. The characteristics in Figure 6.12(a) are very similar to that of the GO device i.e., typical diode like characteristics, which once again arises due to the Schottky type barrier between NH_2-GO layers and Aluminium contacts. As the channel material has antibodies immobilized over them. Therefore, on exposure with Glutathione molecules (antigen to the antibodies), the antigen-antibody binding takes place, which results in a decrement in the current. On successive increments in the concentration of Glutathione added to the channel, the current levels keep on decreasing. The figure shows the calibration curve of current with respect to the concentration of Glutathione. It can be seen from Figure 6.12(b) that the device has a wide linear measurement range which is from 1nM to 10uM with a sensitivity of 10 nA/nM. The device has an extemely low limit of detection (LOD) of 100pM. In order to observe the real-time response of the sensor device, the device was subjected to transient electrical characterization, and the result is given in Figure 6.13. The device was biased at 4.2 V, and the current values were plotted with respect to time. The Figure shows the change in the current upon varying concentration of Glutathione in the channel region. Also, the response time of the device can be estimated from the transient response plot, which in this case is below 5 sec.

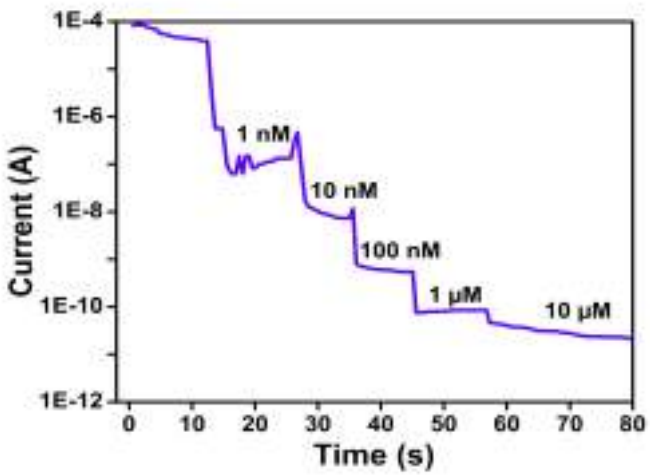

Figure 6.13: Transient characterization of GSH sensing over Antibody immobilized over Amine functionalized Graphene Oxide.

Finally, the selectivity aspect of the device with respect to various amino acids is investigated and shown in Figure 6.14.

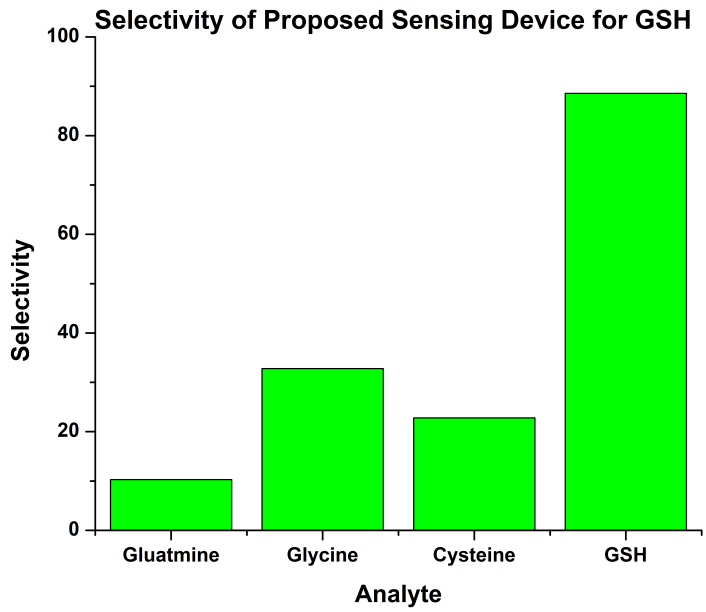

Figure 6.14: Selectivity of the proposed device for GSH over other amino acids.

Table 6.1: Comparison of proposed sensing device with various others.

Detection method	Material	Sensitivity	Range	LOD	Sample Volume	Time	Ref.
Cyclic Voltammetry	Multi-walled carbon nano-tubes	4.8 x 105 cm3/M	0.3-3350 uM	80 nM	-	-	[232]
Cyclic Voltammetry	Carbon nanotube screen-printed electrode	0.64 nA/uM	10-60 uM	3uM	50 uL	-	[233]
Differential pulse Voltammetry	thymine-rich DNA-gated switch functionalized mesoporous silica nanoparticles	96 nA/uM	1 nM- 1 uM	0.6 nM	50uL	20 min	[234]
Square wave Voltammetry	DNA-modified gold electrode	0.76 uA/uM	0.5 nM -5 uM	0.14 nM	-	20 min	[235]
cyclic Voltammetry	Poly-m-aminophenol deposited Glassy carbon electrode	84.2 nA/uM	0.1-5uM	0.095 uM	-	-	[236]
Chem-resistive	Antibody immobilized over amine graphene oxide	10 nA/nM	1nM - 10 uM	100 pM	1uL	5sec	This work

From Figure 6.14, it can be concluded that the device is highly selective towards the Glutathione molecules, and there is very minimal change in the current on exposure to other amino acids. In the end, the performance parameters of the proposed device are compared with the literature. From Table 6.1, it can be concluded that the proposed device has better sensitivity, selectivity, and response time as compared to the reported literature. Also, it has a significantly less sample requirement, which is 1uL. The proposed device was tested for stability. The devices stored at 4 degrees Celcius were found to be stable for around 30 days.

6.7 Conclusion

In this work, the trench-based sensor devices fabricated through the optical lithography techniques with GO and antibody immobilized NH_2-GO as channel material were explored for Glutathione detection applications. The synthesized materials were thoroughly characterized with FESEM, XRD, FTIR, and RAMAN spectroscopy. The synthesized materials were drop casted between channel regions, and the devices were electrically characterized. The channel region of the device was subjected to varying concentrations of Glutathione molecules and the changes in the current were examined. It was observed that the GO device (without any bio-recognition element) is sensitive towards the Glutathione molecules and, therefore, can act as a detection for the same. However, due to the lack of any bio-recognition element GO device suffered from selectivity aspects. Therefore, the antibody functionalized NH_2-GO devices were explored for Glutathione detection. The device exhibits an excellent sensitivity towards Glutathione molecules. Also, the transient response shows that the device has a fast response time which is less than 5 seconds. The device also possesses high selectivity towards the same, which is evident from negligible current change with respect to other amino acids.

Our sensing device proves to have a better performance towards Glutathione sensing as compared to the reported literature with some additional benefits of the trench during pouring of analyte and estimation experiments. Therefore, it can be concluded that the proposed device has the potential to be used as a point of care sensing application.

7

Label-Free Electrochemical Sensing of Lactate with Sulfur Doped Polyaniline Electrodes Immobilized with Lactate Dehydrogenase

Contents

Outline This work explores sulfur-doped polyaniline (PANI) coated ITO-PET electrodes for lactate detection applications. A simple and cost-effective deposition of doped PANI coating over ITO-PET was demonstrated through chrono-amperometry. The thickness of films was optimized through deposition time. The films were carefully analyzed and characterized through FESEM and AFM. The obtained films were smooth and had good adhesion with the ITO layer, because of which the electrodes have better stability in liquids. A sensor is developed based on the Lactate dehydrogenase (LDH) enzymatic actions on lactate. The LDH is negatively charged, whereas the PANI surface is positively charged; therefore, a drop-casted and incubation approach was employed for the immobilization of LDH over the PANI-ITO electrodes. The sensing experiments were performed with cyclic voltammetry to determine sensor performances and dynamic ranges. Our results indicate that the sensitivity, range of detection, and detection limit of the sensor improved signifi- cantly using Chrono-amperometry deposited sulfur-doped PANI electrode. The calibration plot was linear ($r^2 = 0.96839$) over the range of 1 to 100 nM. Further, a detection limit of 10 pM was observed with a sensitivity of 95.6 A/nM, which is higher than the reported literature. Therefore, the proposed sulfur-doped PANI- ITO electrodes can be used for lactate sensing for point of care applications.

7.1 Introduction

Lactate is the conjugate base of Lactic acid, produced from deprotonation of the carboxy group. It can be found in both bacterial and human metabolism [237]. Pure lactate can be produced from E.coli and other Lactic acid bacteria, which can be used in many food-processing industries [238]. Lactate level in the food is also an indicator of freshness, storage quality, and shelf life of the food items [239]. In the human body, lactate is a key fuel/by-product of anaerobic metabolism. The normal concentration of lactate in blood is 1-2mM/L but can increase up to 25mM/L during intense exercise. Without timely removal of such high concentrations through the liver and kidney, the condition of lactic acidosis can arise [240]. During intense physical activities, when the need for energy is sufficiently high, lactate is produced from pyruvate at a rate that is higher than its rate of removal, leading to its increased concentration in the body. The increase in lactate level can also disrupt the pH balance of the body, which may cause fatigue and metabolic disorder. Therefore, the estimation and monitoring of blood lactate levels are crucial in sports medicine and tracking fitness tracking [241]. The elevated levels of lactate also indicate several critical conditions such as Sepsis, Septic Shock, Haemorrhagic

Shock, Cardiac Arrest, Trauma, and Seizure [242]. Hence, the importance of estimating blood lactate levels is paramount for critically ill patients [239]. Moreover, the high concentration of lactate is also a sign of hypoxia, which can damage the brain, liver, and heart, and its severity may lead to death [243]. In recent literature reports, a clinical study has been conducted on Covid-19 patients, considering lactate as the detector of hypoxia. It was observed during the study that the chances of infection rose with the higher lactate levels [244]. Therefore, it can be concluded that the detection and estimation of lactate levels are vital not only for various industries but also for pathology and medicine. Colorimetric tests, high-performance liquid chromatography (HPLC), magnetic resonance spectroscopy, fluorimetry, chemiluminescence are the most common technique for lactate detection [240]. However, these techniques are time-consuming and costly as it involves pre-treatment of samples, high-end equipment, and require trained personnel for handling. Electrochemical biosensors can be the possible remedy for such problems, which can produce a real-time response, needless pre-treatment, low cost, and easy to handle with efficient detection. Electrochemical biosensors are mainly two or three-electrode systems placed in an electrochemical cell. Recently, several conducting materials have been unexplored as working electrodes in electrochemical biosensors, such as gold nanoparticles (Au), Graphene and its derivatives, electrically conducting polymers (CPs), and carbon nanotubes (CNTs). Among these electrode materials, conducting polymers gained huge attention from the scientific community due to their special π-orbital structure, which raises their sensitivity towards chain formation alterations [245]. Conducting polymers are basically organic material with high conductivity, exhibits redox action, have high electron affinity, and can be doped in p or n-type by oxidation and reduction of the special -electron, respectively. Such properties make them suitable for sensing applications [246]. Polyaniline (PANI) is one of the most attractive conducting polymers, which has been used in many types of electrochemical biosensors due to its environmental stability, easy synthesis process than other conducting polymers, low cost, high conductivity, and tuneable electrical properties [246]- [247]. Also, PANI is the only conducting polymer stable in air. Amine rich chemical skeleton of PANI makes it most suitable for biosensors, as it is highly useful in immobilizing various types of biomolecules. Its redox properties make it attractive for enzymatic biosensors due to the significant charge transfer between enzyme and polymer. Additionally, independent charge transfer of PANI reduces the requirement of an external mediator [247]. Over the last decades, PANI-based materials have been used as the electrode for lactate sensing [248]- [249]. Chaubey et al. used

PANI electrodes immobilized with two enzymes, LOD, and LDH for lactate detection [248]- [250]. In comparison, Rahman et al. and Cheng et al. used co-immobilization of LDH and NAD+ on the PANI composites [251]- [252]. PANI composites are also very attractive electrode materials nowadays for lactate detection [253]- [249]. In the literature, PANI electrodes used are of pure form, mainly synthesized in HCl, and do not possess any kind of molecular doping. Although the electrode materials and enzymes may vary, the bio-chemical assay involved is the same for all. In this work, for the first time, a sulfur-doped PANI electrode immobilized only with LDH is used for the detection of lactate levels. PANI electrode is synthesized in H_2SO_4 to generate sulfur-doped PANI for better conductivity and higher sensitivity. Morphological and chemical characteristics of PANI electrodes are determined. In addition, the performance of the sensor in terms of stability of electrode, sensitivity, linear range is determined. Our results proved that the doped PANI electrodes immobilized with LDH possess improved sensing capabilities towards lactate. Also, they are easy to fabricate and require only one enzyme rather than previously reported co-immobilization of two enzymes or involve complex composite electrodes. Hence, they can be used as lactate sensing at point of care applications.

7.2 Materials and Characterization Equipments

LDH, sodium Lactate, and all the other chemicals are purchased from Sigma-Aldrich and used without further purification. FESEM images were performed from JEOL FESEM Model: JSM-7610F. AFM images were taken from Innova SPM machine in tapping mode. FTIR spectra obtained from PerkinElmer, Singapore, Model: Spectrum two. The cyclic voltammetry were performed on Gamry 600+ potentiostate.

7.3 PANI Deposition over ITO-PET

The PANI can be obtained from PANI dispersion drop-casted over ITO-PET. However, drop-casted coatings have high resistance and have adhesion issues. Various treatments of the ITO-PET surface, such as plasma treatment and silanization are also explored. But, the improvement was substantial. Mixing the PANI powder along with the binder is having better stability, but sometimes random aggregation was observed. Therefore the possible remedies are polymerization of PANI over ITO-PET and electrochemical deposition of PANI. For the former case, the obtained films were quite stable, but the polymerization is time-consuming. Whereas, in the latter case of electrochemical

deposition, the obtained films are quite stable, and the process only takes 15-20 min. There are various ways to deposit PANI using an electrochemical setup. Among them, Cyclic Voltammetry and Chrono-amperometry methods are the simplest. For cyclic voltammetry deposition, the obtained films were very thin, and several cycles were required to obtain sufficient thickness. Whereas Chrono-amperometry deposition is quick, and deposited films are of good quality. In Chrono-amperometry

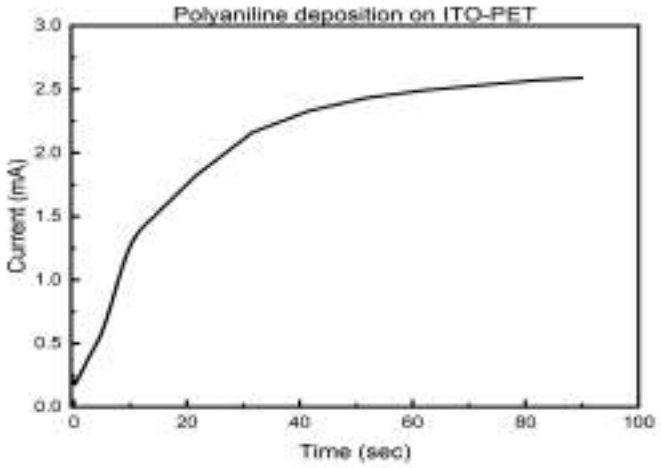

Figure 7.1: Polyaline deposition over ITO-PET using Chrono-Amperommetry.

deposition, the deposition was performed for 60 and 90 sec, at a constant voltage of 2V, as shown in Fig. 7.1, the increase in the current shows the deposition process at the ITO. The electrode used for both the methods were: Ag/AgCl ref electrode, Pt counter electrode, and ITO coated PET as working electrodes. Before, the deposition, the ITO-PET sheets were cleaned in ethanol and DI water followed by nitrogen stream drying. The solution for both methods was Aniline (0.1M) in H_2SO_4 (0.25M) solution. The synthesized electrodes were cleaned in dilute H_2SO_4, followed by a rinse in DI water to remove any oligomers, and finally, dried overnight at room temperature.

7.3.1 LDH Immobilization over PANI Coated ITO-PET

The fabricated electrodes were cleaned with N_2 gas stream to remove any dust particles. The 10uL of LDH enzyme were drop-casted over 1 cm^2 area of PANI-ITO electrodes and incubated at 4 degrees celcius for 4-6 Hours. LDH is negatively charged, whereas, PANI surface is positively charged, therefore, an electrostic coupling can occur between them which result in binding of LDH over PANI. The incubated electrodes are immersed in PBS 0.1M solution and DI water to remove any un-attached enzyme. Finally, these electrodes were placed in an electrochemical cell for lactate

detection experiments.

7.4 Characterization

7.4.1 FESEM

The morphological characteristics of the PANI films were studied through FESEM images. From Fig.7.2a and Fig.7.2b, fibrous structure can be seen for Chrono-amperometry polymerization, performed for 60 sec. The nano-fibers in the fibrous structure have a diameter within the range of 65-100 nm and have a smooth surface, which can be seen in Fig.7.2c. The nano-fibers are well connected and scattered irregularly, making porous nature as reported in [254]. This crystalline nano-fiber structure raises the conductivity of the polymer, as the carriers can be transported by hopping.

Fig. 7.2d. shows the granular formation of PANI for 90-sec polymerization deposition by the Chrono-amperometry method. The heterogeneous growth morphology depends on the applied voltage and the time of polymerization reaction [255]. As the time duration of polymerization increased, the porous of fibrous structure became filled, and a dense pact, thick and uniform granular structure arises. After immobilization of LDH over PANI electrode made by Chrono-amperometry deposition for 60 sec.

The flake-like structure on the fibrous structure of PANI films can be seen in Fig.7.2d and Fig.7.2e. These new flake-like structures are absent in the previous PANI electrode FESEM image, which proves the immobilization of the LDH enzyme on the PANI electrode. The randomly scattered flakes of LDH indicate the higher concentration of immobilized LDH enzyme.

7.4.2 FTIR

FTIR spectra of PANI thin film are shown in Fig.7.3. The peak at 1566 and 1486 cm^{-1} represented the C=C stretching vibration of the quinonoid and benzenoid ring [256]. Characteristic peaks at 1297 and 1230 cm^{-1} attributed to C-N stretching vibration of secondary aromatic amine [257], stretching and bending vibration of C-C bond [258], respectively; this indicates the amine backbone of PANI. The asymmetric vibration of SO_3^- in H_2SO_4 corresponds to the peak at 1084 cm^{-1} [258], which proves the sulfur doping in PANI thin film. The peaks at 1009, 800, 713 cm^{-1} represent the in-plane bending [6], out-plane bending vibration of one, 4- ring, and out-plane bending vibration of 1, 2- ring of C-H bond [256].

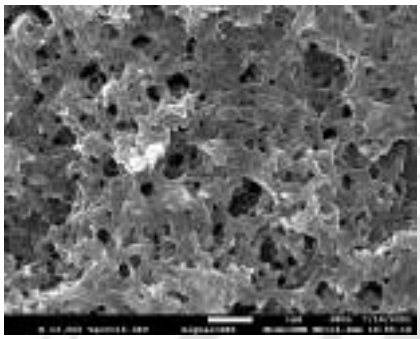

(a) FESEM image of PANI film deposited over ITO-PET using Chrono-Amperommetr for 60sec.

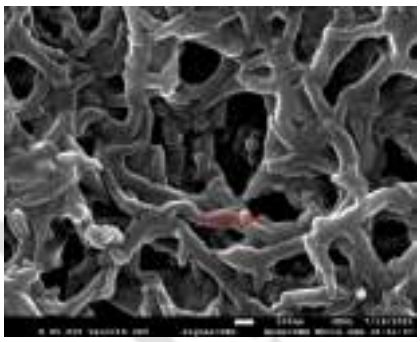

(b) Fiberous structure in PANI film deposited for 60sec.

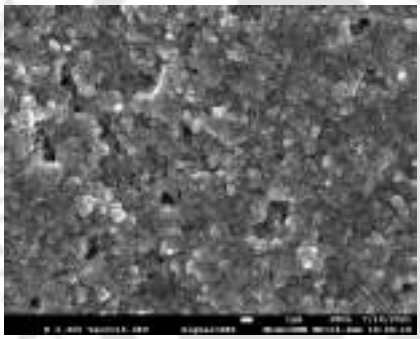

(c) Densely packed structures for 90 sec deposition.

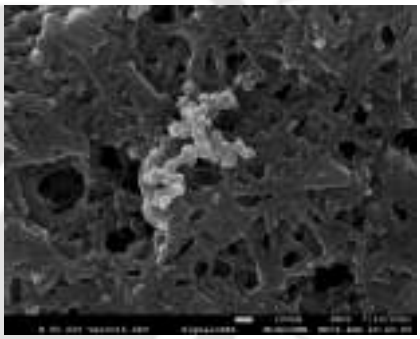

(d) Flake like structures after LDH immoblilization.

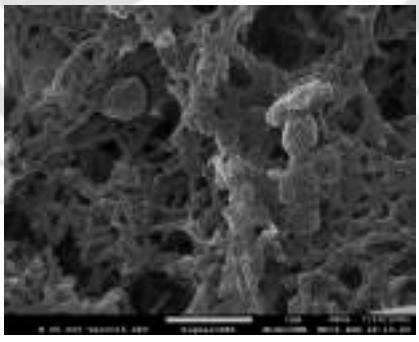

(e) Change in the morphology of PANI Films after LDH immobilization.

Figure 7.2: FESM

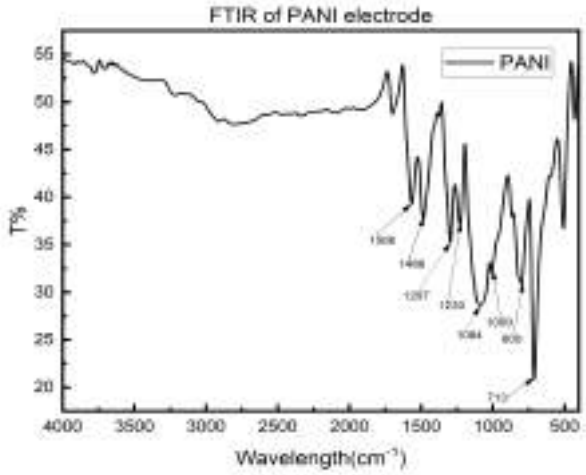

Figure 7.3: FTIR spectra for PANI deposited over ITO-PET.

7.4.3 AFM

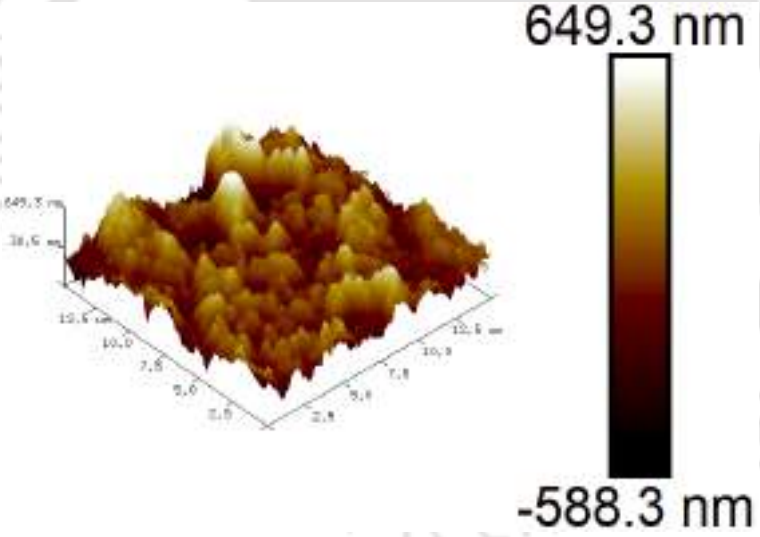

Figure 7.4: 3-D AFM image for PANI film deposited for 60sec.

The topography of PANI films over ITO-PET was investigated through tapping mode AFM. The 3-D AFM image for the films deposited for 60 sec are given in Fig. 7.4; the deposited film forms hills and valley-like morphology and has roughness below 150nm. Whereas the films deposited for 90 sec have similar morphology Fig. 7.5, but the roughness is increased from 150 to around 200nm. The AFM images again prove the thin and denser packing of PANI in 60-sec and 90-sec deposition, respectively.

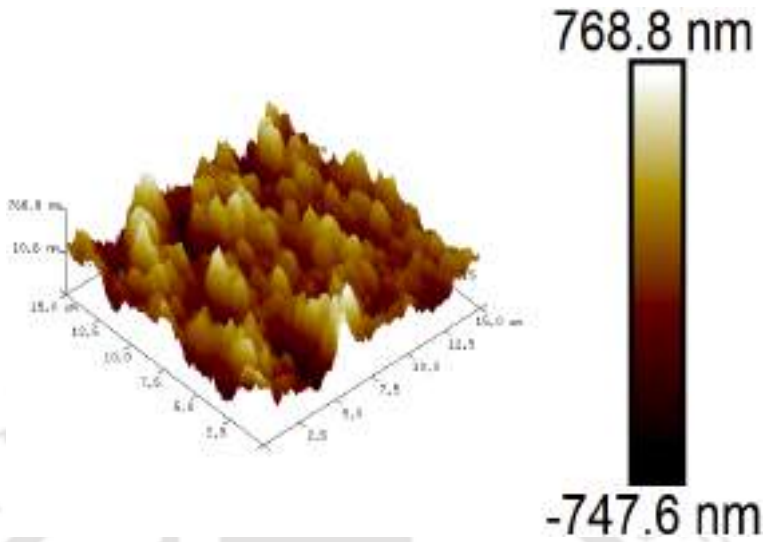

Figure 7.5: 3-D AFM image for PANI film deposited for 90sec.

7.5 Lactate Detection

The fabricated PANI-ITO electrodes were used as a working electrode in cyclic voltammetry, with Ag/AgCl as a reference and platinum wire as a counter electrode; PBS 0.1M was used as conducting electrolyte in the electrochemical cell. The cyclic voltammetry was performed in the -3V to 0V range with a scan rate of 100 mV/sec. The electrochemical activity of PANI-ITO electrodes tends to decrease as the pH increases; therefore, neutral pH (pH=7) was selected for the study. The electrodes are stable till a few no of the cycle enough to conduct and complete the measurement as shown in Fig.7.6.

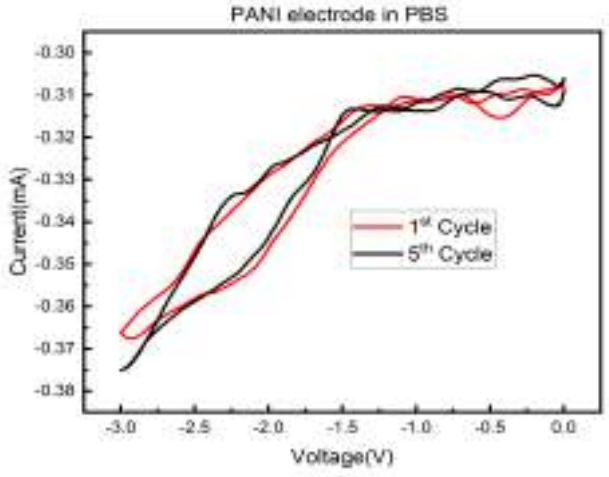

Figure 7.6: cyclic voltammogram of PANI-ITO electrodes in PBS.

Also, PBS buffer tends to decrease the current. Before the measurement of lactate, the LDH enzyme/protein was incubated over the electrode for 4-6 hours at 4 degrees Celsius. The cyclic voltammogram of the incubated electrodes (PANI/LDH electrode) in 0.1M PBS with the scan rate of 100mV/sec is shown in Fig. 7.7. The reduction peak was observed to be at -2.1 V. From the curve, it can be deduced that in the reduction cycle, there is a large charge transfer. This CV of PANI/LDH electrode was repeated many times with the same electrode and with other PANI/LDH electrodes. For the same electrode, the change in current levels is negligible, which proves the stability of the PANI/LDH electrode. Nevertheless, there can be significant variations in current levels for different electrodes, although the nature of the curve remains the same. This is because of the difference in the number of immobilized LDH on the PANI surface of the different electrodes.

Table 7.1: cyclic voltammogram of PANI-LDH electrodes.

Electrode	Principle	Limit of Detection	Linear Range	Sensitivity	Ref.
PANI/LOD-LDH	Amperometric	50 uM	0.1-1mM	38.5 uA/mM	[248]
pTTCA/MWNT/ LDH/NAD+	Amperometric	1 uM	5-90 uM	0.0106 uA/uM	[251]
LDH/Au-EVIMC-TiNTs-PANI/ITO	Amperometric	0.165 uM	0.55-5.55 uM and 5.55-3.33 uM	-	[252]
TiONT-PANI-GNP/ LDH/NAD+/ITO	Photo-electrochemical	0.15 uM	0.5-210 uM	0.0401 uA/uM	[249]
PANI-LDH	Cyclic Voltammetry	10 pM	1-100 nM	95.6 uA/nM	Present Work

The sensing experiment is done in 0.1M PBS with 100 mV/sec scan rate. For the detection of lactate, the LDH assay was followed. Lactate is added to the electrolyte (0.1M PBS) at the start of each experiment. As the lactate introduced in the electrolyte, it gets oxidized to pyruvate, and the reduction occurred at electrodes. From Fig.7.8, it can be noticed that as the concentration of lactate increased, the CV curve shift upwards. This is due to the increase of lactate concentration, leading to an increase in the reaction, which causes the electron transfer. Also as evident from previous figures,the reduction peak arises near -2V, therefore, the data for calibration for sensing lactate is collected at -2V of the reduction cycle and presented in Fig. 7.9. In order to ensure the reproducibility, three batches of electrodes were fabricated and tested separately, the obatined sensitivities were comparable. Fig. 7.9 represents the calibration curve for the lactate sensing with PANI/LDH electrode. The linear detection range can be shown from the curve with R^2=0.96839 for the 1-100nM range. Although the

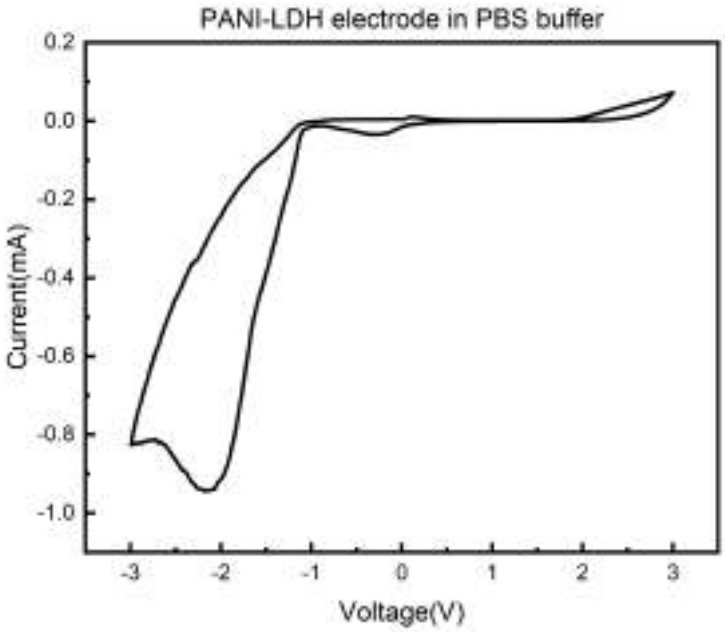

Figure 7.7: Cyclic voltammogram of PANI-LDH electrodes.

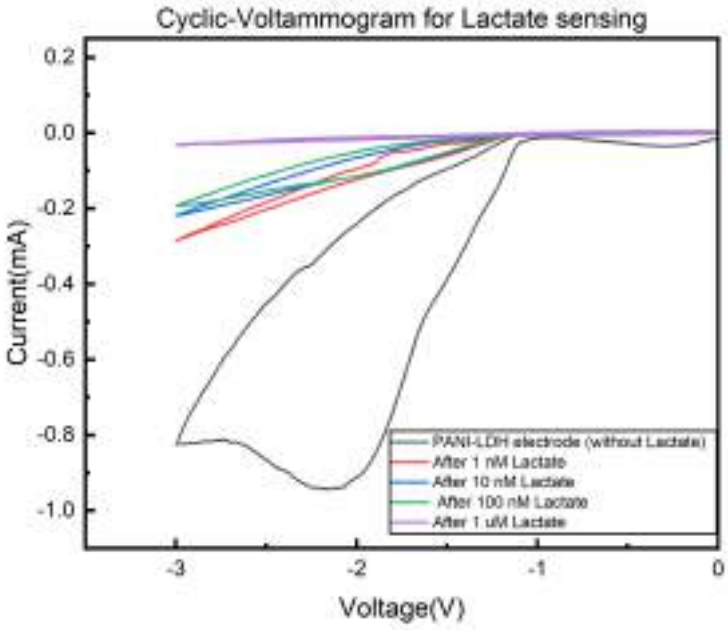

Figure 7.8: cyclic voltammogram study of lactate detection over PANI-LDH electodes.

linearity can be only seen in this range, the actual limit of detection for the PANI-LDH electrodes was 10 pM which is a significant improvement over the reported literature. All the work on Lactate

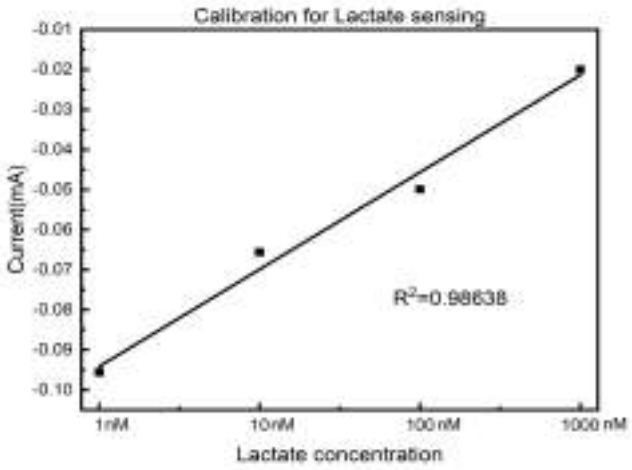

Figure 7.9: Calibration curve for lactate detection over PANI-LDH electrodes.

detection by electrochemical method to date is based mainly on Ampiometric detection; Table 7.1 shows the comparison of results of enzymatic lactate detection with the previous reported literature. From Table 7.1, it can be concluded that the proposed electrode has better sensitivity as well as the limit of detection than the reported literature. This is because of the different morphological and chemical characteristics of the deposited PANI film. In the literature, the PANI film is deposited in the presence of HCl, whereas in the present work H_2SO_4 is used, which causes the sulfur doping in the film. In addition, the difference of the constant potential during the polymerization of PANI film changes it morphological characteristics, which can increase the conductivity of the film. Therefore, it can be concluded that the PANI-LDH electrode proposed in the present work has better sensing capabilities towards lactate sensing, and they can be used in monitoring physiological processes such as estimation of glycolysis in pancreas.

7.6 Summary

This work demonstrates sulfur-doped PANI-coated ITO electrodes for lactate detection applications. The electrodes were fabricated through Chrono-amperometry, which is less time-consuming and cost-effective. These electrodes are of good quality and were stable in liquids. Since LDH is negatively charged and PANI surface is positively charged, therefore, electrostatic coupling occurred

between them, because of which a simple drop-casting followed by incubation technique of LDH immobilization was employed. These electrodes were used for lactate detection with the help of cyclic voltammetry. The proposed electrodes had higher sensitivity at a low concentration of Lactate and a very low detection limit of 10 pM. The linear detection range was observed from 1-100 nM and with a sensitivity of 95.6 uA/nM. Our result proves that the proposed electrodes are simple, cost-effective, and highly sensitive towards lactate detection can be used as lactate sensing at point of care applications.

8

Summary and Conclusions

Contents

This chapter outlines and summarizes the results obtained from the works presented in this thesis. However, during this thesis work, numerous possible directions for further investigations were identified. All these aspects are mentioned at the end of this chapter under the future scope section.

8.1 Summary and Conclusions

This thesis focused on the theoretical and experimental aspects of graphene-based devices, which are employed for bio-sensing applications. The first part of the thesis explored various approaches to theoretically simulate, observe, and model the interactions between the sensing layer and analyte molecule. Out of the various approaches discussed, the Density Functional Theory based is capable of studying the system presented in the thesis. This thesis consists of a number of theoretical studies starting from simple systems with gradually increasing complexity. In the first study, the Density Functional Theory (DFT) based study was conducted to observe the interactions between gaseous air pollutants, including di-atomic (CO and NO), tri-atomic (CO_2 and HCN), and poly-atomic (HCHO and $COCl_2$) species, and Ti-doped zigzag graphene nanoribbon (ZGNR) structures. The major outcomes of this study includes the suitability of Ti-doped ZGNR structures for the adsorption of these gases, particularly the doping in which the Ti atom replaces two carbon atoms. Since, after the adsorption, the changes in the density of states are observed, suggesting that the Ti-doped ZGNR can be used as the sensing platform for these gases. In the second study, the thorough analysis of the interaction between Phosgene ($COCl_2$) on two configurations of Titanium doped Graphene Nanoribbons (GNR)- Armchair GNR and ZigZag GNR has been done. The results indicate that in a few cases, the Titanium atom causes a catalytic splitting of the C-Cl bond, reducing the toxic gas into less harmful by-products (i.e., Carbon mono-oxide gas is released after the adsorption, while the Chlorine atoms attach to the substrate).The preventive action of the Oxygen atom was in the gas was also observed in a small minority of the cases; it may partially shield the C-Cl bond and form a physical barrier to the splitting. This study was further extended to two other molecules, one with an S-Cl bond ($SOCl_2$ -Thionyl Chloride) and one with an O-Cl bond ($POCl_3$). Our results demonstrate that Ti-doped graphene nanoribbons have great potential to be used as a platform for toxic gas treatment and sensing. Till now, only the gaseous entities are considered. Therefore, in the subsequent study, the interactions between Urea with pristine and transition metal (TM) doped two-dimensional graphene structures were explored. Four TM-dopants, namely, V, Ti, Fe, and Cr, are considered, and results

Table 8.1: Summary of Theoretical Studies

S.No.	System			Theory	Parameters	Major outcome	Special Remarks	Application
	Substrate	Doping	Analyte molecules					
1	ZGNR	Ti atom replacing one carbon (SV-ZGNR) and replacing two carbon (DV-ZGNR)	CO,NO, CO_2, and HCHO	DFT GGA-PBE	Mesh Cutoff= 370 Ry K-Point Grid = 1 ×1 × 45 Force Tolerance = 0.01 eV/Ang Optimization Algorithm = CG	Ti doped SV and DV-ZGNR structures favours the adsorption of these gases over pristine ZGNR	Changes in electronic structure of Ti doped ZGNR after adsorption	Ti-doped ZGNR have potential to be used as sensing platform
2	ZGNR and AGNR	Ti atom replacing one carbon (SV-ZGNR) and replacing two carbon (DV-ZGNR)	$COCl_2$, $SOCl_2$, and $POCl_3$	DFT GGA-PBE	Mesh Cutoff= 370 Ry K-Point Grid = 1 ×1 × 45 Force Tolerance = 0.01 eV/Ang Optimization Algorithm = CG	Ti doped ZGNR and AGNR structures favours the adsorption of these gases over pristine ZGNR and AGNR	1. Changes in electronic structure of Ti doped ZGNR after adsorption. 2. Splitting of $COCl_2$, $SOCl_2$, and $POCl_3$ over Ti doped ZGNR.	1. Ti doped ZGNR can be used for sensing these gases. 2. Also, Ti doped ZGNR can be explored in catalytic conversion of these toxic gases.
3	Two-dimensional Graphene sheet	Transition metal (TM) doping (V, Ti, Fe, and Cr) TM atom replacing one carbon atom from sheet	Urea	DFT GGA-PBE	Mesh Cutoff= 370 Ry K-Point Grid = 7 × 7 × 1 Force Tolerance = 0.01 eV/Ang Optimization Algorithm = CG	All TM doped Graphene sheets favours the adsorption of Urea molecules over pristine graphene	1. V-doped Graphene sheets are preferred for Urea adsorption as compared to other doped sheets. 2. Each case significant charge transfer and electronic structure variation was observed	TM doped Graphene sheets can be a sensing platform for Urea.
4	Two-dimensional Graphene sheet	Ti atom replacing one carbon atom from sheet	Chloro-fluoro-carbon (CFC) $CFCl_3$, CCl_2F_2, $CClF_3$	DFT GGA-PBE	Mesh Cutoff= 370 Ry K-Point Grid = 7 × 7 × 1 Force Tolerance = 0.01 eV/Ang Optimization Algorithm = CG	Ti doped graphene sheets favours adsorption of the CFC over pristine graphene	1. Changes in electronic structure of Ti doped graphene sheet after adsorption. 2. Splitting of $CFCl_3$ and CCl_2F_2 over Ti-doped graphene sheet. 3. $CClF_3$ does not possess splitting tendency over Ti-doped graphene sheet.	1. Ti doped graphene sheet can be used for sensing CFCs. 2. Also, Ti doped graphene sheet can be exploredf or catalytic conversion of $CFCl_3$ and CCl_2F_2

indicate that TM-doped ZGNR is better for Urea adsorption as compared to the pristine 2-D graphene sheet, particularly V-doped structure is preferred over others in terms of adsorption. Once again, the changes in the electronic structures after the adsorption suggests that TM-doped ZGNR can have the potential to be the sensing platform for Urea. In the last theoretical study, Chlorofluorocarbons (CFC) molecules, namely $CFCl_3$, $CClF_3$, and CCl_2F_2 adsorption over pristine and Ti-doped two-dimensional graphene sheets was studied. The obtained results indicate strong chemical interaction of the Ti-doped graphene as compared to the pristine graphene. Other than the significant transfer of charge and variation in the electronic structure after the adsorption, in some cases, splitting of the molecules was observed. Therefore, once again, the study suggests that Ti-doped graphene nanostructures can be used for sensing as well as catalytic conversion of these gases. A thorough summary of all the above-mentioned studies is presented in Table 8.1.

The second part of the thesis explored the fabrication of devices with functionalized graphene as a sensing layer for the biosensing application. During this, the synthesis procedure of functionalized graphene was discussed, followed by their characterization. Finally, these synthesized graphenes were employed as a channel in a chemiresistor sensing device. The antibodies of Glutathione were immobilized over this channel layer, and sensing experiments were conducted, and sensor parameters

Table 8.2: Summary of Experimental Work

Device Architecture or Sensing Method	Sensing Material	Sensitivity	Range of Detection	Limit of Detection	Sample Volume	Measurement Time	Remarks
Chem-resistive	Antibody immobilized over amine functionalized graphene oxide	0.01 uA/nM	1nM - 10 uM	1 nM	1uL	Approx. 5 sec	1. Excellent selectivity 2. Device can be stored at 4 Degree Celsius for long term use.
Cyclic Voltammetry	LDH functionalized sulfur doped PANI-ITO electrodes	95.6 uA/nM	1-100 nM	10 pM	-	Approx. 5 min	1. Simple fabrication of electrodes 2. Cost-effective and highly sensitive

were estimated. Our results prove that the proposed device has better sensitivity and selectivity than the reported literature. Finally, in Chapter-7, the electrochemical sensing of Lactate is demonstrated using functionalized Polyaniline as a sensing layer. The sensing action demonstrated using cyclic voltammetry, and sensing parameters were estimated. The fabricated electrode achieved good sensitivities and limit of detection as compared to the reported literature. A thorough summary of all the above-mentioned experimental works is presented in Table 8.2.

8.2 Future Scope

Based on the conclusion of the theoretical studies presented in the thesis, there can be a few possible directions for further investigations, which are given as follows:

- The effect of concentration of doping as well as ZGNR width on the adsorption of the gases can be explored.
- Other than DFT-PBE, the adsorption process can be studied with hybrid functionals, which may provide more accuracy.
- These adsorptions studies conducted can be further elaborated with molecular dynamics or QM/MM simulations, therefore, the effect of system size, temperature, and pressure can be observed. Hence, a multi-level simulation model can be prepared.
- Finally, the effect of adsorption on the transport properties can be explored through Non-Equilibrium Green's Functions formalism. These simulations are complex and time-consuming but can provide variation I-V characteristics after the adsorption of gas molecules.

The experimental studies presented in the thesis can be further extended with the following aspects:

- The Field Effect Transistor can be fabricated with the proposed antibody immobilized amine-functionalized graphene as the channel, and the effect of gate voltage on the sensor parameter can be observed.
- The effect of temperature and pH of the analyte on the sensing action can be explored. Hence, optimum temperature and pH can be estimated for the sensing.
- The real-life samples such as cell lysate or blood samples can be tested with the proposed device. During this, the cause of degradation of the results or sensor device can be studied. The remedies to such problems can also be an interesting research topic.
- The small, cost-effective readout circuit for GSH and Lactate sensor should be explored for point of care device applications.

A

Mask Fabrication

Contents

A.1 Mask Fabrication

As mentioned above, the standard silicon fabrication process was employed for sensor fabrication and optical lithography is a key step in the same. In order to perform the optical lithography process, glass masks are essential. Therefore, this section describes the glass mask fabrication, the overall process flow is shown in the Figure A.1 followed by details of each step. There are two types of glass masks employed, iron oxide coated and chromium coated soda lime gass, the former one is cheaper and see through than the later one. Both kind of masks have 5300 A of AZ1518 Photoresist coated over them, therefore, these mask plates must be carefully handled under yellow ultra-violet light condition.

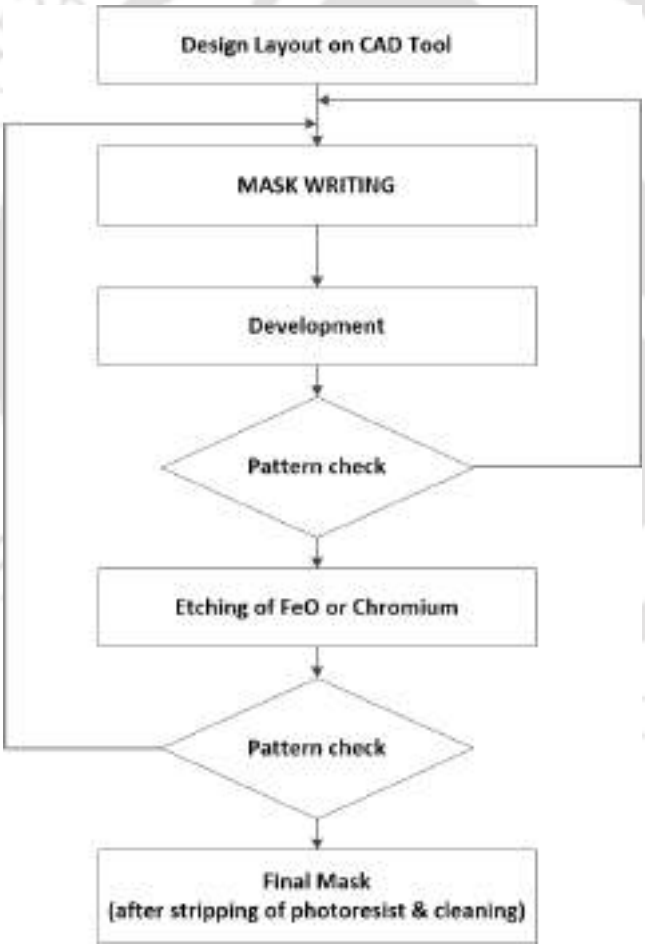

Figure A.1: Process flow for MASK fabrication.

The mask fabrication process starts with the designing of the layout of the micro-structures (device structures) on the CAD tool, we use clevin version for the same. The design file is converted to mask writer file formats and fed to the control software of the mask writer machine (Heidelberg and Dilase 250). These mask writer equipments are capable of transfering the device structure image on the

mask plates through direct laser writing exposure lithography. The typical exposure dosage for the AZ 1518 phototresists is about 110mJ but it must be optimized as per the device structure as well as feature size. The exposure process alter the chemical structure of the photoresist hence making it soluble in developer solution. The exposed mask plates were immersed in the Microchem developer solution for 20-30 seconds with mild shaking like agitations in order to ease the dissolution of the exposed photoresist. The developer solutions are corrosive in nature and once the development is over, the plates should be thoroughly cleaned with running DI water, therefore, the stopping the development action. The developer solutions didnt attack the iron oxide or chromium layer lying under the developed regions, hence, etching is performed by placing them in Microchem etchant solution with gental agitation till the iron oxide or chromium dissolved properly followed by DI water wash for one minute to remove any etchant left. The plates were dried under nitrogen blow and inspected under microscope.

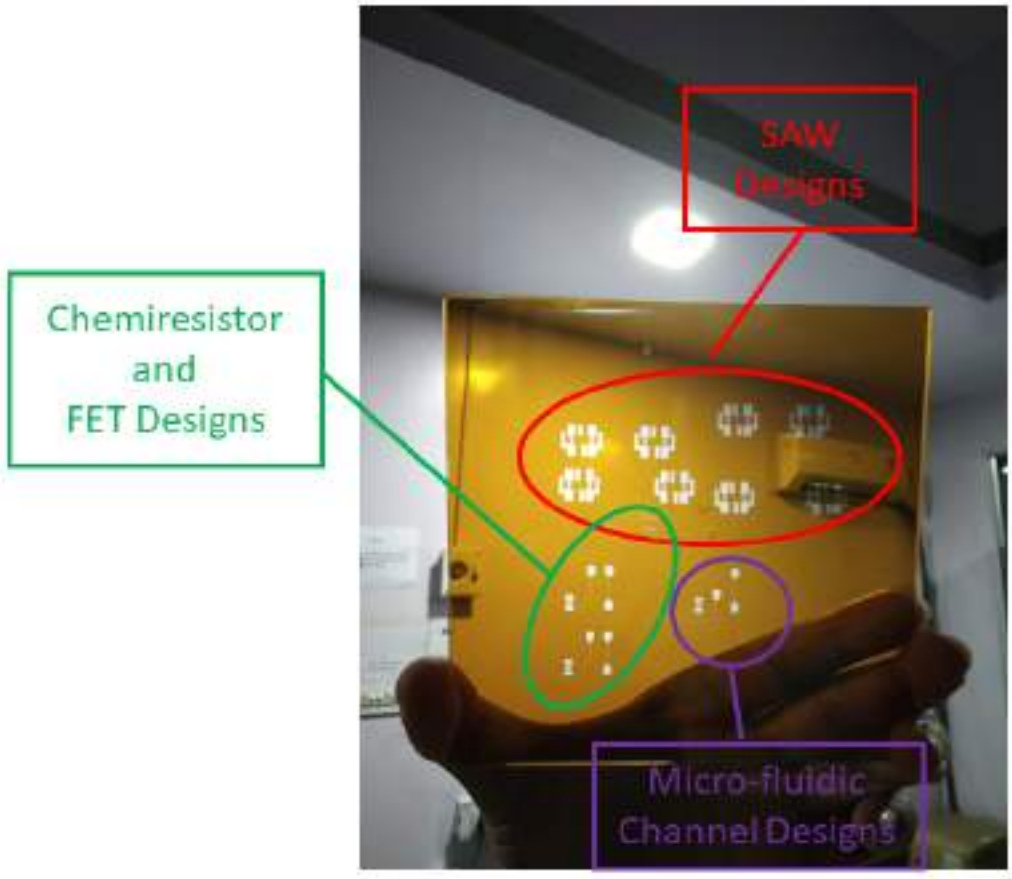

Figure A.2: Process flow for Device fabrication.

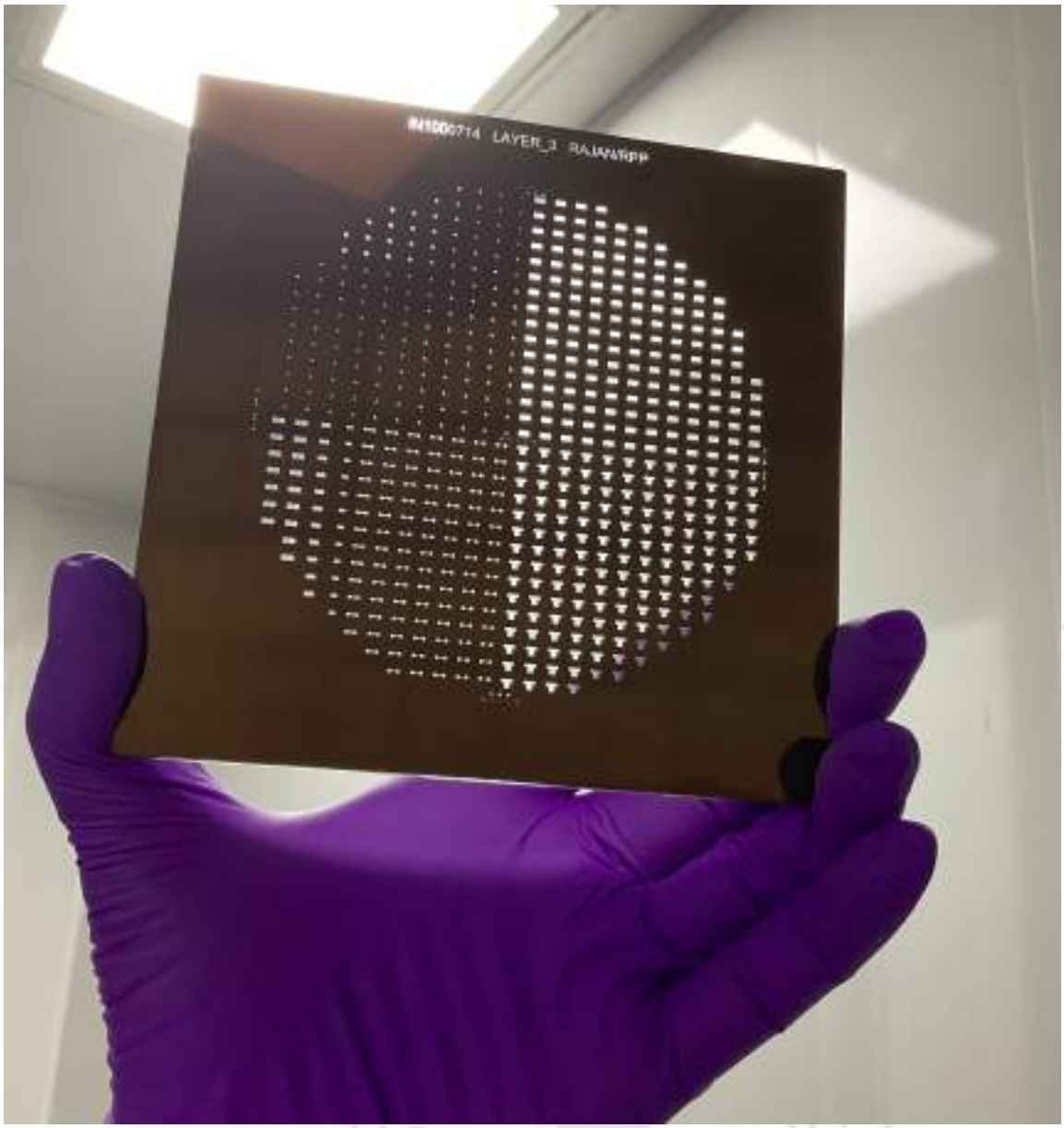

Figure A.3: Process flow for Device fabrication.

If in case of any imperfections, the previous steps needs to repeat with the appropriate modifications. Once the desired designs were obtained over the mask plate, then the remaining photoresist needs to be stripped by immersing them in Microchem stripper solution or acetone solution. After the photoresist stripping, mask plates were cleaned with running DI water and dried with nitrogen stream. In the end, final inspections were done under the optial microscope. The optical images for the fabricated MASKs are given in Figure A.2 and A.3.

A.2 Device Fabrication

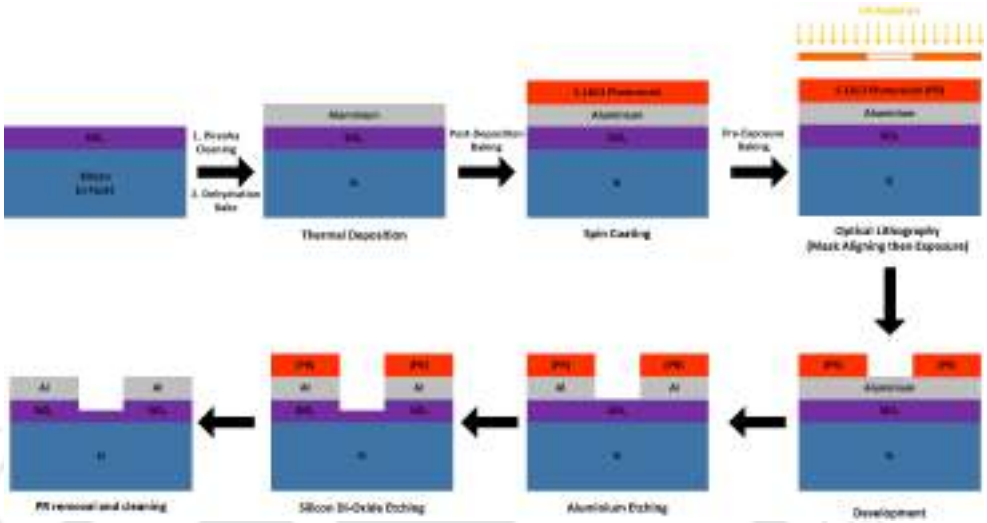

Figure A.4: Process flow for Device fabrication.

The detailed fabrication process shown in Figure A.4 is discussed as follows:

- Wafer Cleaning: The device were fabricated on n-type Silicon wafers 4inch diameter and 500um thickness with $< 100 >$ orientation and 300 nm thermally grownd SiO_2 over it. These wafers were cleaned through acidic piranha solution 3:1 mixture of H_2SO_4 and H_2O_2 for 10-15 minutes with gentle agitation. The wafers were cleaned thoroughly with running DI water for 1-2 minutes to remove left over piranha solution then dried in nitrogen stream. The wafers were then subjected to ozone cleaning to remove hydrocarbons and obatain hydrophobic surface.

- Dehydration Bake: The cleaned wafers from previous steps were heated to 175 degrees Celsius for 10-15 minutes to remove the moisture and any residual liquid over the surface. After the baking, the wafers were allowed to cool down to room temperature.

- Metal Deposition: The Aluminium deposition was performed to make the contacts. The procedure was done in a thermal deposition equipment. A high purity aluminium wire placed in tugesten filament was used to deposite aluminium. The pressure at the time of deposition was 5×10^{-6} torr and the obatined thickness was 100nm.

- Spin coating of Primer: The surface wettability properties of the wafer can severally affect the photoresist adhesion. Improper adhesion may lead to development and etching issues and can

cause complete removal of photoresist film. Thus, the proper adhesion must be ensured. One way to achieve proper adhesion is through Primer soltion. The HMDS Primer solution was coated over the wafers at 6000 rpm for 1 minute followed by a baking at 175 degrees Celsius for 10 minutes.

- Spin coating of photoresist: The S1813 positive photoresist was employed for this work. The photoresist solution was carefully poured over wafers in order to avoid any bubbles. The coating was performed at 3500 rpm for 1 minute.

- Soft bake: After the coating, photoresist films were subjected to baking at 135 degrees Celsius for 3 minutes. Soft baking is needed to ensure the removal of solvents or liquid from the film and ensuring proper adhesion.

- Lithography: The micro-structures or contact patterns were transferred over the photoresist coated wafers through optical lithpgraphy process performed over UV LED exposure-masking system Kloe UV-KUB 2 equipment. This eqipment operates at 365 nm UV LED sources and can provide maximum power density of 35mW/cm2. The typical dosage for S-1813 photoresist is 150 mJ/cm2 at 436 nm illumination which provides a good starting point for the dose optimization. The dosage for different micro-structures as per their size and critical dimensions were optimized before performing the actual lithography and the optimized dosage between 75-85 mJ/cm2.

- Development: The lithography process was supoose to chemically alter the exposed photoresists and therefore it can be removed during the developement process. In this, the exposed wafers were immersed into MIF-319 developer solutions with mild agitations for about 20 seconds. As the developement process dissolved the photoresist and hence the micro-structures can be seen. The developed wafers were then washed with DI water to stop the development action as well as remove any left over developer.

- Aluminium etching: The Aluminium which is exposed after the development process was subjected to etching with the help of aluminum etchant solution which is a mixture of H3PO4:HNO3:H2O = [19:1:4] ratio [18]. The process was performed till a few minutes to completely remove the aluminium layer. After that, the sample was cleaned with DI water five times and heated at 120 degrees Celsius for 15 min.

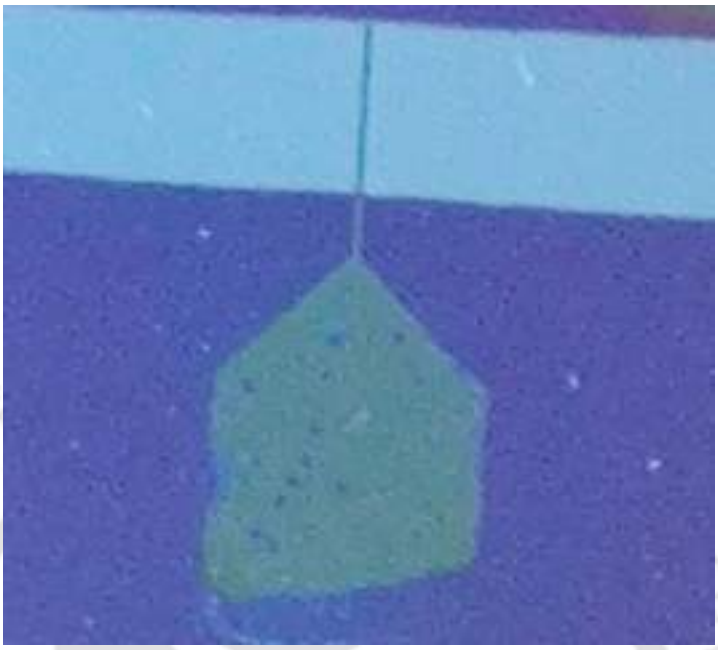

Figure A.5: The optical image of the fabricated device for sensing application.

- SiO2 etching: In order to etch the SiO2 layer and form the trench, we explored hydrofluoric acid (HF) solution with varying percentages. It was observed that HF etching was violent and can damage oxide as well as photoresist. Therefore, Buffered oxide etch (BOE) which is much safer etchant was emplyed. BOE is a mixture of ammonium fluoride (NH4F) and hydrofluoric acid (HF) [10:1]. Ammonium fluoride minimizes the violent action of HF and hence the etching is uniform.

- Cleaning: In the end, the remaining layer of photoresist needs to be removed. However, after multiple heating cycles, the photoresist layer is very hardened, and therefore, photoresist stripper solution is required rather than a simple acetone cleaning. The stripper solution is a solution of 1-methyl-2-pyrrolidone. The wafers were immeresed in hot 70 degrees Celsius stripper solution and agitated gently. After the complete removal of photoresist, the wafers were thoroughly cleaned with running DI water and dried under nitrogen stream. Finally, the wafers were heated at 150 degrees Celsius for 10 minutes before storing them in vacuum dessicators. The optical image of the fabricate device is given in Figure A.5.

Bibliography

[1] "Biosensor," http://en.wikipedia.org/wiki/Biosensor, 2015, [Online; accessed 3-JUN-2015].

[2] S. Sang, Y. Wang, Q. Feng, Y. Wei, J. Ji, and W. Zhang, "Progress of new label-free techniques for biosensors: a review," *Critical Reviews in Biotechnology*, vol. 0, no. 0, pp. 1–17, 0, pMID: 25608959. [Online]. Available: http://dx.doi.org/10.3109/07388551.2014.991270

[3] R. Monošík, M. Streďanskỳ, and E. Šturdík, "Biosensors-classification, characterization and new trends," *Acta chimica slovaca*, vol. 5, no. 1, pp. 109–120, 2012.

[4] P. Bergveld, "The development and application of fet-based biosensors," *Biosensors*, vol. 2, no. 1, pp. 15 – 33, 1986. [Online]. Available: http://www.sciencedirect.com/science/article/pii/0265928X86850106

[5] D.-S. Kim, J.-E. Park, J.-K. Shin, P. K. Kim, G. Lim, and S. Shoji, "An extended gate fet-based biosensor integrated with a si microfluidic channel for detection of protein complexes," *Sensors and Actuators B: Chemical*, vol. 117, no. 2, pp. 488 – 494, 2006, transducers '05 Selected Papers from {TRANSDUCERS} '05. The 13th International Conference on Solid-State Sensors, Actuators and Microsystems. [Online]. Available: http://www.sciencedirect.com/science/article/pii/S0925400506000189

[6] H. J. N. P. D. Mello, T. Heimfarth, and M. Mulato, "Influence of the physicalchemical properties of polyaniline thin films on the final sensitivity of varied field effect sensors," *Materials Chemistry and Physics*, vol. 160, no. 0, pp. 257 – 263, 2015. [Online]. Available: http://www.sciencedirect.com/science/article/pii/S0254058415300353

[7] I. Basu, R. Subramanian, A. Mathew, A. M. Kayastha, A. Chadha, and E. Bhattacharya, "Solid state potentiometric sensor for the estimation of tributyrin and urea," *Sensors and Actuators B: Chemical*, vol. 107, no. 1, pp. 418 – 423, 2005, proceedings of the 7th European Conference on Optical Chemical Sensors and Biosensors EUROPT(R)ODE {VII}. [Online]. Available: http://www.sciencedirect.com/science/article/pii/S0925400504007294

[8] D. Grieshaber, R. MacKenzie, J. Voeroes, and E. Reimhult, "Electrochemical biosensors-sensor principles and architectures," *Sensors*, vol. 8, no. 3, pp. 1400–1458, 2008.

[9] G. M. Mntze, B. Baur, W. Schfer, A. Sasse, J. Howgate, K. Rth, and M. Eickhoff, "Quantitative analysis of immobilized penicillinase using enzyme-modified algan/gan field-effect transistors," *Biosensors and Bioelectronics*, vol. 64, no. 0, pp. 605 – 610, 2015. [Online]. Available: http://www.sciencedirect.com/science/article/pii/S0956566314007490

[10] K. Kiilerich-Pedersen and N. Rozlosnik, "Cell-based biosensors: Electrical sensing in microfluidic devices," *Diagnostics*, vol. 2, no. 4, pp. 83–96, 2012.

[11] S. Wustoni, S. Hideshima, S. Kuroiwa, T. Nakanishi, M. Hashimoto, Y. Mori, and T. Osaka, "Sensitive electrical detection of human prion proteins using field effect transistor biosensor with dual-ligand binding amplification," *Biosensors and Bioelectronics*, vol. 67, no. 0, pp. 256 – 262, 2015, special Issue: {BIOSENSORS} 2014. [Online]. Available: http://www.sciencedirect.com/science/article/pii/S0956566314006162

[12] N. Yang, X. Chen, T. Ren, P. Zhang, and D. Yang, "Carbon nanotube based biosensors," *Sensors and Actuators B: Chemical*, vol. 207, Part A, no. 0, pp. 690 – 715, 2015. [Online]. Available: http://www.sciencedirect.com/science/article/pii/S0925400514012507

[13] M.-Y. Shen, B.-R. Li, and Y.-K. Li, "Silicon nanowire field-effect-transistor based biosensors: From sensitive to ultra-sensitive," *Biosensors and Bioelectronics*, vol. 60, no. 0, pp. 101 – 111, 2014. [Online]. Available: http://www.sciencedirect.com/science/article/pii/S0956566314002383

[14] E. Hill, A. Vijayaragahvan, and K. Novoselov, "Graphene sensors," *Sensors Journal, IEEE*, vol. 11, no. 12, pp. 3161–3170, Dec 2011.

[15] R. M. Martin, *Electronic structure: basic theory and practical methods*. Cambridge university press, 2004.

[16] R. G. Parr, "Density functional theory of atoms and molecules," in *Horizons of Quantum Chemistry*. Springer, 1980, pp. 5–15.

[17] "IUPAC GOLD BOOK," http://goldbook.iupac.org/B00663.html, 2015, [Online; accessed 3-JUN-2015].

[18] X.-L. Luo, J.-J. Xu, W. Zhao, and H.-Y. Chen, "A novel glucose {ENFET} based on the special reactivity of mno2 nanoparticles," *Biosensors and Bioelectronics*, vol. 19, no. 10, pp. 1295 – 1300, 2004. [Online]. Available: http://www.sciencedirect.com/science/article/pii/S0956566303004251

[19] A. Purwidyantri, H.-C. Lai, S.-H. Tsai, J.-D. Luo, C.-C. Chiou, Y.-C. Tian, C.-H. Cheng, Y.-T. Lin, and C.-S. Lai, "Sensing performance of fibronectin-functionalized au-egfet on the detection of s. epidermidis biofilm and 16s rrna of infection-related bacteria in peritoneal dialysis," *Sensors and Actuators B: Chemical*, vol. 217, no. 0, pp. 92 – 99, 2015, selected Papers from the 15th International Meeting on Chemical Sensors, 16-19 March 2014, Buenos Aires, Argentina. [Online]. Available: http://www.sciencedirect.com/science/article/pii/S0925400514013793

[20] P. Wang and Q. Liu, Eds., *Cell-based biosensors : principles and applications*, ser. Artech House series engineering in medicine & biology. Boston: Artech House, 2010, nlmcopyc. [Online]. Available: http://opac.inria.fr/record=b1130919

[21] J. Parka, H. H. Nguyena, A. Woubitc, and M. Kima, "Applications of field-effect transistor (fet)-type biosensors," vol. 23, no. 2, pp. 61–71, 2014.

[22] F. Khoshnoud and C. de Silva, "Recent advances in mems sensor technology biomedical applications," *Instrumentation Measurement Magazine, IEEE*, vol. 15, no. 1, pp. 8–14, February 2012.

[23] ——, "Recent advances in mems sensor technology-mechanical applications," *Instrumentation Measurement Magazine, IEEE*, vol. 15, no. 2, pp. 14–24, April 2012.

[24] S. Cheng, S. Hideshima, S. Kuroiwa, T. Nakanishi, and T. Osaka, "Label-free detection of tumor markers using field effect transistor (fet)-based biosensors for lung cancer diagnosis," *Sensors and Actuators B: Chemical*, vol. 212, no. 0, pp. 329 – 334, 2015. [Online]. Available: http://www.sciencedirect.com/science/article/pii/S0925400515002117

[25] Z.-D. Lin, C.-H. Hsiao, S.-J. Young, C.-S. Huang, S.-J. Chang, and S.-B. Wang, "Carbon nanotubes with adsorbed au for sensing gas," *Sensors Journal, IEEE*, vol. 13, no. 6, pp. 2423–2427, June 2013.

[26] C.-T. Lee, Y.-S. Chiu, L.-R. Lou, S.-C. Ho, and C.-T. Chuang, "Integrated ph sensors and performance improvement mechanism of zno-based ion-sensitive field-effect transistors," *Sensors Journal, IEEE*, vol. 14, no. 2, pp. 490–496, Feb 2014.

[27] A. Fattah and S. Khatami, "Selective h2s gas sensing with a graphene/n-si schottky diode," *Sensors Journal, IEEE*, vol. 14, no. 11, pp. 4104–4108, Nov 2014.

[28] C.-H. Huang, I.-S. Wang, K.-I. Ho, Y.-T. Lin, C. Chou, C.-F. Chan, and C.-S. Lai, "High polarization and low-repulsion hfo2 thin film for alkali metal ion detections by plasma system with a complementary filter," *IEEE SENSORS JOURNAL*, vol. 13, no. 6, p. 2459, 2013.

[29] A. Gao, N. Lu, P. Dai, T. Li, H. Pei, X. Gao, Y. Gong, Y. Wang, and C. Fan, "Silicon-nanowire-based cmos-compatible field-effect transistor nanosensors for ultrasensitive electrical detection of nucleic acids," *Nano letters*, vol. 11, no. 9, pp. 3974–3978, 2011.

[30] R. S. Andre, M. H. Facure, R. Schneider, F. L. Migliorini, D. M. dos Santos, L. A. Mercante, and D. S. Correa, "Chemical sensors based on nanofibers produced by electrospinning and solution blow spinning," in *Reference Module in Biomedical Sciences*. Elsevier, 2021. [Online]. Available: https://www.sciencedirect.com/science/article/pii/B9780128225486000078

[31] F.-G. Banica, *Chemical sensors and biosensors: fundamentals and applications*. John Wiley & Sons, 2012.

[32] S. Ammu, V. Dua, S. R. Agnihotra, S. P. Surwade, A. Phulgirkar, S. Patel, and S. K. Manohar, "Flexible, all-organic chemiresistor for detecting chemically aggressive vapors," *Journal of the American Chemical Society*, vol. 134, no. 10, pp. 4553–4556, 2012.

[33] R. Yoo, J. Kim, M.-J. Song, W. Lee, and J. S. Noh, "Nano-composite sensors composed of single-walled carbon nanotubes and polyaniline for the detection of a nerve agent simulant gas," *Sensors and Actuators B: Chemical*, vol. 209, pp. 444–448, 2015.

[34] J. F. Fennell, H. Hamaguchi, B. Yoon, and T. M. Swager, "Chemiresistor devices for chemical warfare agent detection based on polymer wrapped single-walled carbon nanotubes," *Sensors*, vol. 17, no. 5, p. 982, 2017.

[35] Y. Wang, Y. Wu, J. Xie, H. Ge, and X. Hu, "Multi-walled carbon nanotubes and metal–organic framework nanocomposites as novel hybrid electrode materials for the determination of nano-molar levels of lead in a lab-on-valve format," *Analyst*, vol. 138, no. 17, pp. 5113–5120, 2013.

[36] C. Viviers, A. du Toit, W. Perold, B. Loos, and J.-H. Hofmeyr, "A resistive biosensor for the detection of lc3 protein in autophagy," *IEEE Sensors Journal*, vol. 20, no. 10, pp. 5119–5129, 2020.

[37] F. Walters, S. Rozhko, D. Buckley, E. D. Ahmadi, M. Ali, Z. Tehrani, J. Mitchell, G. Burwell, Y. Liu, O. Kazakova *et al.*, "Real-time detection of hepatitis b surface antigen using a hybrid graphene-gold nanoparticle biosensor," *2D Materials*, vol. 7, no. 2, p. 024009, 2020.

[38] D. Grieshaber, R. MacKenzie, J. Vörös, and E. Reimhult, "Electrochemical biosensors-sensor principles and architectures," *Sensors*, vol. 8, no. 3, pp. 1400–1458, 2008.

[39] Q. K. Vu, Q. H. Tran, N. P. Vu, T.-L. Anh, T. T. Le Dang, T. Matteo, and T. H. H. Nguyen, "A label-free electrochemical biosensor based on screen-printed electrodes modified with gold nanoparticles for quick detection of bacterial pathogens," *Materials Today Communications*, vol. 26, p. 101726, 2021.

[40] B. Rashmi, S. F. Harlapur, C. Ravikumar, B. Avinash, K. Gurushantha, M. Divakara, M. Santosh, and K. Veena, "Moo3 nanoparticles based electrodes as novel electrochemical sensors for the detection of h2o2," *Materials Today: Proceedings*, vol. 46, pp. 5931–5935, 2021.

[41] F. Hu, T. Liu, J. Pang, Z. Chu, and W. Jin, "Facile preparation of porous co3o4 nanocubes for directly screen-printing an ultrasensitive glutamate biosensor microchip," *Sensors and Actuators B: Chemical*, vol. 306, p. 127587, 2020.

[42] A. C. H. de Castro, L. M. Alves, A. C. S. Siquieroli, J. M. Madurro, and A. G. Brito-Madurro, "Label-free electrochemical immunosensor for detection of oncomarker ca125 in serum," *Microchemical Journal*, vol. 155, p. 104746, 2020.

[43] T. Zhu, X. Wang, W. Chang, Y. Zhang, T. Maruyama, L. Luo, and X. Zhao, "Green fabrication of cu/rgo decorated swcnt buckypaper as a flexible electrode for glucose detection," *Materials Science and Engineering: C*, vol. 120, p. 111757, 2021.

[44] H. Imran, K. Vaishali, S. A. Francy, P. N. Manikandan, and V. Dharuman, "Platinum and zinc oxide modified carbon nitride electrode as non-enzymatic highly selective and reusable electrochemical diabetic sensor in human blood," *Bioelectrochemistry*, vol. 137, p. 107645, 2021.

[45] F. N. Crespilho, *Nanobioelectrochemistry*, 1st ed. Springer-Verlag Berlin Heidelberg, 2013.

[46] P. Bergveld, "Thirty years of isfetology: What happened in the past 30 years and what may happen in the next 30 years," *Sensors and Actuators B: Chemical*, vol. 88, no. 1, pp. 1 – 20, 2003. [Online]. Available: http://www.sciencedirect.com/science/article/pii/S0925400502003015

[47] A. Cazal, W. Sant, J. Launay, F. Ginot, and P. Temple-Boyer, "Study of field effect transistors for the sodium ion detection using fluoropolysiloxane-based sensitive layers," *Sensors and Actuators B: Chemical*, vol. 177, no. 0, pp. 515 – 521, 2013. [Online]. Available: http://www.sciencedirect.com/science/article/pii/S0925400512012506

[48] Y. Alifragis, A. Volosirakis, N. Chaniotakis, G. Konstantinidis, A. Adikimenakis, and A. Georgakilas, "Potassium selective chemically modified field effect transistors based on algan/gan two-dimensional electron gas heterostructures," *Biosensors and Bioelectronics*, vol. 22, no. 12, pp. 2796 – 2801, 2007, chem and Biosensing Transistors: from materials to systems. [Online]. Available: http://www.sciencedirect.com/science/article/pii/S0956566306004878

[49] C.-T. Lee and Y.-S. Chiu, "Photoelectrochemical passivated zno-based nanorod structured glucose biosensors using gate-recessed algan/gan ion-sensitive field-effect-transistors," *Sensors and Actuators B: Chemical*, vol. 210, no. 0, pp. 756 – 761, 2015. [Online]. Available: http://www.sciencedirect.com/science/article/pii/S0925400515000581

[50] M. Sheliakina, V. Arkhypova, O. Soldatkin, O. Saiapina, B. Akata, and S. Dzyadevych, "Urease-based {ISFET} biosensor for arginine determination," *Talanta*, vol. 121, no. 0, pp. 18 – 23, 2014. [Online]. Available: http://www.sciencedirect.com/science/article/pii/S0039914013010357

[51] M. Myers, F. L. M. Khir, A. Podolska, G. A. Umana-Membreno, B. Nener, M. Baker, and G. Parish, "Nitrate ion detection using algan/gan heterostructure-based devices without a reference electrode," *Sensors and Actuators B: Chemical*, vol. 181, no. 0, pp. 301 – 305, 2013. [Online]. Available: http://www.sciencedirect.com/science/article/pii/S0925400513001123

[52] C.-H. Kao, H. Chen, L.-T. Kuo, J.-C. Wang, Y.-T. Chen, Y.-C. Chu, C.-Y. Chen, C.-S. Lai, S. W. Chang, and C. W. Chang, "Multi-analyte biosensors on a {CF4} plasma treated nb2o5-based membrane with an extended gate field effect transistor structure," *Sensors and Actuators B: Chemical*, vol. 194, no. 0, pp. 419 – 426, 2014. [Online]. Available: http://www.sciencedirect.com/science/article/pii/S0925400513015293

[53] B.-R. Huang, S.-C. Hung, and Y.-P. Lo, "Effects of in2o3 modification of sprayed multiwalled carbon nanotubes for ph-sensing applications," *Materials Science in Semiconductor Processing*, vol. 26, no. 0, pp. 710 – 715, 2014. [Online]. Available: http://www.sciencedirect.com/science/article/pii/S1369800114003552

[54] T. Goda and Y. Miyahara, "Label-free and reagent-less protein biosensing using aptamer-modified extended-gate field-effect transistors," *Biosensors and Bioelectronics*, vol. 45, no. 0, pp. 89 – 94, 2013. [Online]. Available: http://www.sciencedirect.com/science/article/pii/S0956566313000560

[55] Y.-S. Chiu, C.-T. Lee, L.-R. Lou, S.-C. Ho, and C.-T. Chuang, "Wide linear sensing sensors using zno:ta extended-gate field-effect-transistors," *Sensors and Actuators B: Chemical*, vol. 188, no. 0, pp. 944 – 948, 2013. [Online]. Available: http://www.sciencedirect.com/science/article/pii/S092540051300912X

[56] A. Das, D. H. Ko, C.-H. Chen, L.-B. Chang, C.-S. Lai, F.-C. Chu, L. Chow, and R.-M. Lin, "Highly sensitive palladium oxide thin film extended gate {FETs} as ph sensor," *Sensors and Actuators B: Chemical*, vol. 205, no. 0, pp. 199 – 205, 2014. [Online]. Available: http://www.sciencedirect.com/science/article/pii/S092540051401034X

[57] C.-M. Yang, I.-S. Wang, Y.-T. Lin, C.-H. Huang, T.-F. Lu, C.-E. Lue, D. G. Pijanowska, M.-Y. Hua, and C.-S. Lai, "Low cost and flexible electrodes with {NH3} plasma treatments in extended gate field effect transistors for urea detection," *Sensors and Actuators B: Chemical*, vol. 187, no. 0, pp. 274 – 279, 2013, selected Papers from the 14th International Meeting on Chemical Sensors. [Online]. Available: http://www.sciencedirect.com/science/article/pii/S0925400512012026

[58] T.-W. Lin, D. Kekuda, and C.-W. Chu, "Label-free detection of dna using novel organic-based electrolyte-insulator-semiconductor," *Biosensors and Bioelectronics*, vol. 25, no. 12, pp. 2706–2710, 2010.

[59] T.-M. Pan, C.-W. Lin, W.-Y. Lin, and M.-H. Wu, "High-tm2 ti2 o7 electrolyte-insulator-semiconductor creatinine biosensor," *IEEE SENSORS JOURNAL*, vol. 11, no. 10, 2011.

[60] R. Preetha, K. Rani, M. S. S. Veeramani, R. E. Fernandez, H. Vemulachedu, M. Sugan, E. Bhattacharya, and A. Chadha, "Potentiometric estimation of blood analytestriglycerides and urea: Comparison with clinical data and estimation of urea in milk using an electrolyte–insulator–semiconductor–capacitor (eis-cap)," *Sensors and Actuators B: Chemical*, vol. 160, no. 1, pp. 1439–1443, 2011.

[61] N. C. Vieira, A. Figueiredo, E. G. Fernandes, F. E. Guimares, and V. Zucolotto, "Nanostructured polyaniline thin films as urea-sensing membranes in field-effect devices," *Synthetic Metals*, vol. 175, no. 0, pp. 108 – 111, 2013. [Online]. Available: http://www.sciencedirect.com/science/article/pii/S0379677913002282

[62] A. Diallo, L. Djeghlaf, L. Mazenq, J. Launay, W. Sant, and P. Temple-Boyer, "Development of ph-based elecfet biosensors for lactate ion detection," *Biosensors and Bioelectronics*, vol. 40, no. 1, pp. 291 – 296, 2013, selected Papers from the World Congress on Biosensors. [Online]. Available: http://www.sciencedirect.com/science/article/pii/S0956566312005052

[63] M.-H. Wu, H.-W. Yang, M.-Y. Hua, Y.-B. Peng, and T.-M. Pan, "High- gdtixoy sensing membrane-based electrolyteinsulatorsemiconductor with magnetic nanoparticles as enzyme carriers for protein contamination-free glucose biosensing," *Biosensors and Bioelectronics*, vol. 47, no. 0, pp. 99 – 105, 2013. [Online]. Available: http://www.sciencedirect.com/science/article/pii/S0956566313001723

[64] M. Holzinger, A. Le Goff, and S. Cosnier, "Nanomaterials for biosensing applications: a review," *Frontiers in chemistry*, vol. 2, 2014.

[65] X.-N. Wang and P.-A. Hu, "Carbon nanomaterials: controlled growth and field-effect transistor biosensors," *Frontiers of Materials Science*, vol. 6, no. 1, pp. 26–46, 2012.

[66] R. A. C. Jr, S. Vaddiraju, P.-Y. Chan, R. Seyta, and F. C. Jain, "Label-free protein detection based on vertically aligned carbon nanotube gated field-effect transistors," *Sensors and Actuators B: Chemical*, vol. 160, no. 1, pp. 154 – 160, 2011. [Online]. Available: http://www.sciencedirect.com/science/article/pii/S092540051100668X

[67] S. Liu and X. Guo, "Carbon nanomaterials field-effect-transistor-based biosensors," *NPG Asia Materials*, vol. 4, no. 8, p. e23, 2012.

[68] H. Pandana, K. Aschenbach, D. R. Lenski, M. S. Fuhrer, J. Khan, and R. D. Gomez, "A versatile biomolecular charge-based sensor using oxide-gated carbon nanotube transistor arrays," *Sensors Journal, IEEE*, vol. 8, no. 6, pp. 655–660, June 2008.

[69] J. Oh, G. Yoo, Y. W. Chang, H. J. Kim, J. Jose, E. Kim, J.-C. Pyun, and K.-H. Yoo, "A carbon nanotube metal semiconductor field effect transistor-based biosensor for detection of amyloid-beta in human serum," *Biosensors and Bioelectronics*, vol. 50, no. 0, pp. 345 – 350, 2013. [Online]. Available: http://www.sciencedirect.com/science/article/pii/S0956566313004740

[70] W.-L. Tsai, B.-T. Huang, K.-Y. Wang, Y.-C. Huang, P.-Y. Yang, and H.-C. Cheng, "Functionalized carbon nanotube thin films as the ph sensing membranes of extended-gate field-effect transistors on the flexible substrates," *Nanotechnology, IEEE Transactions on*, vol. 13, no. 4, pp. 760–766, July 2014.

[71] E. Buitrago, M. Fernndez-Bolaos, S. Rigante, C. F. Zilch, N. S. Schrter, A. M. Nightingale, and A. M. Ionescu, "The top-down fabrication of a 3d-integrated, fully cmos-compatible {FET} biosensor based on vertically stacked sinws and finfets," *Sensors and Actuators B: Chemical*, vol. 193, no. 0, pp. 400 – 412, 2014. [Online]. Available: http://www.sciencedirect.com/science/article/pii/S0925400513014822

[72] M. O. Noor and U. J. Krull, "Silicon nanowires as field-effect transducers for biosensor development: A review," *Analytica chimica acta*, vol. 825, pp. 1–25, 2014.

[73] B. R. Dorvel, B. Reddy Jr, J. Go, C. Duarte Guevara, E. Salm, M. A. Alam, and R. Bashir, "Silicon nanowires with high-k hafnium oxide dielectrics for sensitive detection of small nucleic acid oligomers," *ACS nano*, vol. 6, no. 7, pp. 6150–6164, 2012.

[74] A. Tarasov, M. Wipf, R. L. Stoop, K. Bedner, W. Fu, V. A. Guzenko, O. Knopfmacher, M. Calame, and C. Schnenberger, "Understanding the electrolyte background for biochemical sensing with ion-sensitive field-effect transistors," *ACS Nano*, vol. 6, no. 10, pp. 9291–9298, 2012, pMID: 23016890. [Online]. Available: http://dx.doi.org/10.1021/nn303795r

[75] T. Cohen-Karni, B. P. Timko, L. E. Weiss, and C. M. Lieber, "Flexible electrical recording from cells using nanowire transistor arrays," *Proceedings of the National Academy of Sciences*, vol. 106, no. 18, pp. 7309–7313, 2009.

[76] J. Chang, G. Zhou, E. R. Christensen, R. Heideman, and J. Chen, "Graphene-based sensors for detection of heavy metals in water: a review," *Analytical and bioanalytical chemistry*, vol. 406, no. 16, pp. 3957–3975, 2014.

[77] N. S. Green and M. L. Norton, "Interactions of {DNA} with graphene and sensing applications of graphene field-effect transistor devices: A review," *Analytica Chimica Acta*, vol. 853, no. 0, pp. 127 – 142, 2015. [Online]. Available: http://www.sciencedirect.com/science/article/pii/S0003267014012562

[78] T. K. Truong, T. Nguyen, T. Q. Trung, I. Y. Sohn, D.-J. Kim, J.-H. Jung, and N.-E. Lee, "Reduced graphene oxide field-effect transistor with indium tin oxide extended gate for proton sensing," *Current Applied Physics*, vol. 14, no. 5, pp. 738 – 743, 2014. [Online]. Available: http://www.sciencedirect.com/science/article/pii/S1567173914000893

[79] C. Reiner-Rozman, M. Larisika, C. Nowak, and W. Knoll, "Graphene-based liquid-gated field effect transistor for biosensing: Theory and experiments," *Biosensors and Bioelectronics*, vol. 70, no. 0, pp. 21 – 27, 2015. [Online]. Available: http://www.sciencedirect.com/science/article/pii/S0956566315001578

[80] C. Wang, J. Kim, Y. Zhu, J. Yang, G.-H. Lee, S. Lee, J. Yu, R. Pei, G. Liu, C. Nuckolls, J. Hone, and Q. Lin, "An aptameric graphene nanosensor for label-free detection of small-molecule biomarkers," *Biosensors and Bioelectronics*, vol. 71, no. 0, pp. 222 – 229, 2015. [Online]. Available: http://www.sciencedirect.com/science/article/pii/S0956566315300269

[81] H. G. Sudibya, Q. He, H. Zhang, and P. Chen, "Electrical detection of metal ions using field-effect transistors based on micropatterned reduced graphene oxide films," *ACS Nano*, vol. 5, no. 3, pp. 1990–1994, 2011, pMID: 21338084. [Online]. Available: http://dx.doi.org/10.1021/nn103043v

[82] K. Xu, J. Qian, P. Shukla, M. Dutta, and M. A. Stroscio, "Graphene-based fet structure: modeling fet characteristics for an aptamer-based analyte sensor," in *2012 15th International Workshop on Computational Electronics*. IEEE, 2012, pp. 1–4.

[83] C. Mackin, L. H. Hess, A. Hsu, Y. Song, J. Kong, J. A. Garrido, and T. Palacios, "A current–voltage model for graphene electrolyte-gated field-effect transistors," *IEEE Transactions on Electron Devices*, vol. 61, no. 12, pp. 3971–3977, 2014.

[84] V. Poltev, "Molecular mechanics: Method and applications," in *Handbook of Computational Chemistry*. Springer, 2012, pp. 259–291.

[85] J. Haile, *Molecular dynamics simulation*. Wiley, New York, 1992, vol. 18.

[86] D. Sholl and J. A. Steckel, *Density functional theory: a practical introduction*. John Wiley & Sons, 2011.

[87] "Density functional theory," https://en.wikipedia.org/wiki/Density_functional_theory, 2016, [Online; accessed 21-JUN-2016].

[88] K. Ramachandran, G. Deepa, and K. Namboori, *Computational chemistry and molecular modeling: principles and applications*. Springer Science & Business Media, 2008.

[89] "QM/MM," https://en.wikipedia.org/wiki/QM/MM, 2016, [Online; accessed 21-JUN-2016].

[90] "Semi-empirical quantum chemistry method," https://en.wikipedia.org/wiki/Semi-empirical_quantum_chemistry_method, 2016, [Online; accessed 21-JUN-2016].

[91] K. Farrington, E. Magner, and F. Regan, "Predicting the performance of molecularly imprinted polymers: Selective extraction of caffeine by molecularly imprinted solid phase extraction," *Analytica chimica acta*, vol. 566, no. 1, pp. 60–68, 2006.

[92] A. Molinelli, J. O'Mahony, K. Nolan, M. R. Smyth, M. Jakusch, and B. Mizaikoff, "Analyzing the mechanisms of selectivity in biomimetic self-assemblies via ir and nmr spectroscopy of prepolymerization solutions and molecular dynamics simulations," *Analytical chemistry*, vol. 77, no. 16, pp. 5196–5204, 2005.

[93] J. Saloni, P. Lipkowski, S. S. Dasary, Y. Anjaneyulu, H. Yu, and G. Hill, "Theoretical study of molecular interactions of tnt, acrylic acid, and ethylene glycol dimethacrylate–elements of molecularly imprinted polymer modeling process," *Polymer*, vol. 52, no. 4, pp. 1206–1216, 2011.

[94] A. Kowalska, A. Stobiecka, and S. Wysocki, "A computational investigation of the interactions between harmane and the functional monomers commonly used in molecular imprinting," *Journal of Molecular Structure: THEOCHEM*, vol. 901, no. 1, pp. 88–95, 2009.

[95] A. Fuoco, S. Galier, H. Roux-de Balmann, and G. De Luca, "Correlation between macroscopic sugar transfer and nanoscale interactions in cation exchange membranes," *Journal of Membrane Science*, vol. 493, pp. 311–320, 2015.

[96] T. Zhang, S. Mubeen, N. V. Myung, and M. A. Deshusses, "Recent progress in carbon nanotube-based gas sensors," *Nanotechnology*, vol. 19, no. 33, p. 332001, 2008.

[97] S. Iijima, "Helical microtubules of graphitic carbon," *nature*, vol. 354, no. 6348, pp. 56–58, 1991.

[98] Y. Wang and J. T. Yeow, "A review of carbon nanotubes-based gas sensors," *Journal of sensors*, vol. 2009, 2009.

[99] A. K. Geim and K. S. Novoselov, "The rise of graphene," in *Nanoscience and technology: a collection of reviews from nature journals*. World Scientific, 2010, pp. 11–19.

[100] K. S. Novoselov, V. Fal, L. Colombo, P. Gellert, M. Schwab, K. Kim *et al.*, "A roadmap for graphene," *nature*, vol. 490, no. 7419, pp. 192–200, 2012.

[101] Y. Liu, X. Dong, and P. Chen, "Biological and chemical sensors based on graphene materials," *Chemical Society Reviews*, vol. 41, no. 6, pp. 2283–2307, 2012.

[102] M. Rojas and E. Leiva, "Density functional theory study of a graphene sheet modified with titanium in contact with different adsorbates," *Physical Review B*, vol. 76, no. 15, p. 155415, 2007.

[103] B. Mandal, S. Sarkar, A. Pramanik, and P. Sarkar, "Electronic structure and transport properties of sulfur-passivated graphene nanoribbons," *Journal of Applied Physics*, vol. 112, no. 11, p. 113710, 2012.

[104] V. Barone, O. Hod, and G. E. Scuseria, "Electronic structure and stability of semiconducting graphene nanoribbons," *Nano letters*, vol. 6, no. 12, pp. 2748–2754, 2006.

[105] P. Ruffieux, S. Wang, B. Yang, C. Sánchez-Sánchez, J. Liu, T. Dienel, L. Talirz, P. Shinde, C. A. Pignedoli, D. Passerone *et al.*, "On-surface synthesis of graphene nanoribbons with zigzag edge topology," *Nature*, vol. 531, no. 7595, pp. 489–492, 2016.

[106] X. Deng, Z. Zhang, G. Tang, Z. Fan, and C. Yang, "Spin filtering and large magnetoresistance behaviors in carbon chain-zigzag graphene nanoribbon nanojunctions," *Physics Letters A*, vol. 378, no. 21, pp. 1540–1547, 2014.

[107] H.-p. Zhang, X.-g. Luo, X.-y. Lin, Y.-p. Zhang, P.-p. Tang, X. Lu, and Y. Tang, "Band structure of graphene modulated by ti or n dopants and applications in gas sensoring," *Journal of Molecular Graphics and Modelling*, vol. 61, pp. 224–230, 2015.

[108] S. S. Varghese, S. Swaminathan, K. K. Singh, and V. Mittal, "Ab initio study on gas sensing properties of group iii (b, al and ga) doped graphene," *Computational Condensed Matter*, vol. 9, pp. 40–55, 2016.

[109] B. Huang, "Electronic properties of boron and nitrogen doped graphene nanoribbons and its application for graphene electronics," *Physics Letters A*, vol. 375, no. 4, pp. 845–848, 2011.

[110] A. S. Rad, "Al-doped graphene as a new nanostructure adsorbent for some halomethane compounds: Dft calculations," *Surface Science*, vol. 645, pp. 6–12, 2016.

[111] G. Yu, X. Lü, L. Jiang, W. Gao, and Y. Zheng, "Structural, electronic and magnetic properties of transition-metal embedded zigzag-edged graphene nanoribbons," *Journal of Physics D: Applied Physics*, vol. 46, no. 37, p. 375303, 2013.

[112] H.-p. Zhang, X.-g. Luo, X.-y. Lin, X. Lu, Y. Leng, and H.-t. Song, "Density functional theory calculations on the adsorption of formaldehyde and other harmful gases on pure, ti-doped, or n-doped graphene sheets," *Applied surface science*, vol. 283, pp. 559–565, 2013.

[113] S. A. Tawfik, X. Cui, D. Carter, S. Ringer, and C. Stampfl, "Sensing sulfur-containing gases using titanium and tin decorated zigzag graphene nanoribbons from first-principles," *Physical Chemistry Chemical Physics*, vol. 17, no. 10, pp. 6925–6932, 2015.

[114] H. J. Yoon, J. H. Yang, Z. Zhou, S. S. Yang, M. M.-C. Cheng *et al.*, "Carbon dioxide gas sensor using a graphene sheet," *Sensors and Actuators B: Chemical*, vol. 157, no. 1, pp. 310–313, 2011.

[115] P. Ordejón, E. Artacho, and J. M. Soler, "Self-consistent order-n density-functional calculations for very large systems," *Physical Review B*, vol. 53, no. 16, p. R10441, 1996.

[116] J. M. Soler, E. Artacho, J. D. Gale, A. García, J. Junquera, P. Ordejón, and D. Sánchez-Portal, "The siesta method for ab initio order-n materials simulation," *Journal of Physics: Condensed Matter*, vol. 14, no. 11, p. 2745, 2002.

[117] J. P. Perdew, K. Burke, and M. Ernzerhof, "Generalized gradient approximation made simple," *Physical review letters*, vol. 77, no. 18, p. 3865, 1996.

[118] N. Troullier and J. L. Martins, "Efficient pseudopotentials for plane-wave calculations," *Physical review B*, vol. 43, no. 3, p. 1993, 1991.

[119] C. B. Bast and D. F. Glass-Mattie, "Phosgene," in *Handbook of Toxicology of Chemical Warfare Agents*. Elsevier, 2020, pp. 341–351.

[120] N. R. Council *et al.*, "Acute exposure guideline levels for selected airborne chemicals: Volume 3," 2003.

[121] G. E. P. Box and H. Cullumbine, "The relationship between survival time and dosage with certain toxic agents," *British journal of pharmacology and chemotherapy*, vol. 2, no. 1, p. 27, 1947.

[122] U. P. Kodavanti, D. L. Costa, S. N. Giri, B. Starcher, and G. E. Hatch, "Pulmonary structural and extracellular matrix alterations in fischer 344 rats following subchronic phosgene exposure," *Fundamental and Applied Toxicology*, vol. 37, no. 1, pp. 54–63, 1997.

[123] R. C. Gupta, *Handbook of toxicology of chemical warfare agents*. Academic Press, 2015.

[124] V. Barone, O. Hod, and G. E. Scuseria, "Electronic structure and stability of semiconducting graphene nanoribbons," *Nano letters*, vol. 6, no. 12, pp. 2748–2754, 2006.

[125] ——, "Electronic structure and stability of semiconducting graphene nanoribbons," *Nano letters*, vol. 6, no. 12, pp. 2748–2754, 2006.

[126] A. K. Geim and K. S. Novoselov, "The rise of graphene," in *Nanoscience and technology: a collection of reviews from nature journals*. World Scientific, 2010, pp. 11–19.

[127] Y. Liu, X. Dong, and P. Chen, "Biological and chemical sensors based on graphene materials," *Chemical Society Reviews*, vol. 41, no. 6, pp. 2283–2307, 2012.

[128] N. Shaari and S. Kamarudin, "Graphene in electrocatalyst and proton conductiong membrane in fuel cell applications: An overview," *Renewable and Sustainable Energy Reviews*, vol. 69, pp. 862–870, 2017.

[129] S. S. Varghese, S. Swaminathan, K. K. Singh, and V. Mittal, "Ab initio study on gas sensing properties of group iii (b, al and ga) doped graphene," *Computational Condensed Matter*, vol. 9, pp. 40–55, 2016.

[130] B. Guo, L. Fang, B. Zhang, and J. R. Gong, "Graphene doping: a review," *Insciences J.*, vol. 1, no. 2, pp. 80–89, 2011.

[131] D. Wei, Y. Liu, Y. Wang, H. Zhang, L. Huang, and G. Yu, "Synthesis of n-doped graphene by chemical vapor deposition and its electrical properties," *Nano letters*, vol. 9, no. 5, pp. 1752–1758, 2009.

[132] T. Martins, R. d. Miwa, A. J. Da Silva, and A. Fazzio, "Electronic and transport properties of boron-doped graphene nanoribbons," *Physical review letters*, vol. 98, no. 19, p. 196803, 2007.

[133] M. Rojas and E. Leiva, "Density functional theory study of a graphene sheet modified with titanium in contact with different adsorbates," *Physical Review B*, vol. 76, no. 15, p. 155415, 2007.

[134] N. Darzi, A. Morsali, and S. Beyramabadi, "Mechanism of covalent adsorption of benzenesulfonamide onto cooh–and cocl–functionalised carbon nanotubes," *Progress in Reaction Kinetics and Mechanism*, vol. 41, no. 1, pp. 100–107, 2016.

[135] P. Ordejón, E. Artacho, and J. M. Soler, "Self-consistent order-n density-functional calculations for very large systems," *Physical Review B*, vol. 53, no. 16, p. R10441, 1996.

[136] J. Yun, G. Lee, and K. S. Kim, "Electron transport in graphene nanoribbon field-effect transistor under bias and gate voltages: isochemical potential approach," *The journal of physical chemistry letters*, vol. 7, no. 13, pp. 2478–2482, 2016.

[137] J. M. Soler, E. Artacho, J. D. Gale, A. García, J. Junquera, P. Ordejón, and D. Sánchez-Portal, "The siesta method for ab initio order-n materials simulation," *Journal of Physics: Condensed Matter*, vol. 14, no. 11, p. 2745, 2002.

[138] J. P. Perdew, K. Burke, and M. Ernzerhof, "Generalized gradient approximation made simple," *Physical review letters*, vol. 77, no. 18, p. 3865, 1996.

[139] N. Troullier and J. L. Martins, "Efficient pseudopotentials for plane-wave calculations," *Physical review B*, vol. 43, no. 3, p. 1993, 1991.

[140] A. Zhang, Y. Wu, S.-H. Ke, Y. P. Feng, and C. Zhang, "Bandgap engineering of zigzag graphene nanoribbons by manipulating edge states via defective boundaries," *Nanotechnology*, vol. 22, no. 43, p. 435702, 2011.

[141] H.-p. Zhang, X.-g. Luo, X.-y. Lin, Y.-p. Zhang, P.-p. Tang, X. Lu, and Y. Tang, "Band structure of graphene modulated by ti or n dopants and applications in gas sensoring," *Journal of Molecular Graphics and Modelling*, vol. 61, pp. 224–230, 2015.

[142] T. Cusati, G. Fiori, A. Gahoi, V. Passi, M. C. Lemme, A. Fortunelli, and G. Iannaccone, "Electrical properties of graphene-metal contacts," *Scientific reports*, vol. 7, no. 1, pp. 1–11, 2017.

[143] F. Yavari and N. Koratkar, "Graphene-based chemical sensors," *The journal of physical chemistry letters*, vol. 3, no. 13, pp. 1746–1753, 2012.

[144] F. Schedin, A. K. Geim, S. V. Morozov, E. Hill, P. Blake, M. Katsnelson, and K. S. Novoselov, "Detection of individual gas molecules adsorbed on graphene," *Nature materials*, vol. 6, no. 9, pp. 652–655, 2007.

[145] A. Fairbrother, J.-R. Sanchez-Valencia, B. Lauber, I. Shorubalko, P. Ruffieux, T. Hintermann, and R. Fasel, "High vacuum synthesis and ambient stability of bottom-up graphene nanoribbons," *Nanoscale*, vol. 9, no. 8, pp. 2785–2792, 2017.

[146] S. Iijima, "Helical microtubules of graphitic carbon," *nature*, vol. 354, no. 6348, pp. 56–58, 1991.

[147] T. Zhang, H. Sun, F. Wang, W. Zhang, S. Tang, J. Ma, H. Gong, and J. Zhang, "Adsorption of phosgene molecule on the transition metal-doped graphene: First principles calculations," *Applied Surface Science*, vol. 425, pp. 340–350, 2017.

[148] J. V. Golinski, "Peter shaw: chemistry and communication in augustan england," *Ambix*, vol. 30, no. 1, pp. 19–29, 1983.

[149] S. H. Chooljian and G. B. Kauffman, "Wohler's synthesis of artificial urea: A modern version of a classic experiment," *Journal of Chemical Education*, vol. 56, no. 3, p. 197, 1979.

[150] J. N. Scott, N. V. Nucci, and J. M. Vanderkooi, "Changes in water structure induced by the guanidinium cation and implications for protein denaturation," *The Journal of Physical Chemistry A*, vol. 112, no. 43, pp. 10 939–10 948, 2008.

[151] A. P. Abbott, G. Capper, D. L. Davies, R. K. Rasheed, and V. Tambyrajah, "Novel solvent properties of choline chloride/urea mixtures," *Chemical communications*, no. 1, pp. 70–71, 2003.

[152] T. Tamiri, R. Belitzky Rozin, N. Lemberger, and J. Almog, "Urea nitrate, an exceptionally easy-to-make improvised explosive: Studies towards trace characterization," *Analytical and bioanalytical chemistry*, vol. 395, pp. 421–8, 08 2009.

[153] T. C. Drage, A. Arenillas, K. M. Smith, C. Pevida, S. Piippo, and C. E. Snape, "Preparation of carbon dioxide adsorbents from the chemical activation of urea–formaldehyde and melamine–formaldehyde resins," *Fuel*, vol. 86, no. 1-2, pp. 22–31, 2007.

[154] M. N. COURT, R. C. STEPHEN, and J. S. WAID, "Toxicity as a cause of the inefficiency of urea as a fertilizer." *Journal of Soil Science*, vol. 15, no. 1, pp. 49–65, 1964. [Online]. Available: https://onlinelibrary.wiley.com/doi/abs/10.1111/j.1365-2389.1964.tb00244.x

[155] D. M. Anderson, J. M. Burkholder, W. P. Cochlan, P. M. Glibert, C. J. Gobler, C. A. Heil, R. M. Kudela, M. L. Parsons, J. J. Rensel, D. W. Townsend *et al.*, "Harmful algal blooms and eutrophication: examining linkages from selected coastal regions of the united states," *Harmful algae*, vol. 8, no. 1, pp. 39–53, 2008.

[156] N. E. Christians, A. J. Patton, and Q. D. Law, *Fundamentals of turfgrass management.* John Wiley & Sons, 2016.

[157] A. L. Lehninger, D. L. Nelson, and M. M. Cox, *Overhead Transparency Set for Lehninger Principles of Biochemistry 4th Ed.* WH Freeman, 2004.

[158] D. Braundwald, "Fauci. harrison's principles of internal medicine," 2013.

[159] Y. Shao, J. Wang, H. Wu, J. Liu, I. A. Aksay, and Y. Lin, "Graphene based electrochemical sensors and biosensors: a review," *Electroanalysis: An International Journal Devoted to Fundamental and Practical Aspects of Electroanalysis*, vol. 22, no. 10, pp. 1027–1036, 2010.

[160] A. C. Neto, F. Guinea, N. M. Peres, K. S. Novoselov, and A. K. Geim, "The electronic properties of graphene," *Reviews of modern physics*, vol. 81, no. 1, p. 109, 2009.

[161] Y. Lin and A. Valdes-Garcia, "Sj h eric, y. sun, y. wu, c. dimitrakopo uris, ka jenkins," wafer,"," *Science*, vol. 332, p. 6035, 2011.

[162] B. Zhan, C. Li, J. Yang, G. Jenkins, W. Huang, and X. Dong, "Graphene field-effect transistor and its application for electronic sensing," *Small*, vol. 10, no. 20, pp. 4042–4065, 2014.

[163] K. Pi, K. McCreary, W. Bao, W. Han, Y. Chiang, Y. Li, S.-W. Tsai, C. Lau, and R. Kawakami, "Electronic doping and scattering by transition metals on graphene," *Physical Review B*, vol. 80, no. 7, p. 075406, 2009.

[164] Q. Zhou, C. Wang, Z. Fu, Y. Tang, and H. Zhang, "Adsorption of formaldehyde molecule on stone–wales defected graphene doped with cr, mn, and co: a theoretical study," *Computational materials science*, vol. 83, pp. 398–402, 2014.

[165] H.-p. Zhang, X.-g. Luo, H.-t. Song, X.-y. Lin, X. Lu, and Y. Tang, "Dft study of adsorption and dissociation behavior of h2s on fe-doped graphene," *Applied surface science*, vol. 317, pp. 511–516, 2014.

[166] M. Kaukonen, A. V. Krasheninnikov, E. Kauppinen, and R. M. Nieminen, "Doped graphene as a material for oxygen reduction reaction in hydrogen fuel cells: A computational study," *ACS Catalysis*, vol. 3, no. 2, pp. 159–165, 2013. [Online]. Available: https://doi.org/10.1021/cs300605t

[167] Q. Wang, M.-h. Wang, K.-f. Wang, Y.-c. Zhao, W.-l. Wang, and L.-p. Zhang, "Interactions of anionic and neutral serine with pure and metal-doped graphene studied by density functional theory," *Chinese Journal of Chemical Physics*, vol. 29, no. 4, pp. 437–444, 2016. [Online]. Available: https://doi.org/10.1063/1674-0068/29/cjcp1512250

[168] R. R. Langeslay, D. M. Kaphan, C. L. Marshall, P. C. Stair, A. P. Sattelberger, and M. Delferro, "Catalytic applications of vanadium: a mechanistic perspective," *Chemical reviews*, vol. 119, no. 4, pp. 2128–2191, 2018.

[169] K. Pi, K. McCreary, W. Bao, W. Han, Y. Chiang, Y. Li, S.-W. Tsai, C. Lau, and R. Kawakami, "Electronic doping and scattering by transition metals on graphene," *Physical Review B*, vol. 80, no. 7, p. 075406, 2009.

[170] Z. He, K. He, A. W. Robertson, A. I. Kirkland, D. Kim, J. Ihm, E. Yoon, G.-D. Lee, and J. H. Warner, "Atomic structure and dynamics of metal dopant pairs in graphene," *Nano letters*, vol. 14, no. 7, pp. 3766–3772, 2014.

[171] P. Ordejón, E. Artacho, and J. M. Soler, "Self-consistent order-n density-functional calculations for very large systems," *Physical Review B*, vol. 53, no. 16, p. R10441, 1996.

[172] J. M. Soler, E. Artacho, J. D. Gale, A. García, J. Junquera, P. Ordejón, and D. Sánchez-Portal, "The siesta method for ab initio order-n materials simulation," *Journal of Physics: Condensed Matter*, vol. 14, no. 11, p. 2745, 2002.

[173] J. P. Perdew, K. Burke, and M. Ernzerhof, "Generalized gradient approximation made simple," *Physical review letters*, vol. 77, no. 18, p. 3865, 1996.

[174] N. Troullier and J. L. Martins, "Efficient pseudopotentials for plane-wave calculations," *Physical review B*, vol. 43, no. 3, p. 1993, 1991.

[175] A. Krasheninnikov, P. Lehtinen, A. S. Foster, P. Pyykkö, and R. M. Nieminen, "Embedding transition-metal atoms in graphene: structure, bonding, and magnetism," *Physical review letters*, vol. 102, no. 12, p. 126807, 2009.

[176] N. A. Ardehjani and D. Farmanzadeh, "Dft investigation of metal doped graphene capacity for adsorbing of ozone, nitrogen dioxide and sulfur dioxide molecules," *Adsorption*, vol. 25, no. 4, pp. 661–667, 2019.

[177] Q. Zhou, L. Yuan, X. Yang, Z. Fu, Y. Tang, C. Wang, and H. Zhang, "Dft study of formaldehyde adsorption on vacancy defected graphene doped with b, n, and s," *Chemical Physics*, vol. 440, pp. 80–86, 2014.

[178] T. Zhang, H. Sun, F. Wang, W. Zhang, S. Tang, J. Ma, H. Gong, and J. Zhang, "Adsorption of phosgene molecule on the transition metal-doped graphene: First principles calculations," *Applied Surface Science*, vol. 425, pp. 340–350, 2017.

[179] A. N. Chermahini, A. Teimouri, and H. Farrokhpour, "Theoretical studies of urea adsorption on single wall boron-nitride nanotubes," *Applied surface science*, vol. 320, pp. 231–236, 2014.

[180] Y. Gao, N. Zhao, W. Wei, and Y. Sun, "Ab initio dft study of urea adsorption and decomposition on the zno (101¯ 0) surface," *Computational and Theoretical Chemistry*, vol. 992, pp. 1–8, 2012.

[181] A. Singh and B. Ganguly, "Dft study of urea interaction with potassium chloride surfaces," *Molecular Simulation*, vol. 34, no. 10-15, pp. 973–979, 2008. [Online]. Available: https://doi.org/10.1080/08927020802129966

[182] R. J. Meiers and B. Coussens, "The molecular structure of the urea molecule: is the minimum energy structure planar?" *Journal of Molecular Structure: THEOCHEM*, vol. 253, pp. 25–33, 1992.

[183] H. Luo, H. Li, Z. Xia, Y. Chu, J. Zheng, Z. Hou, and Q. Fu, "Novel insights into l-cysteine adsorption on transition metal doped graphene: influences of the dopant and the vacancy," *RSC advances*, vol. 6, no. 35, pp. 29 830–29 839, 2016.

[184] L. N. Plummer and E. Busenberg, "Chlorofluorocarbons," in *Environmental tracers in subsurface hydrology*. Springer, 2000, pp. 441–478.

[185] C. Brock and E. C. Coyner, "freon dielectric-coolants," in *1965 Sixth Electrical Insulation Conference*. IEEE, 1965, pp. 247–250.

[186] G. B. Kauffman, "Frederic swarts: Pioneer in organic fluorine chemistry," *Journal of Chemical Education*, vol. 32, no. 6, p. 301, 1955.

[187] A. B. Garrett, "Freon: Thomas midgley and albert l. henne," *Journal of Chemical Education*, vol. 39, no. 7, p. 361, 1962.

[188] V. Ramanathan, "Greenhouse effect due to chlorofluorocarbons: Climatic implications," *Science*, pp. 50–52, 1975.

[189] B.-S. Lee and C.-B. Chiou, "The relationship of meteorological and anthropogenic factors to time series measurements of cfc-11, cfc-12, and ch3ccl3 concentrations in the urban atmosphere," *Atmospheric Environment*, vol. 42, no. 33, pp. 7706–7717, 2008.

[190] G. J. Velders, S. O. Andersen, J. S. Daniel, D. W. Fahey, and M. McFarland, "The importance of the montreal protocol in protecting climate," *Proceedings of the National Academy of Sciences*, vol. 104, no. 12, pp. 4814–4819, 2007.

[191] N. Campbell, R. Shende, M. Bennett, O. Blinova, R. Derwent, A. McCulloch, M. Yamabe, J. Shevlin, and T. Vink, "Hfcs and pfcs: Current and future supply, demand and emissions, plus emissions of cfcs, hcfcs and halons," *Safeguarding the Ozone Layer and the Global Climate System, Issues Related to Hydrofluorocarbons and Perfluorocarbons, IPCC/TEAP Special Report*, pp. 404–436, 2005.

[192] A. Antušek, K. Jackowski, M. Jaszuński, W. Makulski, and M. Wilczek, "Nuclear magnetic dipole moments from nmr spectra," *Chemical physics letters*, vol. 411, no. 1-3, pp. 111–116, 2005.

[193] T. E. Field-Theodore, M. Olejniczak, M. Jaszuński, and D. J. Wilson, "Nmr shielding constants in group 15 trifluorides," *Physical Chemistry Chemical Physics*, vol. 20, no. 35, pp. 23 025–23 033, 2018.

[194] A. Groppi, A. Polettini, P. Lunetta, G. Achille, and M. Montagna, "A fatal case of trichlorofluoromethane (freon 11) poisoning. tissue distribution study by gas chromatography-mass spectrometry," *Journal of Forensic Science*, vol. 39, no. 3, pp. 871–876, 1994.

[195] R. Oenbrink, "Unexpected adverse effects of freon 11 and freon 12 as medication propellants," *J Am Osteopath Assoc*, vol. 93, pp. 714–8, 1993.

[196] N. R. Council *et al.*, *Spacecraft Maximum Allowable Concentrations for Selected Airborne Contaminants: Volume 4*. National Academies Press, 2000, vol. 4.

[197] I. A. E. Agency, *Use of chlorofluorocarbons in hydrology: a guidebook*. Internat. Atomic Energy Agency, 2006.

[198] K. S. e. a. Novoselov, "Two-dimensional gas of massless dirac fermions in graphene," *nature*, vol. 438, no. 7065, pp. 197–200, 2005.

[199] A. C. Neto, F. Guinea, N. M. Peres, K. S. Novoselov, and A. K. Geim, "The electronic properties of graphene," *Reviews of modern physics*, vol. 81, no. 1, p. 109, 2009.

[200] Y.-M. Lin, A. Valdes-Garcia, S.-J. Han, D. B. Farmer, I. Meric, Y. Sun, Y. Wu, C. Dimitrakopoulos, A. Grill, P. Avouris *et al.*, "Wafer-scale graphene integrated circuit," *Science*, vol. 332, no. 6035, pp. 1294–1297, 2011.

[201] B. Zhan, C. Li, J. Yang, G. Jenkins, W. Huang, and X. Dong, "Graphene field-effect transistor and its application for electronic sensing," *Small*, vol. 10, no. 20, pp. 4042–4065, 2014.

[202] S. Rumyantsev, G. Liu, M. S. Shur, R. A. Potyrailo, and A. A. Balandin, "Selective gas sensing with a single pristine graphene transistor," *Nano letters*, vol. 12, no. 5, pp. 2294–2298, 2012.

[203] K. Pi, K. McCreary, W. Bao, W. Han, Y. Chiang, Y. Li, S.-W. Tsai, C. Lau, and R. Kawakami, "Electronic doping and scattering by transition metals on graphene," *Physical Review B*, vol. 80, no. 7, p. 075406, 2009.

[204] M. Kaukonen, A. Krasheninnikov, E. Kauppinen, and R. Nieminen, "Doped graphene as a material for oxygen reduction reaction in hydrogen fuel cells: a computational study," *ACS catalysis*, vol. 3, no. 2, pp. 159–165, 2013.

[205] Q. Zhou, C. Wang, Z. Fu, Y. Tang, and H. Zhang, "Adsorption of formaldehyde molecule on stone–wales defected graphene doped with cr, mn, and co: a theoretical study," *Computational materials science*, vol. 83, pp. 398–402, 2014.

[206] X.-Y. Liu and J.-M. Zhang, "Formaldehyde molecule adsorbed on doped graphene: a first-principles study," *Applied surface science*, vol. 293, pp. 216–219, 2014.

[207] M. Kaukonen, A. Krasheninnikov, E. Kauppinen, and R. Nieminen, "Doped graphene as a material for oxygen reduction reaction in hydrogen fuel cells: a computational study," *ACS catalysis*, vol. 3, no. 2, pp. 159–165, 2013.

[208] P. Ordejón, E. Artacho, and J. M. Soler, "Self-consistent order-n density-functional calculations for very large systems," *Physical Review B*, vol. 53, no. 16, p. R10441, 1996.

[209] J. M. Soler, E. Artacho, J. D. Gale, A. García, J. Junquera, P. Ordejón, and D. Sánchez-Portal, "The siesta method for ab initio order-n materials simulation," *Journal of Physics: Condensed Matter*, vol. 14, no. 11, p. 2745, 2002.

[210] J. P. Perdew, K. Burke, and M. Ernzerhof, "Generalized gradient approximation made simple," *Physical review letters*, vol. 77, no. 18, p. 3865, 1996.

[211] N. Troullier and J. L. Martins, "Efficient pseudopotentials for plane-wave calculations," *Physical review B*, vol. 43, no. 3, p. 1993, 1991.

[212] T. Zhang, H. Sun, F. Wang, W. Zhang, S. Tang, J. Ma, H. Gong, and J. Zhang, "Adsorption of phosgene molecule on the transition metal-doped graphene: First principles calculations," *Applied Surface Science*, vol. 425, pp. 340–350, 2017.

[213] Q. Zhou, L. Yuan, X. Yang, Z. Fu, Y. Tang, C. Wang, and H. Zhang, "Dft study of formaldehyde adsorption on vacancy defected graphene doped with b, n, and s," *Chemical Physics*, vol. 440, pp. 80–86, 2014.

[214] R. D. J. III, "Computational chemistry comparison and benchmark database," NIST, Aug 21, 2020. [Online]. [Online]. Available: https://cccbdb.nist.gov/

[215] S. Kumaran, M.-C. Su, K. Lim, J. Michael, A. Wagner, L. B. Harding, and D. A. Dixon, "Ab initio calculations and three different applications of unimolecular rate theory for the dissociations of ccl4, cfcl3, cf2cl2, and cf3cl," *The Journal of Physical Chemistry*, vol. 100, no. 18, pp. 7541–7549, 1996.

[216] A. Pompella, A. Visvikis, A. Paolicchi, V. De Tata, and A. F. Casini, "The changing faces of glutathione, a cellular protagonist," *Biochemical pharmacology*, vol. 66, no. 8, pp. 1499–1503, 2003.

[217] K. M. Halprin and A. Ohkawara, "The measurement of glutathione in human epidermis using glutathione reductase," *J invest dermatol*, vol. 48, no. 2, pp. 149–52, 1967.

[218] S.-B. Ha, A. P. Smith, R. Howden, W. M. Dietrich, S. Bugg, M. J. O'Connell, P. B. Goldsbrough, and C. S. Cobbett, "Phytochelatin synthase genes from arabidopsis and the yeast schizosaccharomyces pombe," *The Plant Cell*, vol. 11, no. 6, pp. 1153–1163, 1999.

[219] P. Ruzza, A. Rosato, C. R. Rossi, M. Floreani, and L. Quintieri, "Glutathione transferases as targets for cancer therapy," *Anti-Cancer Agents in Medicinal Chemistry (Formerly Current Medicinal Chemistry-Anti-Cancer Agents)*, vol. 9, no. 7, pp. 763–777, 2009.

[220] M. Raggi, L. Nobile, and A. Giovannini, "Spectrophotometric determination of glutathione and of its oxidation product in pharmaceutical dosage forms," *Journal of pharmaceutical and biomedical analysis*, vol. 9, no. 10-12, pp. 1037–1040, 1991.

[221] M. Kominkova, P. Horky, N. Cernei, K. Tmejova, B. Ruttkay-Nedecky, R. Guran, M. Pohanka, O. Zitka, V. Adam, and R. Kizek, "Optimization of the glutathione detection by high performance liquid chromatography with electrochemical detection in the brain and liver of rats fed with taurine," *Int. J. Electrochem. Sci*, vol. 10, no. 2, pp. 1716–1727, 2015.

[222] D. L. Rabenstein, D. W. Brown, and C. J. McNeil, "Determination of glutathione in intact and hemolyzed erythrocytes by titration with tert-butyl hydroperoxide with end point detection by proton nuclear magnetic resonance spectrometry," *Analytical chemistry*, vol. 57, no. 12, pp. 2294–2299, 1985.

[223] C. Yang, Y. Huang, B. L. Hassler, R. M. Worden, and A. J. Mason, "Amperometric electrochemical microsystem for a miniaturized protein biosensor array," *IEEE transactions on biomedical circuits and systems*, vol. 3, no. 3, pp. 160–168, 2009.

[224] J. Guerrero-Contreras and F. Caballero-Briones, "Graphene oxide powders with different oxidation degree, prepared by synthesis variations of the hummers method," *Materials Chemistry and Physics*, vol. 153, pp. 209–220, 2015.

[225] H. Huang, Y. Wang, Y. Zhang, Z. Niu, and X. Li, "Amino-functionalized graphene oxide for cr (vi), cu (ii), pb (ii) and cd (ii) removal from industrial wastewater," *Open Chemistry*, vol. 18, no. 1, pp. 97–107, 2020.

[226] R. K. Sharma, A. Sharma, S. Sharma, S. Dutta, S. Yadav, and B. Arora, "Design and exploration of catalytic activity of two-dimensional surface-engineered graphene oxide nanosheets in the transannulation of n-heterocyclic aldehydes or ketones with alkylamines," *ACS omega*, vol. 4, no. 2, pp. 3146–3158, 2019.

[227] X. Pu, H.-B. Zhang, X. Li, C. Gui, and Z.-Z. Yu, "Thermally conductive and electrically insulating epoxy nanocomposites with silica-coated graphene," *Rsc Advances*, vol. 4, no. 29, pp. 15 297–15 303, 2014.

[228] S. Dadkhah, E. Ziaei, A. Mehdinia, T. B. Kayyal, and A. Jabbari, "A glassy carbon electrode modified with amino-functionalized graphene oxide and molecularly imprinted polymer for electrochemical sensing of bisphenol a," *Microchimica Acta*, vol. 183, no. 6, pp. 1933–1941, 2016.

[229] M. Z. Iqbal, M. S. Katsiotis, S. M. Alhassan, M. W. Liberatore, and A. A. Abdala, "Effect of solvent on the uncatalyzed synthesis of aminosilane-functionalized graphene," *RSC advances*, vol. 4, no. 13, pp. 6830–6839, 2014.

[230] X. Zhi, Y. Mao, Z. Yu, S. Wen, Y. Li, L. Zhang, T. W. Chan, and L. Liu, "gamma aminopropyl triethoxysilane functionalized graphene oxide for composites with high dielectric constant and low dielectric loss," *Composites Part A: Applied Science and Manufacturing*, vol. 76, pp. 194–202, 2015.

[231] M. Z. Iqbal, M. S. Katsiotis, S. M. Alhassan, M. W. Liberatore, and A. A. Abdala, "Effect of solvent on the uncatalyzed synthesis of aminosilane-functionalized graphene," *RSC advances*, vol. 4, no. 13, pp. 6830–6839, 2014.

[232] M. Taei, H. Hadadzadeh, F. Hasanpour, G. Zahedi, and Z. Dehbanipour, "A voltammetric sensor based on multiwalled carbon nanotubes and a new azoferrocene derivative for determination of glutathione," *IEEE Sensors Journal*, vol. 15, no. 8, pp. 4472–4479, 2015.

[233] P. T. Lee, L. M. Goncalves, and R. G. Compton, "Electrochemical determination of free and total glutathione in human saliva samples," *Sensors and Actuators B: Chemical*, vol. 221, pp. 962–968, 2015.

[234] Y. Wang, L. Jiang, L. Chu, W. Liu, S. Wu, Y. Wu, X. He, and K. Wang, "Electrochemical detection of glutathione by using thymine-rich dna-gated switch functionalized mesoporous silica nanoparticles," *Biosensors and Bioelectronics*, vol. 87, pp. 459–465, 2017.

[235] Y. Lv, L. Yang, X. Mao, M. Lu, J. Zhao, and Y. Yin, "Electrochemical detection of glutathione based on hg2+-mediated strand displacement reaction strategy," *Biosensors and Bioelectronics*, vol. 85, pp. 664–668, 2016.

[236] Y. Oztekin, A. Ramanaviciene, and A. Ramanavicius, "Electrochemical glutathione sensor based on electrochemically deposited poly-m-aminophenol," *Electroanalysis*, vol. 23, no. 3, pp. 701–709, 2011.

[237] pubchem, "pubchem," pubchem, July, 2021. [Online]. [Online]. Available: https://pubchem.ncbi.nlm.nih.gov/compound/Lactate

[238] D.-E. Chang, H.-C. Jung, J.-S. Rhee, and J.-G. Pan, "Homofermentative production of d-orl-lactate in metabolically engineered escherichia coli rr1," *Applied and environmental microbiology*, vol. 65, no. 4, pp. 1384–1389, 1999.

[239] A. Parra, E. Casero, L. Vázquez, F. Pariente, and E. Lorenzo, "Design and characterization of a lactate biosensor based on immobilized lactate oxidase onto gold surfaces," *Analytica Chimica Acta*, vol. 555, no. 2, pp. 308–315, 2006.

[240] K. Rathee, V. Dhull, R. Dhull, and S. Singh, "Biosensors based on electrochemical lactate detection: A comprehensive review," *Biochemistry and biophysics reports*, vol. 5, pp. 35–54, 2016.

[241] I. Jacobs, "Blood lactate," *Sports medicine*, vol. 3, no. 1, pp. 10–25, 1986.

[242] L. W. Andersen, J. Mackenhauer, J. C. Roberts, K. M. Berg, M. N. Cocchi, and M. W. Donnino, "Etiology and therapeutic approach to elevated lactate levels," in *Mayo Clinic Proceedings*, vol. 88, no. 10. Elsevier, 2013, pp. 1127–1140.

[243] nursingcenter, "nursingcenter," nursingcenter, July, 2021. [Online]. [Online]. Available: https://www.nursingcenter.com/ncblog/march-2017/elevated-lactate-%E2%80%93-not-just-a-marker-for-sepsis-an

[244] T. P. Velavan, A. K. Le Thi Kieu Linh, J. Gabor, S. Krishna, and P. G. Kremsner, "Longitudinal monitoring of lactate in hospitalized and ambulatory covid-19 patients," *The American Journal of Tropical Medicine and Hygiene*, vol. 104, no. 3, p. 1041, 2021.

[245] N. Aydemir, J. Malmström, and J. Travas-Sejdic, "Conducting polymer based electrochemical biosensors," *Physical Chemistry Chemical Physics*, vol. 18, no. 12, pp. 8264–8277, 2016.

[246] C. Dhand, M. Das, M. Datta, and B. Malhotra, "Recent advances in polyaniline based biosensors," *Biosensors and Bioelectronics*, vol. 26, no. 6, pp. 2811–2821, 2011.

[247] C. Dhand, N. Dwivedi, S. Mishra, P. R. Solanki, V. Mayandi, R. W. Beuerman, S. Ramakrishna, R. Lakshminarayanan, and B. D. Malhotra, "Polyaniline-based biosensors," *Nanobiosensors in disease diagnosis*, vol. 4, p. 25, 2015.

[248] A. Chaubey, K. Pande, V. Singh, and B. Malhotra, "Co-immobilization of lactate oxidase and lactate dehydrogenase on conducting polyaniline films," *Analytica chimica acta*, vol. 407, no. 1-2, pp. 97–103, 2000.

[249] J. Zhu, X. Huo, X. Liu, and H. Ju, "Gold nanoparticles deposited polyaniline–tio2 nanotube for surface plasmon resonance enhanced photoelectrochemical biosensing," *ACS applied materials & interfaces*, vol. 8, no. 1, pp. 341–349, 2016.

[250] A. Chaubey, K. K. Pande, M. K. Pandey, and V. S. Singh, "Signal amplification by substrate recycling on polyaniline/lactate oxidase/lactate dehydrogenase bienzyme electrodes," *Applied biochemistry and biotechnology*, vol. 96, no. 1, pp. 239–248, 2001.

[251] M. Rahman, M. J. Shiddiky, M. A. Rahman, and Y.-B. Shim, "A lactate biosensor based on lactate dehydrogenase/nictotinamide adenine dinucleotide (oxidized form) immobilized on a conducting polymer/multiwall carbon nanotube composite film," *Analytical biochemistry*, vol. 384, no. 1, pp. 159–165, 2009.

[252] H. Cheng, C. Hu, Z. Ji, W. Ma, and H. Wang, "A solid ionic lactate biosensor using doped graphene-like membrane of au-evimc-titania nanotubes-polyaniline," *Biosensors and Bioelectronics*, vol. 118, pp. 97–101, 2018.

[253] E. Simon, C. M. Halliwell, C. S. Toh, A. E. Cass, and P. N. Bartlett, "Immobilisation of enzymes on poly (aniline)–poly (anion) composite films. preparation of bioanodes for biofuel cell applications," *Bioelectrochemistry*, vol. 55, no. 1-2, pp. 13–15, 2002.

[254] D. Bandgar, G. Khuspe, R. Pawar, C. Lee, and V. Patil, "Facile and novel route for preparation of nanostructured polyaniline (pani) thin films," *Applied Nanoscience*, vol. 4, no. 1, pp. 27–36, 2014.

[255] Q. Qin and Y. Guo, "Preparation and characterization of nano-polyaniline film on ito conductive glass by electrochemical polymerization," *Journal of Nanomaterials*, vol. 2012, 2012.

[256] F. Xu, G. Zheng, D. Wu, Y. Liang, Z. Li, and R. Fu, "Improving electrochemical performance of polyaniline by introducing carbon aerogel as filler," *Physical Chemistry Chemical Physics*, vol. 12, no. 13, pp. 3270–3275, 2010.

[257] W. Yue, H. Dawei, and W. Yongsheng, "Enhanced microwave absorption performance of mof-derived hollow zn-co/c anchored on reduced graphene oxide," *Chinese Physics B*, vol. 30, no. 6, pp. 67 804–067 804, 2021.

[258] J. Manuel, T. Salguero, and R. P. Ramasamy, "Synthesis and characterization of polyaniline nanofibers as cathode active material for sodium-ion battery," *Journal of Applied Electrochemistry*, vol. 49, no. 5, pp. 529–537, 2019.

List of Publications

Journal Publications

- R. Singh, R. Paily, "Adsorption of Urea over Transition Metal-Doped Graphene: A DFT Study". Journal of Electronic Materials. 2019 Nov 1;48(11):6940-8.
- R. Singh, R. Paily, "First Principle Study of Adsorption of Chlorofluorocarbons over Ti-doped Two-dimensional Graphene Sheet". (Under review in IEEE Transactions on Nanotechnology)
- R. Vatsyayan, R. Singh, V. Settipalli, R. Paily, "Adsorption of Phosgene on Titanium Doped Graphene Nanoribbons: A DFT Study". IEEE Transactions on Nanotechnology. 2019 Oct 28;18:1174-80.
- R. Vatsyayan, Rajan Singh, Roy Paily, "Adsorption of Air Pollutants Gases over Ti-doped ZGNR Structures: A DFT study", International Journal of Nanoparticles (1753-2507).

Conference Publications

- Ritwik Vatsyayan, Rajan Singh, and Roy Paily, "Adsorption of CO and NO on Ti-doped ZGNR structures: A DFT study",2nd international conference 2017 Devices for Integrated Circuit (DevIC), Kalyani Government Engineering College, March 23-24, 2017. Engineering College, March 23-24, 2017.
- Samyak Dhole, Rajan Singh, and Roy Paily, "The Effects of Backbone Fluorination on Photovoltaic Properties of Polymers of Thiophene, Selenophene and Tellurophene and their Hexyl Derivatives: A DFT study", 2nd international conference 2017 Devices for Integrated Circuit (DevIC),Kalyani Government Engineering College, March 23-24, 2017.

Manuscripts Under Preparation

- Rajan Singh, and Roy Paily, "First principle based Theoretical Investigation of Adsorption of Toxic Gaseous Molecules over Doped Graphene Nanostructures." [To be submitted in Transactions on Nanotechnology]
- Rajan Singh, and Roy Paily, "Functionlized Graphene-FET biosensor for label-free Glutathione Sensing." [To be submitted in Transactions on Electron Devices]

- Rajan Singh, and Roy Paily, "Functionlized Polyaniline Electrodes for Lactate/LDH Sensing." [To be submitted in Transactions on Electron Devices]

Patents Under Preparation

- Rajan Singh, and Roy Paily, "Functionlized Graphene-FET biosensor for label-free Glutathione Sensing." [To be submitted as an Indian Patent]
- Rajan Singh, and Roy Paily, "Functionlized Polyaniline Electrodes for Lactate/LDH Sensing." [To be submitted as an Indian Patent]

Additional List of Publications

Patent Submitted

- Supriya Das, Rajan Singh, Avijit Das, Sudipta Bag, Roy P. Paily and Uttam Manna, "Low-Strain based, Water Repellent and Highly Sensitive Human Motion Sensor", submitted as an US Patent.

Journal Publications

- Supriya Das, Rajan Singh, Avijit Das, Sudipta Bag, Roy P. Paily, and Uttam Manna. "Abrasion Tolerant, Non-Stretchable and Super-Water-Repellent Conductive & Ultrasensitive Pattern for Identifying Slow, Fast, Weak and Strong Human Motions at Diverse Conditions." Materials Horizons (2021). [First three authors contributed equally to this work.]
- Monica Naorem, Rajan Singh, and Roy Paily. "Detection of Hydrogen Peroxide using rGO/PPy Nanocomposites in Silicon Dioxide Trench Embedded Field Effect Transistor." IEEE Sensors Journal (2021).
- Monica Naorem, Rajan Singh, and Roy Paily. "Ionic Liquid Channel Field Effect Transistor Fabricated Using Silicon Dioxide Trench." IEEE Transactions on Electron Devices 68, no. 9 (2021): 4741-4747.
- Soham Talukder, Rajan Singh, Satyajit Bora, and Roy Paily. "An efficient architecture for QRS detection in FPGA using integer Haar wavelet transform." Circuits, Systems, and Signal Processing (2020): 1-16.